University of Strathclyde

Department of Naval Architecture, Ocean and Marine Engineering

Experimental and Numerical Analysis of the Squat and Resistance of Ships Advancing through the New Suez Canal

Khaled Elsherbiny

A thesis presented in fulfilment of the requirements for the degree of Doctor of Philosophy

2020

This thesis is the result of the author's original research. It has been composed by the author and has not been previously submitted for examination which has led to the award of a degree.

Signed: **Date:**

Acknowledgements

Without a doubt, I have spent four years very productive and enjoyable years during my studies in Glasgow. I would like to thank everyone who contributed to this, and helped me towards completing my PhD with their advice, assistance and friendship.

To start with, I would like to express the deepest appreciation to my primary supervisor, Dr. Tahsin Tezdogan, who has been a tremendous mentor for me during the last four years. I have benefited from his boundless experience and guidance in both my academic and private life. Dr. Tahsin has always been a perfect example to me, with his everlasting energy and outstanding academic career. If he had not believed in me, I would have not achieved this. I aspire to become a lecturer like him in the near future. In addition, I would like to acknowledge the valuable support and help of my second supervisor, Professor Atilla Incecik.

Also, I would like to thank the Professor Mohamed Kotb my third supervisor for his continuous help and support to me. I am indebted him for his understanding and precious advice. Moreover, I gratefully acknowledge the sponsorship of Arab Academy for Science Technology and Maritime Transport in Egypt, fully supported my PhD research at the University of Strathclyde, Glasgow. Thanks are also extended to my professor, colleagues, friends at the Department of Marine Engineering.

I would also like to thank the University of Strathclyde Faculty of Engineering for provision of the Kelvin Hydrodynamics Lab where the experimental results were obtained using Lab facilities.

I would also like to thank the University of Strathclyde Faculty of Engineering for provision of the ARCHIE-WeSt high performance computing facilities. The CFD results were obtained using the EPSRC funded ARCHIE-WeSt High Performance Computer (www.archie-west.ac.uk).

I would also like to thank the Suez Canal Authority to allowed me have a tour for New Suez Canal and providing me with necessary information and documentation for characteristics of New Suez Canal. In particular, I would like to extend my sincere appreciation to Mr. Essam Metawlly for his assistance and help in the regards.

Additionally, I would like to thank my colleague and friend Momchil Terziev who assisted me during my PhD and helped me out.

Last, but definitely not least, I would like to thank the very understanding and supportive Raghda Mohamed my beloved wife. I gratefully acknowledge her continuous help. Without her support and motivation, I would not have completed this thesis work on time.

And finally, I would like to thank my Father, mother, brother and my sisters for always supporting my decisions and for believing in me.

CONTENTS

List of Figures

List of Tables

ABSTRACT

When a ship is sailing in shallow and restricted waters such as harbours and canals, it is usually accompanied by obvious sinkage and trim, called squat. The ship squat has important influences on ship hydrodynamic performance in shallow and restricted water such as ship resistance. Squat is caused by the drop in pressure under the bottom of the ship, where the relative speed of the water is higher. Due to the squat effect, the hydrodynamic forces on the ship will increase largely, ship control will become difficult and risks of grounding may increase.

A new division of the Suez Canal is called New Suez Canal, recently opened for international navigation. It is important to obtain accurate prediction data for ship squat to minimise the risk of grounding in this canal. Accurate prediction of the squat is of great significance to correctly evaluate ship hydrodynamic performance and to ensure navigation safety in the New Suez Canal. In this study, various methods for prediction of ship squat were conducted and introduced.

A series of experiments were conducted with a model scale of the KRISO Container Ship (KCS) at 1:75 scale. The squat of the KCS was examined by measuring its sinkage, trim and resistance. The influences of ship speed, water depth, ship-bank distance on the squat and blockage effect were analysed. The results indicated that for Froude's number based on depth (Fn_h) below 0.4, measured squat values do not change with either Fn_h or depth to draft ratio (H/T). The squat increases with H/T values for the depth Froude numbers higher than 0.4. Moreover, a ship's speed can be increased to up to 9 knots inside the New Suez Canal with no adverse effects, thus significantly reducing the time for a ship to pass through the Canal. Next, the study of reduced the Canal width to 62.5% of its real-life cross sectional area, no significant effect was observed on ship squat.

Moreover, a series of experimental tests were conducted at loading conditions under different trimming angles to examine the range of ship trim for safe and efficient sailing in canals. to detect the best trim angle for ships during sailing in restricted waters to reduce resistance and therefore fuel consumption. The results show that for depth Froude's numbers higher than 0.4, the ship model sinkage is less for aft trim than for level trim or

forward trim. Concurrently, it can be observed that there is less water resistance for aft trim than for forward trim, albeit level trim shows the least resistance.

Furthermore, the present study combines numerical, analytical and empirical methods for a holistic approach in calm water. As a case-study, the KCS hullform is adopted, and analysed experimentally, via Computational Fluid Dynamics, using the slender body theory, and empirical formulae. The results reveal strong effect between the canal's cross section and all examined parameters. In addition, CFD calculations proved to be a reliable tool for predicting ship performance while navigating shallow and restricted waters. CFD simulations in multiphase and double body regime are performed to reveal the form factor and wave resistance of the KCS. This is performed in two different canals while varying the depth Froude number. The results suggest a dependency of the form factor on ship speed. Analytical and empirical methods were used for comparison, the slender body theory, provided good predictions in the low speed range, but did not agree well with the experimental data at high speeds. To model the sloping canal sides of the Suez Canal via the slender body theory, a rectangular canal with equivalent blockage was constructed, which may have influenced the accuracy of the theory.

Chapter One

1. INTRODUCTION

To begin with, this chapter will provide an insight and introduction about recent expansion project; the New Suez Canal. Following this, it will define the squat incident for ships and the effect of shallow and restricted water on this phenomenon. Next, it will present research aims and objectives, and finally, the chapter will provide an overview of the structure and layout of this thesis.

1.1 New Suez Canal

The well-known Suez Canal is located in Egypt, in the West of the Sinai Peninsula. It connects Port Said on the Mediterranean Sea with the Port of Suez on the Red Sea, and provides an essentially direct route for the transport of goods between Europe and Asia. The Canal separates the African continent from Asia, and it offers the shortest maritime route between Europe and the lands lying around the Indian and western Pacific oceans. It is one of the world's most heavily used shipping lanes.

The Suez Canal is also one of the most important waterways in the world. It is a sea level canal and the water depth slightly differs throughout the canal and the extreme tidal range is 65 cm in the north and 1.9 m in the south. The banks of the canal are protected against the wash and waves, generated by the transit of ships, by revetments of hard stones and steel sheet piles corresponding to the nature of soil in every area. On both sides of the canal, there are mooring bollards every 125 m for the mooring of vessels in case of emergency, and kilometric sign posts helping locate the position of ships in the waterway. The navigable channel is bordered by light and reflecting buoys as navigational aids to night traffic (Suez Canal Authority, 2019a).

Figure 1 shows the Suez Canal’s location. It should be noted that the Canal supports approximately 8% of the world’s shipping traffic with almost fifty vessels traveling through the canal each day (Suez Canal Authority, 2019a).

Figure 1 Suez Canal location (Suez Canal Authority, 2019a)

A new shipping lane (termed the New Suez Canal) was added to the existing Suez Canal and was inaugurated on 5 August 2015, as can be seen in Figure 2. In addition, other parts of the Suez Canal were made deeper and wider (Suez Canal Authority, 2019a). Figure 3 shows the canal's cross section and Table 1 presents Suez Canal's main dimensions in addition to the maximum ship speed and draft permitted.

Figure 2 Aerial view for the New Suez Canal (Suez Canal Authority, 2019a)

The aim of opening a new lane is to create a new canal, parallel to the existing one, is to maximise benefits from the present canal and its by-passes, and double the longest possible parts of the waterway to facilitate the traffic in the two directions and to minimise

the waiting time for transiting ships. This will certainly reduce the time needed for the trip from one end of the canal to the other, and will increase the cargo capacity of the waterway, in anticipation of the expected growth in world trade.

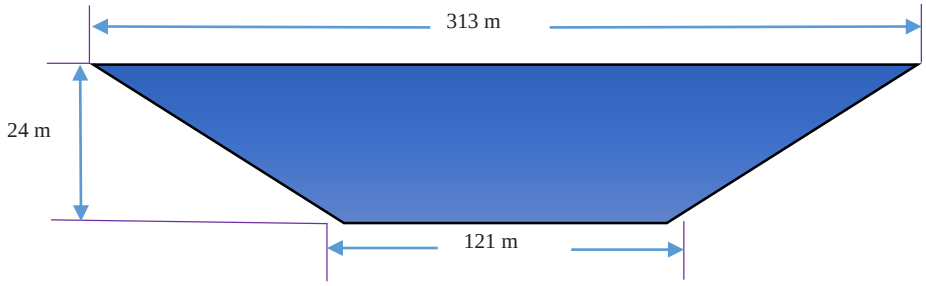

Figure 3 New Suez Canal cross sectional area

Table 1 Suez Canal Characteristics (Suez Canal Authority, 2019a) (DWT: Deadweight tonnage)

Parameter	Unit	Value
Overall length	km	193.30
Double path length	km	113.3
The width range along the canal at 11 m depth	m	205-225
Water depth	m	24
Maximum draft of ship	m	20.12
The cross sectional area range along the Canal	m^2	4800-5200
Max. loaded ship	DWT	240000
Maximum vessel passing speed	knot	7
Maximum vessel beam	m	77.5
Distance between two ships	km	2

The New Suez Canal is expected to expand trade along the fastest shipping route between Europe and Asia. The new added canal allows ships to sail in both directions at the same time. This decreases the transit time from 18 hours to 11 hours for the southbound convoy. It also shortens the waiting time for vessels down to a maximum of three hours, rather than the previous 8-11 hours. This will cut down on trip costs and make the Suez Canal more attractive for ship owners. The New Suez Canal is expected to virtually double the

capacity of the Suez Canal from 49 to 97 ships a day. Moreover, direct unstopped transit for 45 ships in the two directions.

1.2 Returns and outcome from the New Suez Canal (Suez Canal Authority, 2019a):

In general Suez Canal is considered one of the main incomes to Egypt. The Suez Canal contributes 10 percent to the total international trade, 24.5 percent to international containerization trade and 100 percent to Asian and Europe containerization trade (egypt today, 2019). The expected benefits of the New Suez Canal are:

- Increase the Suez Canal revenues from $ 5.3 billion at present to $ 13.226 billion in 2023; an increase equal to 259% that shall positively contribute to Egypt's national income of hard currencies;
- Create job opportunities for people living at the Canal Zone, Sinai, and neighbouring governorates; and creating new urban societies as well; and
- Maximize competitiveness of the Suez Canal, excel its ranking among other alternative canals, and world classification societies due to the high rate of safety accomplished during transits.

1.3 Squat phenomenon

The phenomenon of squat is caused in shallow water when the clearance between a ship's keel and the seabed decreases. A combination of the sinkage and trim angle variation in shallow water is called ship squat (Barrass and Derrett, 2012). In the first place this phenomenon occurs due to appreciable change in potential flow around the hull. If the ship is considered as being at rest in a flowing stream of restricted depth, but unrestricted width, the water passing below it must speed up more than in deep water, with a consequent great reduction in pressure. As per Bernoulli's theorem (Larsson and Raven, 2010), if the flow velocity Vs increases in a flowing liquid, the pressure in the region decreases. As the pressure P at the bottom of the ship decreases, the ship needs to react in some manner to compensate for this. Ships float because the net forces acting on the

ship are zero because the force of gravity equals the force of buoyancy. This drop in pressure is compensated by the sinkage of the vessel as the direction of this force (low pressure) is downwards (see Figure 4). If, in addition, the water is restricted laterally, as in a river or canal, these effects are exaggerated. A reduction in ship speed may be observed when a ship enters a shallow water condition. A drop in speed may be up to 30% upon entering shallow waters and may rise up to 60% if the ship is advancing through a confined channel such as a river or a canal (Barrass and Derrett, 2012). It should be noted that this reduction in speed is not only due to the increase in resistance, but also due to the change in the manoeuvring features of the vessel as it entes a shallow water area as pointed out in (Tezdogan et al., 2016a).

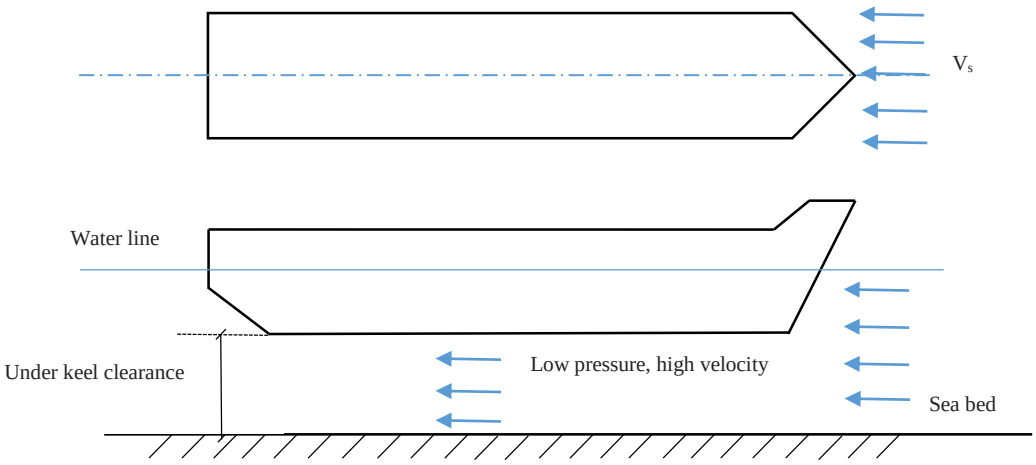

Figure 4 Squat effect on ships in shallow water

The ship squat phenomenon has been known for some time. Accurate determination of ship squat is required when navigating vessels through shallow water regions, such as rivers, channels and harbours. More than 117 ships have been reported as grounded over the past 40 years, mostly due to squat as pointed out in (Barrass and Derrett, 2012). In 1992, QE2 was grounded due to flooding of the tanks in the bow (Kazerooni and Seif, 2014). This was due to extreme squat and draft in the ship forepeak, with the financial loss evaluated at £20 million. These examples demonstrate that accurate prediction of ship squat is essential.

More recently, some grounding of ships in the Suez Canal have been recorded and published in World Maritime News (from World Maritime News website, March 2016).

A 163,038 DWT oil tanker ran aground 159 km into the Suez Canal in May 2016. Similarly, a 182,307 DWT bulker called Eibhlin ran aground during its transit of the Suez Canal with the Southbound convoy.

Finally, in April 2016, a 153,514 DWT containership MSC Fabiola had a similar fate. For this reason, it is very important that the Suez Canal authorities have accurate prediction data for ship squat to minimise the risk of grounding for ships.

In the present study a model scale of the Kriso Container Ship (KCS) was used to study squat characteristics and resistance in shallow water and restricted water. New Suez Canal was used as a typical navigation route for the present study. Container ships are recorded as the most common type of ships crossing the Suez Canal. As shown in Figure 5 and Figure 6, respectively, container ships make up 30% of the total ship number passing through the canal and in terms of net tonnage they constitute more than 50% of total net tonnage of ships in the canal per year (Suez Canal Authority, 2018). For these reasons the KCS, a well-known container ship model, was chosen in this study to provide realistic study of squat phenomena in the New Suez Canal.

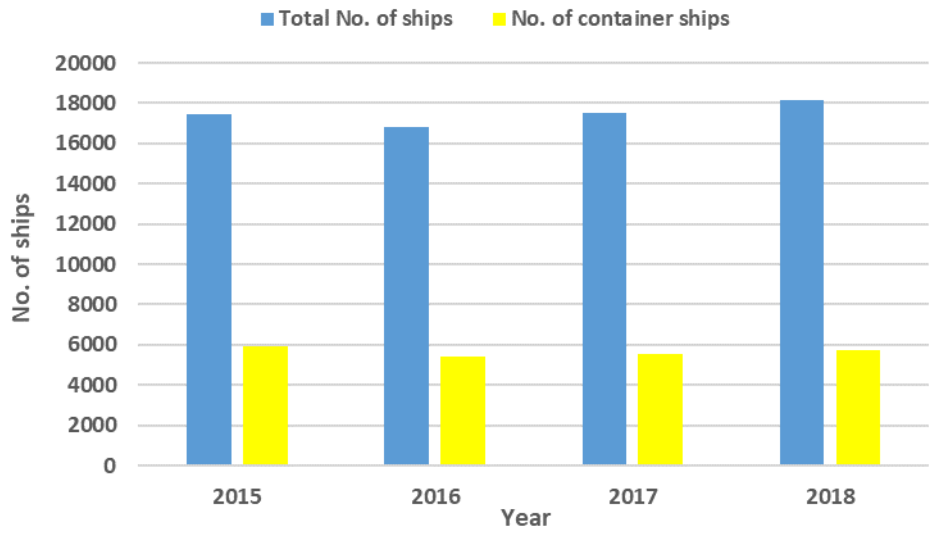

Figure 5 Navigation statistics for number of ships crossing the Suez Canal (Suez Canal Authority, 2018)

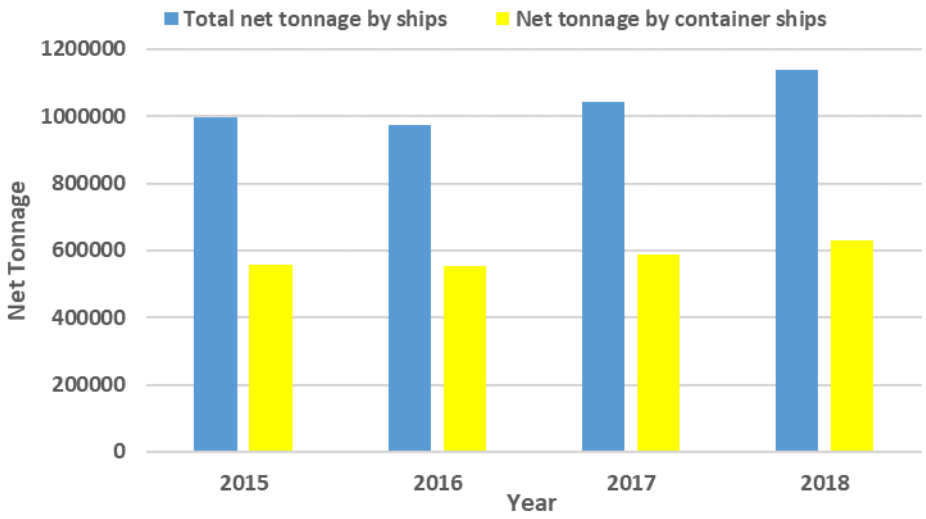

Figure 6 Navigation statistics for net tonnage by ships (Suez Canal Authority, 2018)

1.4 Motivation behind the work

The New Suez Canal, recently opened for international navigation in August 2015. It is important to obtain accurate prediction data for ship squat to minimise the risk of grounding in this canal.

Some grounding of ships in the Suez Canal have been recorded and published in World Maritime News (from World Maritime News website, March 2016). A 163,038 DWT oil tanker ran aground 159 km into the Suez Canal in May 2016. Similarly, a 182,307 DWT bulker Eibhlin ran aground during its transit of the Suez Canal with the Southbound convoy. Finally, in April 2016, a 153,514 DWT containership MSC Fabiola had a similar fate. For this reason, it is very important that the Suez Canal authorities have accurate prediction data for ship squat to minimise the risk of grounding for ships.

On the other hand, no study has looked into the effect of different water depth to ship's draft ratios on ship squat and resistance in the New Suez Canal. Moreover, no experimental study has been performed to investigate the effect of critical blockage ratio sinkage, trim and resistance in the New Suez Canal. Also, no experimental study has been performed to measure the resistance and sinkage variations with speed, water depth and loading conditions under different trimming angles to detect the best trim angle for ships

during sailing in the New Suez Canal to reduce resistance and therefore fuel consumption. Finally, no study has been conducted to study the blockage effect on the ship hydrodynamic performance in the New Suez Canal.

1.5 Research Aims and Objectives

The main aim of this dissertation is to perform the hydrodynamic analyses of a container ship in shallow and restricted waters, *including* the New Suez Canal, to predict the ship's performance and behaviour in these shallow water regimes through a suite of experimental, analytical and numerical methods. In order to achieve this aim and the specific objectives as given below, an extensive experimental campaign was performed at the University of Strathclyde's Kelvin Hydrodynamic Laboratory. In addition to Experimental Fluid Dynamics (EFD), a Reynolds Averaged Navier-Stokes (RANS)-based Computational Fluid Dynamic (CFD) technique was developed to numerically investigate the shallow water hydrodynamics of the ship in question. The numerical and experimental results were also compared to those from slender body theory and a set of empirical formulae. The specific objectives of this thesis are formulated as follows:

- ✓ To review the available literature on squat of ships and to investigate the differences between various prediction techniques.
- ✓ To perform a series of experiments on a model scale of the KRISO Container Ship (KCS) in shallow water and restricted water (including the New Suez Canal).
- ✓ To gain a better understanding of the effects of the water depth to ship draft ratios at various ship speeds on the squat phenomena and ship resistance in slope and rectangular canal.
- ✓ To study the blockage effect on ship resistance and squat.
- ✓ To determine a form factor value for the KCS at various water depth to ship draft ratios.
- ✓ To detect the best trim angle for ships sailing in restricted waters to reduce resistance and therefore fuel consumption.
- ✓ To introduce a CFD-based RANS simulation model to predict the resistance and squat of the ship operating in shallow and restricted water.

- ✓ To predict the squat and resistance of a vessel advancing through a Suez Canal using this RANS solver.
- ✓ To make a comparison between different methodologies (experimental, numerical, analytical and empirical) for the prediction of ship squat and resistance on KCS model in sloped and rectangular canal.

1.6 Methodology

This thesis relies predominantly on experimental methods. However, additional approaches are incorporated within the final chapter to assess their performance. These include numerical (CFD), potential theory (Slender body theory), and empirical formulae.

The hydrodynamic performance of the ship in shallow water is assessed by:

- To assess the influence of depth to draught ratio, the canal bathymetry is varied systematically over a range of speeds. Additionally, the effect of blockage is determined by changing the canal width, thus, influencing the restriction level.
- To identify the optimum trimming angle of the ship, the initial trim is varied by bow and stern in conditions…
- To gauge the performance of the numerical, empirical and potential methods mentioned previously, their performance is assessed against the experimentally obtained data from Chapter 3. Two canal bathymetries are assessed over a range of depth Froude numbers as case-studies. To perform the assessment, the theory developed by Beck et al., (1975) and Tuck (1967a, 1966) is used. The theory is solved via the in-house code, as examined in Terziev et al. (2019a). In order to solve the potential flow around the ship in the New Suez Canal, a modification is applied to the aforementioned theory. Specifically, the equivalent blockage of the canal is used to replace the sloping canal sides of the New Suez Canal. In terms of resistance, the RANS solver Star-CCM+ is used. To numerically predict the wave resistance and form factor of the ship in the experimentally examined cases, double body simulations are used alongside multiphase cases. The pros and cons of the methods used in this thesis are shown in figure 7.

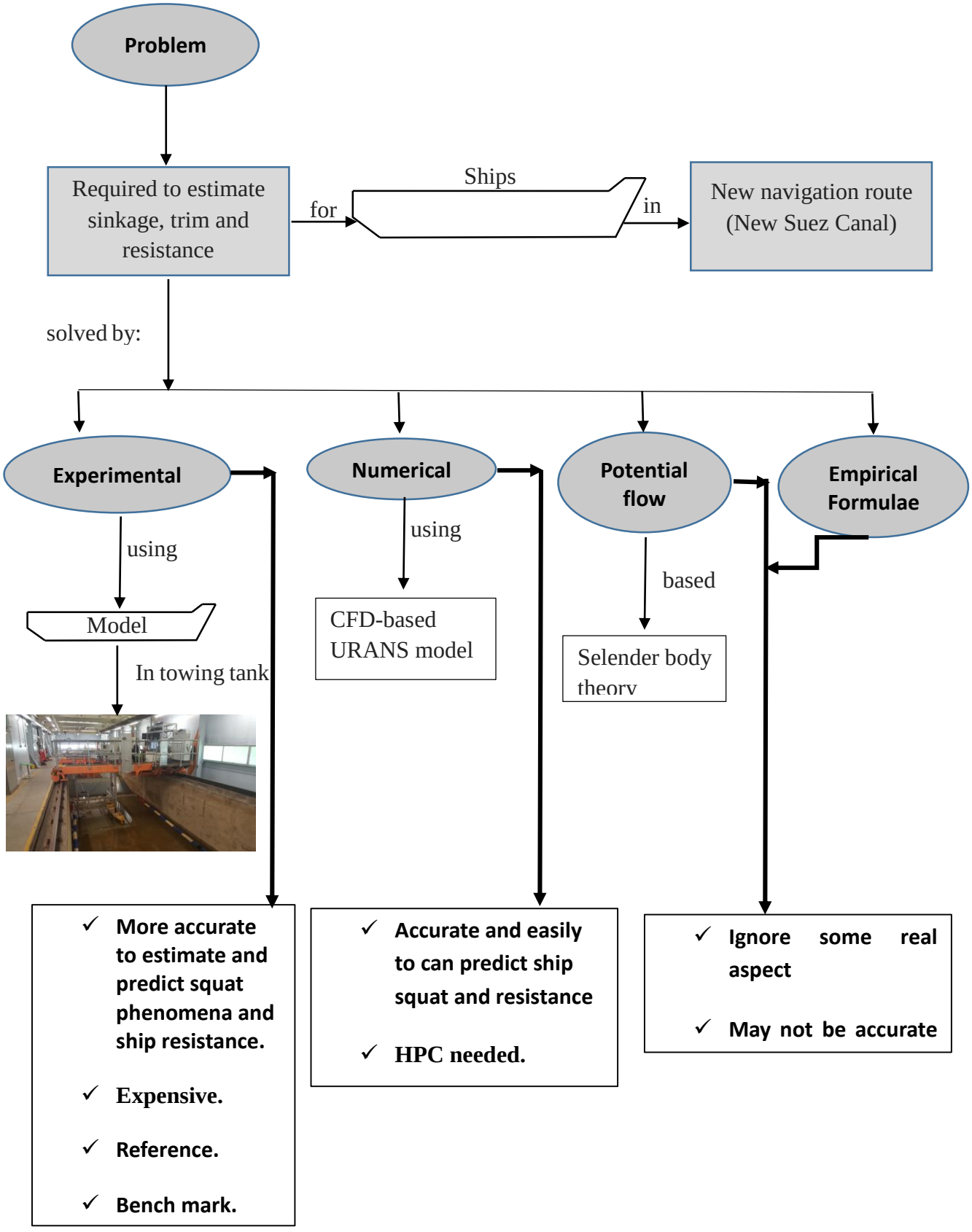

Figure 7 the methodology followed in this thesis

1.7 Research gap and novelty

1. The findings from this study concerning the New Canal is novel in the sense that it is the first study of this nature to be carried on the added new extension of the existing Suez Canal.
2. The present study was carried out following the introduction of the New Suez Canal to show that the Suez Canal is still a more feasible and attractive route for worldwide marine transport than other competitive routes (e.g. North Pole, Cape of Good Hope, etc….). To the best of the authors knowledge, no similar study exists, examining the hydrodynamics of ships advancing through the new Suez Canal.
3. This thesis will investigate the squat and Resistance of Ships Advancing through the New Suez Canal. To the best of the author knowledge, the novelty of the study is expressed in:

    - ❖ Resistance, and squat of a containership advancing through the new Suez Canal was determined by a series of experiments on a model scale of the KRISO Container Ship (KCS) to measure its sinkage and trim at various water depth to ship draft ratios and different ship speeds.

    - ❖ Effect of different trimming angle on the resistance and squat of a ship advancing in the New Suez Canal. It was determined, the loading condition level trim recorded the higher sinkage and lowest total resistance values at high speed.

    - ❖ Effect of blockage effect of a ship advancing through the New Suez Canal It was determined, the change in the blockage factor results in reducing the critical depth Froude's number for deep water operation

    - ❖ A holistic overview of an empirical, analytical and numerical techniques, with experimental validation of a ship advancing through the New Suez Canal.

1.8 Thesis Structure

The structure of this thesis is summarised briefly below.

- Chapter 2 (CRITICAL REVIEW) presents a detailed literature survey on the current techniques developed to predict the ship squat and resistance for vessels in shallow water and restricted water. It first outlines the historical development of modern prediction methods, and then provides potential flow, numerical and experimental methods to predict the squat phenomena. Finally, the chapter presents a literature survey on the specific areas that will be discussed in the main chapters of this thesis.
- Chapter 3 (EXPERIMENTAL ANALYSIS OF THE SQUAT OF SHIPS ADVANCING THROUGH THE NEW SUEZ CANAL) present, a series of experiments on a model scale of the KRISO Container Ship (KCS) to measure its sinkage and trim at various water depth to ship draft ratios and different ship speeds. Additionally, the blockage effect is studied at different water depth to ship draft ratios. Furthermore, deep water tests are performed to compare the results against shallow water test.
- Chapter 4 (AN EXPERIMENTAL INVESTIGATION OF THE TRIM EFFECT ON THE BEHAVIOUR OF A CONTAINERSHIP IN SHALLOW WATER) presents a series of model tests measuring the resistance, sinkage and trim variations with speed, water depth and loading conditions under different trimming angles in order to predict the best trim angle for ships sailing in restricted waters to reduce resistance and therefore fuel consumption.
- Chapter 5 (NUMERICAL STUDY ON HYDRODYNAMIC PERFORMANCE OF SHIPS ADVANCING THROUGH DIFFERENT CANALS) presents a focus study on rectangular canals or channels cross sections. The empirical, analytical, numerical and experimental techniques are utilised to predict the ship squat and resistance of the ship in question for New Suez Canal by using KCS model scale. This chapter will attempt to fill this gap by modelling the Suez Canal and a rectangular canal for reference. Wave resistance and form factor of the ship will be predicted by using CFD simulations to run in both multiphase and double body conditions.

- Chapter 6 (CONCLUSIONS AND FUTURE RESEARCH) provides a discussion of how this thesis has contributed to existing knowledge, and assesses how well the aims and objectives have been achieved. It also makes suggestions for future research.

Chapter Two

2. CRITICAL REVIEW

The following section is devoted to provide the necessary background in the field of shallow water hydrodynamics with a focus on resistance and squat. Potential flow, numerical and experimental methods are examined sequentially to place the present thesis into context. Each chapter also contains a separate, smaller topic-specific background.

2.1 Background

There are various methods available to predict ship squat and resistance in shallow water. These methods include empirical formulae, analytical, numerical and experimental methods. Empirical formulae can quickly estimate the squat according to the ship dimensions, ship coefficients, ship speed and water depth. These formulae are obtained from a series of model tests, but these formulae still have certain conditions and constraints to be satisfied before they can be applied. The analytical method mainly uses assumptions based on simple potential theory such as slender body theory. The numerical method or Computational Fluid Dynamics (CFD) methods have been more recently developed and can be easily used for predicting ship squat. The experimental methods are more accurate to estimate and predict squat phenomena.

There are four main parameters influencing ship squat. These are the blockage factor (K), the block coefficient (CB), the ship's velocity (V), draft (T) and water depth (H). The blockage factor can be defined as the ratio of the submerged midship cross-sectional area and the underwater area of the canal or channel (Figure 8). This dimensionless parameter is utilised in calculating ship squat by empirical formulations, and is given in Eq. (1) (Barrass and Derrett, 2012):

$$K = \frac{B \times T \times C_M}{W \times H} \tag{1}$$

where B is the ship's breadth, T is the ship's draft, W is the average canal's breadth, C_M is the midship area coefficient and H is the water depth of the water.

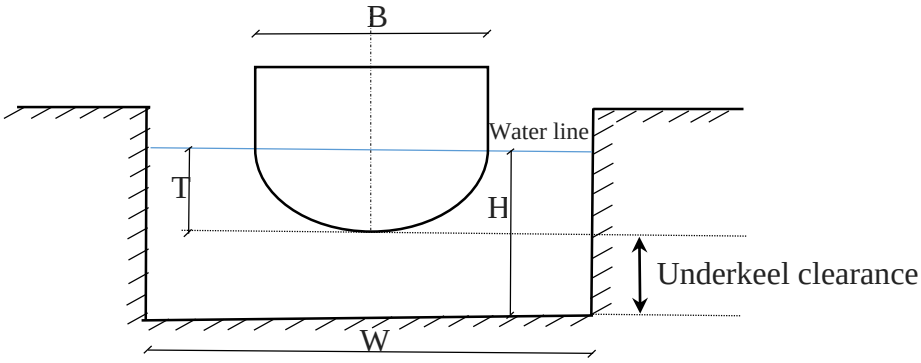

Figure 8. Ship in a canal

A second effect of ship squat is that changes in a ship's wave pattern which occurs when passing from deep water to shallow water (Terziev et al., 2019a). Michell (1898) developed a thin-body method to predict the wave resistance of a ship moving in shallow water. This method, henceforth referred to as the slender body theory, is based on fundamental assumption that the ship's beam is small compared to its length. As a consequence, the waves generated are also of small amplitude, which allows the linearisation of the free water surface.

Later Joukovski (1903) derived a similar formulation of the problem independently. The changes in a ship's wave pattern have been studied by Havelock (1924) for a point pressure impulse travelling over a free water surface. Havelock examined the wave patterns in shallow water by taking into account the speed of the vessel, and the depth of water, which led to the introduction of the depth Froude number (Fn_h), Eq. (2).

$$Fn_h = \frac{V}{\sqrt{gH}} \tag{2}$$

where V is the speed of the vessel (m/s), g is the acceleration due to gravity (m/s^2) and H is the water depth (m).

The depth Froude number can be thought of as the ratio of the ship's speed to the maximum wave velocity in shallow water of depth H. The well-known Kelvin wave pattern resulting from moving objects in water can be observed for $Fn_h < 0.57$ (Tezdogan et al., 2015). As the ship's velocity increases, the lateral wave lengths will increase and the angle of the wave pattern theoretically approaches 90 degrees until Fn_h becomes 1

(Tunaley, 2014), which is called the critical speed. When the depth Froude number is greater than one, the angle of the wave pattern begins to decrease again (Terziev et al., 2019a). The terms subcritical and supercritical speed are used for vessels propagating at $Fn_h<1$ and $Fn_h>1$, respectively. Of greater practical interest is the former scenario, namely when the depth Froude number is smaller than 1 (Beck et al., 1975).

The wave pattern is enclosed between straight lines having angles equal to 19 degrees and 28 minutes (as can be seen in Figure 9) when the Froude number is less than 0.4 (subcritical speeds). The angle of the wave pattern increases and approaches 90 degrees (as seen in Figure 9b) when the Froude number is equal to 1 (critical speeds). The angle of the wave pattern begins to decrease again (as seen in Figure 9c) when the Froude number is more than 1 (supercritical speeds).

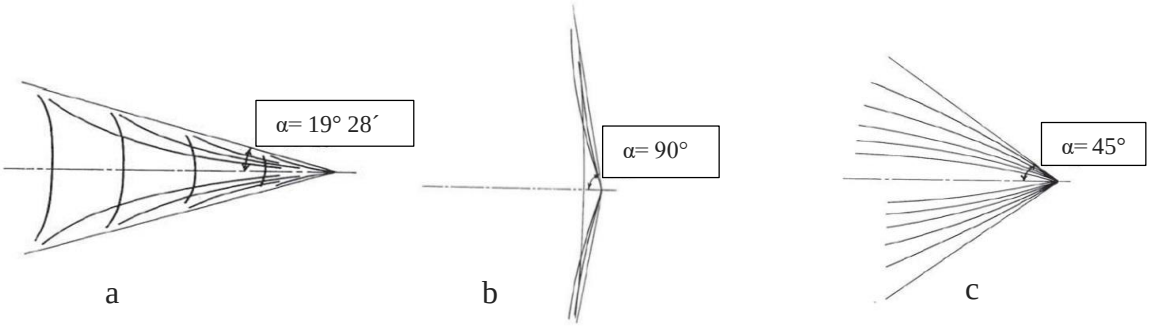

Figure 9 Wave pattern a) $Fn_h < 0.4$, b) $Fn_h = 1$, c) $Fn_h > 1$ (Larsson and Raven, 2010)

2.2 Potential flow-based methods

Many researchers have investigated ship squat in restricted water. Kreitner (1934) calculated ship squat using a one-dimensional hydraulic theory. He showed that the equation for the flow velocity in a canal ceases to provide reasonable solutions as the critical speed is approached. Constantine (1960) studied the different behaviour of ship squat for various ship speeds (subcritical, critical and supercritical), as well as the ratio of midship section to the cross section of the fairway. He determined that laterally restricted waterways have substantial effect on the dynamic squat of a vessel.

Inui (1954) investigated the effect of shallow water and restricted water on the wave-making resistance of ships. He concluded that higher degrees of discontinuity in the wave-resistance of a ship are caused by an increase in the restrictions of a waterway. This

showed that the resistance itself is not a continuous function of depth Froude number in the case of restricted shallow waters.

Tuck (1966) reproduced Michell's linearised slender-body theory and explored the scenario where a ship is travelling in shallow waters of constant, unrestricted width. Tuck (1966) solved for the hydrodynamic forces in shallow water to calculate the sinkage and trim for sub-critical and supercritical speeds by using matched asymptotic expansions. He validated the results with model-scale experiments which showed good agreement for depth Froude number smaller than 0.7. However, the theory fails as depth Froude number equal to 1 because the formulations used become singular. Trim is the leading factor in the supercritical range, while sinkage is predominant in the subcritical range. Regarding resistance, the method predicts zero resistance in the subcritical range.

Tuck (1967a) analysed the effect of restricted channel width in addition to depth on ship behaviour. (Beck et al. (1975) expanded on the Tuck's work to account for vessels in dredged canals with an unrestricted shallow water region of constant depth extending infinitely on either side of the dredged section on the channel.

Beck and Tuck (1971) computed the heave and pitch motions of Series 60 ship using the slender body theory in shallow water for unconstrained ship. At zero forward speed The calculations have shown that mooring forces have very little influence on pitch and heave motions. Results are compered with others zero angle head sea.

Gourlay (2008) obtained a general Fourier transform method to calculate the sinkage and trim of a ship advancing in unrestricted shallow waters, canals and stepped channels as well as channels of arbitrary cross-section. He focussed on the subcritical range of motion. Gourlay (2008) extended his modification of the slender-body theory to calculate the sinkage and trim of a fast displacement catamaran propagating through horizontally unrestricted shallow water, which was valid for all speed regimes.

Then, Gourlay (2008) showed that trim, resistance and sinkage are affected by a change in the spacing between the catamaran hulls. In addition Gourlay (2008) used a theoretical method based on the linear superposition of slender-body shallow-water flow solutions to predict the sinkage and trim of two moving ships as they pass each other, either from opposite directions, or one ship overtaking the other.

The slender body theory has well-known singularity near critical depth Froude numbers. This stems from the fact that equations, used in the theory contain a term subtracting the depth Froude number and unity. Thus, when the critical speed is approached, the theory predicts infinite trim and sinkage. Gourlay and Tuck (2001) presented a trans-critical theory, where the above-mentioned singularity was removed. They did so while preserving the linear form of the solution. On the other hand, Lea and Feldman (1972) arrived at a nonlinear form when attempting to resolve the same problem.

There are several research papers, dealing with the singularity at the critical limit. These include nonlinear theories for uniform shallow water and canals (Alam and Mei, 2008; Mei, 1976; Mei and Choi, 1987). Alternatively, recent contributions to the subject seem to focus more attention on the super and subcritical modes of motion, rather than the critical limit (Deng et al., 2014; Z. Zhang et al., 2017; Zhang et al., 2015). Although these predict a similar singularity to Tuck's (1967, 1966) method, they contain nonlinear and dispersive effects.

A surprising consequence of the formulation of Beck et al. (1975) is that it can predict wave resistance for mixed flows. That is, the equations predict a component in the resistance due to waves of the ship once the exterior flow of the ship has exceeded a depth Froude number of 1. The accuracy of this prediction has not been examined since the publication of the work of Beck et al. (1975). The same authors predict that when if the critical velocity in the exterior region is reached and maintained, the ship will behave as if it is located in a canal of width, equal to the interior region. This is a consequence of the fact that the inviscid formulation predicts that the pressure field at the edge of the step is maintained to infinity, and prevents flux across it. The effect of this assumption was also examined by Terziev et al. (2019a). Their results suggest that while resistance may be higher in a canal, the sinkage and trim in a critical exterior flow case is larger.

Janssen and Schijf (1953) predicted the unstable squat positions for ships. Yao and Zou (2010) tested their theory for a Series 60 hull (C_B=0.6). They calculated the shallow water effects in terms of sinkage, trim, resistance and wave patterns for sub- and supercritical speeds on a ship by discretising the hull by a panel method. They distributed free and wall surface panels onto which Rankine sources of constant strength are mapped. They validated the results with experimental results and the validation was in good agreement.

Sergent et al. (2015) estimated the unstable equilibrium position of a ship during heave motions as a function of canal and ship parameters by using a new mathematical expression from a 2D analytical model. One of the few potential flow theories, capable of predicting the six degree of freedom motion of a ship in shallow water was derived by van Oortmerssen (1976). He used a potential flow-based approach and distributed discreet three-dimensional sources to describe the flow. He obtained the responses of a ship as a result of incident harmonic waves. Furthermore, his method made it possible to account for the presence of a quay. The theory of van Oortmerssen (1976) suggests that viscous effects are magnified as the water depth is decreased.

Separate theories to predict shallow water ship motions are required for several reasons. Deep water strip theory is highly successful in all modes of motion except roll, where viscous effects dominate. In shallow water, all 6 degrees of freedom are influenced substantially by viscosity, which has motivated separate theories to calculate the behaviour of two- and three-dimensional bodies (Beukelman and Gerritsma, 1982).

A related problem is that of manoeuvring in shallow water, as examined by many authors (Liu et al., 2015). The expansion in ship size has meant that ship manoeuvring in shallow water is now a critical factor that must be assessed. The proximity of the seabed can have an adverse effect on manoeuvring characteristics rendering the ship incapable of performing the required operations in extreme cases (Millward, 1996; Mucha, 2017). For example, it has been shown that the tactical diameter of a ship increases substantially with decreasing water depth (Toxopeus et al., 2013).

Similar investigations have taken place to predict the forces and moments, resulting from the interactions between two ships (Gourlay, 2009). Later, Yuan and Day (2015) presented a technique to optimise the distance between two ships in an attempt to minimise the adverse hydrodynamic interactions. They did this by modelling the far field waves of translating and oscillating point sources. The result was further validated using a 3D Rankine source method and an application on the Wigley hull form.

Yuan et al. (2015) presented a Doppler-shift theory to model the waves generated by a translating and oscillating source at the free surface. They applied this theory to predict a variety of wave parameters and patterns using their developed theory. Later, Yuan et al.

(2016) applied their Doppler-shift theory to the interactions between two ships. Their validation showed good agreement with experimental results.

Feng et al., (2016) developed a Rankine source method which utilises the continuous distribution of source panels along the free and seabed surfaces. In this way, was not required to solve a singularity, which facilitated the investigation performed by Feng et al. (2016) into the performance characteristics of a 2-D structure experiencing a forced oscillation, by removing any additional assumptions. To show the effect the proximity and topology of the seabed, several scenarios were investigated in their research article, including a deep water case-study, flat bottom shallow water, and various uneven bottom topologies. One of the key findings made by Feng et al. (2016) was that the mean water depth is a key parameter influencing the hydrodynamic performance of a body in shallow water

Calisal and Alidadi (2011) conducted a numerical study to predict the squat of the Wigley hull. A slender-body theory approach was utilised to convert the three-dimensional ship problem into a series of 2-D cross sections distributed from the bow to the stern at equal intervals. They applied a boundary element method sequentially to each cross section to obtain the disturbance potential. By integrating the pressure over the hull, the forces acting on the hull were derived, which were then used to estimate the squat. A validation study was performed which compared the numerical results with those recorded from experiments at several speeds. The results between the two sets of data were agreeable.

Ha and Gourlay (2017) developed a sinkage coefficient by using a slender body theory in open shallow water and applied the theory to 12 published hull forms: (the DTC, KCS, JUMBO, MEGA-JUMBO, FHR Ship D, and FHR Ship F for container ships; the KVLCC1 and KVLCC2 for oil tankers; the Japan 1704B, JBC, and FHR Ship G for bulk carriers; and the KLNG for membrane LNG carriers). They suggested limitation on the use of the coefficients, based on ship and navigation channel dimensions.

Delefortrie et al. (2010) investigated ship squat when a ship is sailing in a muddy area. They used a mathematical model predicting fairly well the ship’s squat for container carriers, taking into account the bottom conditions and propeller action. Delefortrie et al. (2010) observed that sinkage is mostly smaller when a mud layer is present for a same small under keel clearance referred to the solid bottom.

Gourlay (2013) investigated a ship squat problem in a non-uniform water depth. He used slender-body shallow-water theory for transverse depth variations. Moreover, he discussed the obtained results for ships transiting through canals such as the new Panama Canal and the effect of channel width on ship squat. Gourlay (2013) showed that the midship squat in a typical dredged channel can increase by 20% compared to that in open water of the same depth, while dynamic trim is essentially unchanged. Furthermore, in canals such as the new Panama Canal, midship sinkage can be 100% larger than that in open water of the same depth.

Gourlay et al. (2015) investigated the dynamic sinkage and trim for different container ships by using two potential flow-based methods (slender-body method and Rankine-source method). Their study revealed that slender-body theory is able to give good predictions of dynamic sinkage and trim in wide canals or open water, while Rankine-source methods offer an accurate solution particularly for ships at high speed in narrow canals.

Finally, Empirical formulae can quickly estimate the squat according to the ship dimensions, coefficients, speed, and underwater topology. These formulae are typically obtained from a series of model tests. Alternatively, analytical methods have been developed by researchers that make use of the assumptions inherent in potential flow theory such as slender body theory (Tuck, 1966).

2.3 Numerical methods

Nandhini and Nallayarasu (2019) investigated ship to ship interactions via a RANS approach. Their methodology neglected the free surface, rendering their analysis of double body type. This was justified in their paper due to low speeds analysis being carried out in their study.

A CFD approach was also used by Wang and Zou (2014), to investigate the hydrodynamics effects of a berthed ship and a passing ship entering and leaving a single way lock. They conducted numerical simulation of the three-dimensional unsteady viscous flow around the two ships a using the k – ε. turbulence model by solving the unsteady RANS equations. They analysed the influences of the ship speed, water depth,

transverse and longitudinal positions of the berthed ship on the ship–ship and ship– lock hydrodynamic interaction. The results show that when the ship speed increase and the water depth decrease the magnitude of hydrodynamic forces increases. However, the transverse and longitudinal positions of the berthed ship have no significant effect on the hydrodynamic forces on the passing ship when the ship is entering or leaving the lock chamber.

According to Terziev et al. (2019b), the $k - \varepsilon$ turbulence model is one of the most frequently used method to simulate turbulence in ship hydrodynamics. They performed a series of tests on the turbulence models in shallow water and comparing the integral outcomes with experimental results. The results are analysed via a modified bivariate plot, which reveals a strong candidate for the optimum choice of turbulence modelling.

Sherbaz and Duan (2014) used a numerical method to assess a trim influence of MOERI container ship resistance in deep water. The study showed that trim has pronounced increasing effect on resistance during bow trim. Furthermore, the effect on resistance is varying during stern trim and optimum trim point is 0.02m trim by stern. Ji et al. (2012) performed numerical simulations by solving the 3-D Navier-Stokes equations along with the standard k-ε turbulence model. They simulated wave patterns, induced by moving convoys composed of one or two barges in restricted waterways in order to predict the relationship between geometric and kinematic parameters, as well as the amplitude of ship-generated waves, and the water plane drawdown.

Tezdogan et al. (2016) predicted the squat and resistance of a model scale container ship advancing in a canal using a numerical method based on nonlinear unsteady RANS simulations. One of the findings of Tezdogan et al. (2016) include the fact that the initial draught is highly influential on the attained squat. Specifically, an increased initial draught can lead to markedly different squat values. They also examined the effect of a slopped canal on the wave pattern, which revealed drastic changes depending on the ship speed.

Terziev et al. (2018) presented a numerical study to investigate the sinkage, trim and resistance of ships by using a scale model of DTC container ship advancing through restricted shallow water in four channels with different cross sectional area and ship speeds. They used Computational Fluid Dynamics (CFD), the slender-body theory and

various empirical methods to calculate the trim and squat of a containership advancing through different channel geometries. Terziev et al. (2018) examined the effect of channel dredging on the performance and behaviour of the DTC by modelling the flow numerically in different channels. Their findings relate to the level of restriction present in the channel. Furthermore, their case-studies incorporated a canal case, as well as an open water case for reference. Differences in sinkage, trim and resistance are demonstrated based on the restriction of the channel.

Varyani (2006) conducted a numerical study with a bulk carrier and a high speed craft in shallow water to assess the sinkage and trim of these ships at different depths. He concluded that the inviscid theory used provides results with decreasing accuracy as speed increases. He attributed this to the omission of viscosity. Viscous effects are thought to govern the shallow water phenomena in the high speed range, whereas their importance is smaller at low speeds (Terziev et al., 2019a).

Sakamoto et al. (2007) performed CFD simulations with the Wigley hull in deep and shallow water. Their investigation featured high speeds, as well as a validation with experimental data. As part of the abovementioned study, deep water wave patterns were compared to the equivalent shallow water case-studies. Following this, Jachowski, (2008) carried out a study on the assessment of ship squat in shallow water employing Fluent, a commercial RANS solver. He used a model scale KCS to calculate its squat for several water depths at different ship speeds. Then, Zou and Larsson, (2013), using a steady-state RANS solver (SHIPFLOW), performed a numerical study on the ship-to-ship interaction during a lightening operation in shallow water. They used an Aframax tanker and the KVLCC2 in model scale, both appended with rudder and propeller.

Alderf et al. (2008) developed a new method for the numerical modelling of dynamic squat by using a finite element method. Alderf et al. (2008) also illustrated the effect of sea floor topology on a ship sailing at critical speed. This model can give results for the dynamic responses of a ship in highly restricted canals on any seafloor shape. He developed this model to validate the stability model as an extension of the method proposed by Janssen and Schijf (1953).

Zaghi et al. (2011) explored wave interference effects of a catamaran both experimentally and numerically. Their findings include the fact that with reduced separation distance

between the two demihulls, the resistance is magnified. Cross-flow was also shown by Zaghi et al. (2011) to be increased in the most narrow configuration of the two hull of the catamaran. The researchers also demonstrated cross flow changes with speed.

(Toxopeus, 2013)They in investigated the flow around manoeuvring ships by using CFD tool in deep and shallow water using KLVCC2 model. they verify and validate the prediction of the influence of the water depth on the flow field and the forces and moments on the ship for a full-block hull form. The CFD results give insight into the forces and moments acting on the ship as a function of the drift angle, yaw rate and water depth. A clear dependence of the forces and moments on the water depth is found for steady drift conditions.

Prakash and Chandra (2013) studied shallow water effects on a river-sea ship using a RANS solver. They simulated the vessel advancing at a variety of speeds and predicted the resistance and wave patterns. They concluded that the RANS approach can successfully be applied to problems in shallow water hydrodynamics.

Then, (Wortley, 2013) studied the squat and resistance of the DTC container ship model using a CFD-based RANS solver, OpenFOAM. He also compared his CFD results to the experimental findings, reporting that OpenFOAM overestimates drag forces, especially the wave resistance, due to the generation of a coarse mesh in the domain. He noted that the squat and trim results of a ship model in a canal obtained using CFD are much larger than the experimental results. These authors believe that his numerical setup should be improved and reconsidered, in order to obtain results that are more compatible with experiments.

(He et al., 2015) investigated the interference effects of wave systems on a catamaran in shallow water. They used CFDShip-Iowa as a RANS solver to calculate the resistance and the interference factor of the DELFT catamaran in two separation distances at various water depths.

Castiglione et al. (2014) investigated the interference effects in shallow water, resulting from the presence of a catamaran. They studied a range of separation distances and speeds, incorporating both sub and supercritical regimes. Their RANS simulations indicate that near the critical speed, shallow water effects are significantly magnified.

Furthermore, the speed at which the resistance hump occurs is displaced earlier along the speed curve in extremely shallow waters.

Haase et al. (2016a) assessed the performance of a catamaran in finite waters using CFD in full-scale. The results showed good agreement, when compared to sea trial measurements. The abovementioned authors also concluded that resistance extrapolation techniques tend to overpredict the resistance in shallow water.

The work of Haase et al. (2016a) was presented to extend the work of Haase et al. (2016b), which focused on deep water catamaran performance and scale effects. They devised a novel methodology to scale a ship's resistance characteristics without an increase in the linear dimensions of the ship. Instead, the viscosity was altered to push the Reynolds number to its full-scale equivalent. Although this method shows promise in terms of savings in computational expense, it has yet to be applied widely.

Yao et al. (2011) presented a numerical study by using a first-order Rankine source panel method which was adopted to study the bank effects for a ship travelling along a rectangular and a sloping channels and shallow water. A ship model of 8 000 TEU container ship was used to predict the sway force and yaw moment acting on the hull during the ship model sailing with different forward speeds, different water depths and different distances between the bank and the ship hull. Yao et al. (2011) presented a study which can provide insight into the bank effects in the restricted waters. Furthermore, they gave practical guidance on ship manoeuvring and control to ensure navigation safety in restricted waterways.

Ma et al. (2013) investigated the viscous flow around a KCS model of hull-rudder system towed along a bank in shallow water by using numerical methods to solve the RANS equations. Furthermore, they calculated the hydrodynamic forces and moments acting on ship for different ship-bank distances and rudder angles. They showed that at low ship forward, the speed influences on the free surface elevation and ship squat are assumed to be negligible.

Zhou et al. (2013) summarised and introduced various methods for predicting ship squat in shallow water and shallow channel using theoretical approach which described by the existed empirical methods, empirical formulas and numerical calculation. Zhou et al.

(2013) conducted a numerical calculation for container ship KCS sailing with a constant speed in shallow water and shallow channel. The numerical results were validated with available experimental data and empirical methods. They proved that the squat is significantly affected by ship speed and water depth. Also they showed that the ship bank distance is an influencing factor.

Mucha et al. (2016) presented a validation study on numerical prediction of ship squat and resistance in shallow water. The numerical results were compared with experimental data for the well-known candidate ships (DTC, KCS and KVLCC2) at various water depths, speeds and drift angles. Mucha et al. (2016) performed two numerical methods one of them based on the solution of the Reynolds-averaged Navier-Stokes equations, and one based on slender-body theory by using a Rankine Panel method. They showed that the numerical methods are generally capable of predicting midship sinkage with good accuracy, while the boundary element methods (BEM) yield larger deviations in higher Froude depth number regimes, especially in predicting trim. For very shallow water ship flows ($h/T<1.2$), resistance predictions with viscous flow solvers were shown to be sensitive to near-wall treatment, the boundary condition on the tank bottom and the turbulence modelling. At high speeds, resistance in very shallow water conditions with RANS methods is still under-predicted. They concluded that the EASM turbulence model performed generally better than the k-ω SST model.

Shevchuk and Kornev (2017) applied computational method to predict the wake of an inland ship in model scale by using hybrid URANS/LES turbulence modelling methods in conjunction with the synthetic turbulence generation. They conducted a series of computations of the flow around the inland cruise ship to determine, how the fairway depth restriction and draft angle can influence the hydrodynamic exciters of ship stern vibration. Shevchuk and Kornev (2017) performed statistical analysis of the longitudinal velocity field in the propeller plane, thrust fluctuations and pressure pulses on the hull. They demonstrated that when the ship enters the restricted waters all the hydrodynamic sources of stern vibration are intensified. Moreover, the velocity fluctuations can reach 25% of the ship speed, the thrust fluctuations can be as high as 6.5% of the mean and the amplitude of the pressure pulses can increase to 8 kPa under certain conditions.

Pacuraru and Domnisoru (2017) performed numerical analyses by CFD RANS-VOF method in shallow water using the NUMECA / FineMarine software, free to sink and trim. These numerical analyses used to investigate the viscous flow around a barge hull in the case of the shallow water fluid domain. Pacuraru and Domnisoru (2017) concluded that significant influence of the shallow-water conditions on the barge resistance where the most significant ship resistance change was found at H/T=1.5, V=8.64 knots and V=9.7 knots. Moreover, they showed that for a standard operation speed (6.5 knots) the ship resistance increases from about 5% at H/T=4 to 44% at H/T=1.5. Finally, they provided practical technical recommendations for barge hull design.

(Bechthold and Kastens, 2020), they predict the sinkage and trim pattern by using a RANSE based CFD method for three container ships in confined water and extreme shallow water, for water depth to draft ratio of less than 1.2. The CFD predicted results has been compared with model test data to analyze the robustness of the CFD method and to evaluate the quality of the squat predictions. The presented RANS method is robust and the quality of the predicted squat values is better than 20% deviation. When both CFD and EFD share the same model setup, the prediction deviation is less than 10%.

(Zeng et al., 2019), they analysed the ship's frictional resistance for two types of ship in extremely shallow water by using Computational Fluid Dynamics (CFD) calculations. They show the Reynolds number and the geometry of the ship becomes essential to the prediction of ship's friction in extremely shallow water. The results show that the frictional resistance becomes smaller for certain ship types at the same Reynolds number when the water is shallower.

(Guo et al., 2019), they explored the mechanism and correction method of the blockage effect for KCS model by apply computational fluid dynamics techniques and ship resistance tests. They concluded that The blockage effect increases with the increase of the blockage ratio and Froude number. Moreover, the blockage effect causes hull sinking and trimming by the stern. Also The blockage effect increases the chaotic behavior and complexity of the flow field distribution around the hull.

(Xia et al., 2020), they studied the uncertainty quantification of hydrodynamic forces on the DTC model advancing in shallow water waves. First they compered a state-of-the-art method for uncertainty quantification problems, the non-intrusive polynomial chaos

(NIPC) method is introduced and validated to be effective by studying a stochastic function, together with the Monte-Carlo (MC) method, the, NIPC method is applied to quantify the uncertainty of the resistance, heave motion and pitch motion of the DTC model in shallow water waves. Computations are per-formed with the CFD software STAR-CCM+

Finally, numerical, or Computational Fluid Dynamics (CFD) methods have been more recently developed and can be easily used for predicting ship squat. Although this approach has its own limitations, such as the computational cost, and knowledge required to perform a simulation, it is rapidly gaining popularity (Stern et al., 2013)

2.4 Experimental methods

Elsherbiny et al. (2019b) conducted a series of experiments on a model of the KRISO Container Ship (KCS). The KCS performance was examined by measuring its sinkage, trim and total resistance. A wide range of water depth to ship draft ratios at various ship speeds were investigated. Additionally, the blockage effect was studied by varying the canal width, and deep water tests were performed. Also, the measured model resistance data was used to determine a form factor value for the KCS at various water depth to ship draft ratios. Estimation of experimental uncertainty was conducted for all tests.

Later, Elsherbiny et al. (2019a) presented a series of model tests measuring the resistance, sinkage and trim variations with speed, water depth and loading conditions under different trimming angles at 1:75 scale. This was done to examine the range of ship trim for safe and efficient sailing in restricted water in both depth and width, and to detect the best trim angle for ships sailing in restricted waters to reduce resistance and therefore fuel consumption.

Shivachev et al. (2017) investigated influence of trim on KCS ship resistance in deep and calm water using experimental and numerical methods. The study showed the model test and CFD method had good agreement in prediction of total resistance trend with respect to trim. Furthermore, the study confirmed that significant reduction in total resistance are achievable by operating the ship at optimum trim.

Lataire et al. (2012) conducted an experimental study for a model scale KVLCC2 to predict the squat for a wide range of water depths and widths of a canal with rectangular cross section.

Kazerooni and Seif (2014) measured and analysed the squat phenomenon through model tests with a tanker ship model and the Dhow model in a towing tank. The squat data was investigated and plotted versus under keel clearance for various Froude numbers. The model scales used were quiet small which affected the accuracy of the experimental results.

Mucha et al. (2018) investigated the bank effect on ship resistance and propulsion characteristics in restricted water of an inland waterway and the effects of water depth for various ship forward speed. Benchmark data for CFD for three water depths and three separation distances to a vertical wall at affixed shallow water depth for ship model was provided. Mucha et al. (2018) showed in their study that the hydrodynamic interactions between the model and flow restrictions related to squat and bank effects, as well as their impact on resistance and propulsion characteristics. The abovementioned study demonstrated that shallow waters have a significant impact on the propulsive capability of a ship. Benchmark studies such as the one mentioned here are invaluable because they enable the validation of numerical works which seek to increase the current understanding of the phenomenology of shallow water effects.

Later, Mucha et al. (2019) conducted physical tests of zig-zag manoeuvres at two different water depths. They performed the experiments to investigate a free-running manoeuvring inland waterway ship at extreme shallow water conditions and the effects of limited under-keel clearance. The study confirmed the manoeuvring behaviour of the ship in question changes at extreme shallow water condition, due to the strong hydrodynamic interactions between the ship's bottom and sea floor. This interaction leads to an increase in the forces and moments acting on the hull and dynamic changes of the floating position during manoeuvring. Mucha et al. (2019) concluded that the dynamic response characteristics in surge and sway for extreme shallow water were changed accordingly compared to the same manoeuvre in deep water.

Simonsen et al. (2013) performed CFD and EFD analysis of the KCS in head waves and in calm water for a variety of speeds. Their investigation demonstrated the versatility of

the CFD method when applied to replicate experiments. The experimental campaign was conducted in FORCE technology's towing tank in Denmark, where heave, pitch and resistance were measured. The numerical results showed good agreement with the experiments.

van Hoydonck et al. (2018) presented experimental and numerical study on the effects of ship to bank interaction, in which viscous-flow solvers are used to predict the hydrodynamic forces and moments on the ship. van Hoydonck et al. (2018) conducted shallow water model tests in a towing tank with KRISO Very Large Crude Carrier (KVLCC2) model. The forces and moments on the KVLCC2 model were obtained for various water depths and lateral distances to the banks. van Hoydonck et al. (2018) developed two different CFD codes to predict the loads on the model KVLCC2 as a function of the water depth and lateral position in the channel. They took into consideration the effect of propeller suction and free surface modelling. Moreover, comparisons between the EFD with CFD results from literature and potential flow computations were made. They concluded that when a ship model sails close to a vertical bank in shallow water, potential flow models are not able to accurately predict the bank effects, and viscous-flow methods have to be adopted to obtain the right trends of bank suction or repulsion.

2.5 Concluding Remarks

Up until this point, a substantial literature review has been made on existing ship squat prediction methods in restricted and shallow waters, and on other related topics which will be covered in the following chapters of this thesis. During this literature review, the following gaps in the literature have been detected:

i. No study has looked into the effect of different water depth to ship's draft ratios on ship squat and resistance in the New Suez Canal.
ii. No experimental study has been performed to investigate the effect of critical blockage ratio sinkage, trim and resistance in the New Suez Canal.
iii. No experimental study has been performed to measure the resistance and sinkage variations with speed, water depth and loading conditions under different

trimming angles to detect the best trim angle for ships during sailing in the New Suez Canal to reduce resistance and therefore fuel consumption.

iv. To date, studies performed on the squat and resistance of a vessel in a restricted canal or channel have not investigated the changing form factor and wave making resistance with change the depth Froude number.

The following main chapters of this thesis aim to fill these gaps listed above, using either experimental, potential flow theory and CFD methods.

Chapter Three

3. EXPERIMENTAL ANALYSIS OF THE SQUAT OF SHIPS ADVANCING THROUGH THE NEW SUEZ CANAL

To provide guidance for shipping in canals a series of experiments was conducted on a model scale of the KCS. The squat of the KCS was examined by measuring its sinkage and trim. A wide range of water depth to ship draft ratios at various ship speeds was investigated. Additionally, the blockage effect was studied by varying the canal width, and deep water tests were performed. The results indicated that for Froude's number based on depth (Fn_h) below 0.4, measured squat values are insignificant and do not change with either Fn_h or depth to draft ratio (H/T). The squat increases with H/T values for Froude numbers higher than 0.4. Moreover, a canal with reduced width had a negligible effect on squat, suggesting that the next segment of the Suez Canal can be built to a narrower width.

The container ship was primary chosen for this study for a number of reasons:

1. Container ships presents a quite large percentage of ships passing through Suez Canal.
2. Container ships recently are getting larger in size and their behaviour while navigating the New Suez Canal as related to trim, squat and increased resistance is quite important.
3. The findings and lessons learned from study can be used while dealing with other types of ships of similar size and dimensions.
4. The findings from this study concerning the New Canal are novel in the since that they are the first study of this nature to be carried on this added new extension of the existing Suez Canal. Comparison can be made regarding ship's behaviour between the 90 kilometer New Canal and its counter length of the existing Suez Canal.
5. The recent addition of the New Suez Canal took 150 years after inaugurating the existing Suez Canal (opened for world navigation in 1896).

6. It was necessary to carry out this study after the new introduction of the New Suez Canal to show that the Suez Canal is still more feasible and attractive route for worldwide marine transport than other competitive routes (e.g. North Pole, Cape of Good Hope, etc….).

3.1 Introduction

The experimental methods are more accurate to realistically simulate and predict squat phenomena. In this thesis, a series of experimental tests are carried out on a container ship model to study ship squat and resistance characteristics while navigating the New Suez Canal.

The New Suez Canal was opened on August 6th 2015 for international navigation. It will therefore be very useful to investigate the squat phenomena in the new part of the Canal to avoid any future problems that may arise due to the variation in the seabed depth and/or a vessel's speed. To the best of author's knowledge, no studies on this phenomenon are currently available in the open literature.

This chapter is organised as follows. Section 2 contains the specific details relating to the experimental setup. Section 3 contains details about calibration of equipment's and devices, while section 4 presents uncertainty analysis. Section 5 is devoted to the obtained results and relevant discussion. Section 6 presents determination of form factor value for the KCS in different case. Finally, the conclusion is given in Section 7 of this chapter.

3.2 Experimental setup

3.2.1. Towing Tank

The present experiments were conducted at the Kelvin Hydrodynamics Lab at the University of Strathclyde. The towing tank is 76m long and 4.6m wide (see Figure 10). The water depth at the tank was set at 0.32 m for shallow water tests and 2.3m for deep water tests.

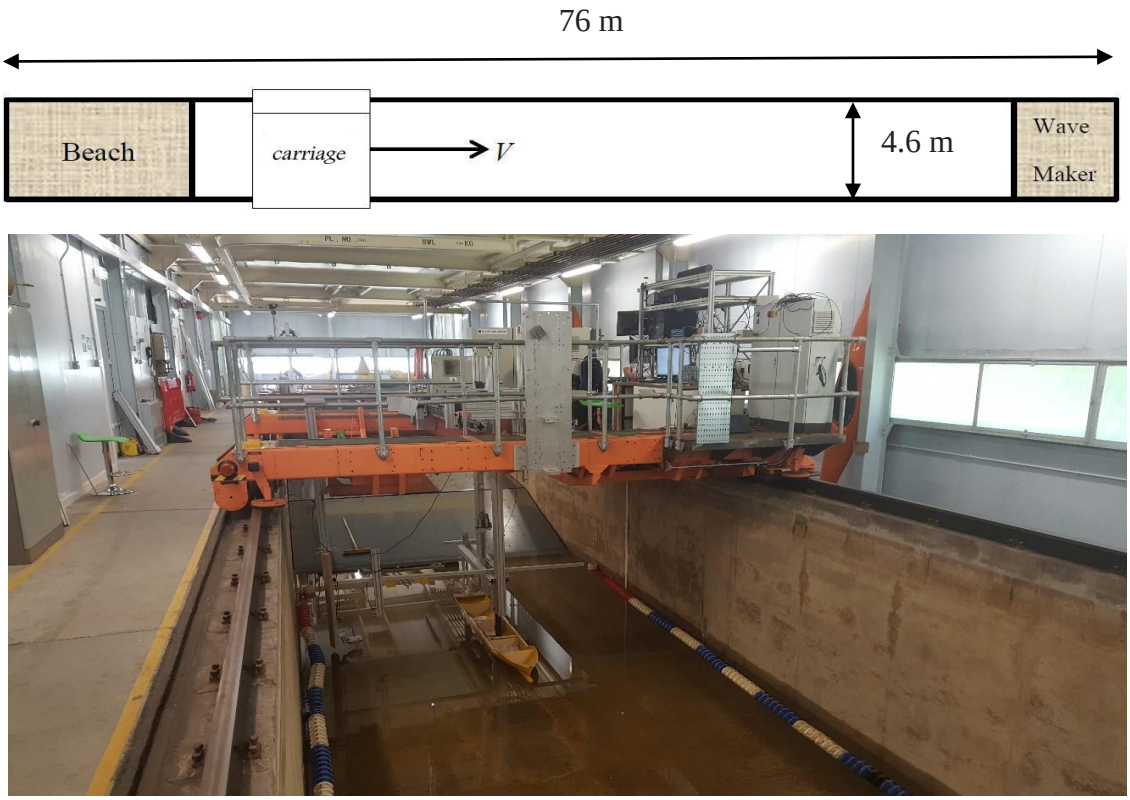

Figure 10 The Kelvin Hydrodynamics Lab

The tank was prepared for four test conditions as follows:

Case I: The tank cross section is rectangular (4.6 m wide and 0.32 m water depth). This is to simulate water depth effects only on ships sailing characteristics. Channel bank effects are excluded. (Refer to Figure 11a).

Case II: Channel banks are introduced through side planks. This configuration is intended to test the effects of both water depth and width (blockage effects) (refer to Table 2). This case also aims to simulate the cross sectional area of the New Suez Canal. It was prepared at a scale of 1:75 with respect to its full scale dimensions (Refer to Figure 11b and c).

Case III: same as case II but with reduced water surface width and bottom width. This case was designed for studying higher blockage ratios. (Refer to Figure 11d and table 2)

Case IV: The tank is filled with water to 2.3 m deep with 4.6 m water surface width. These configurations are intended to test deep water motion characteristics. (Refer to Figure 11e).

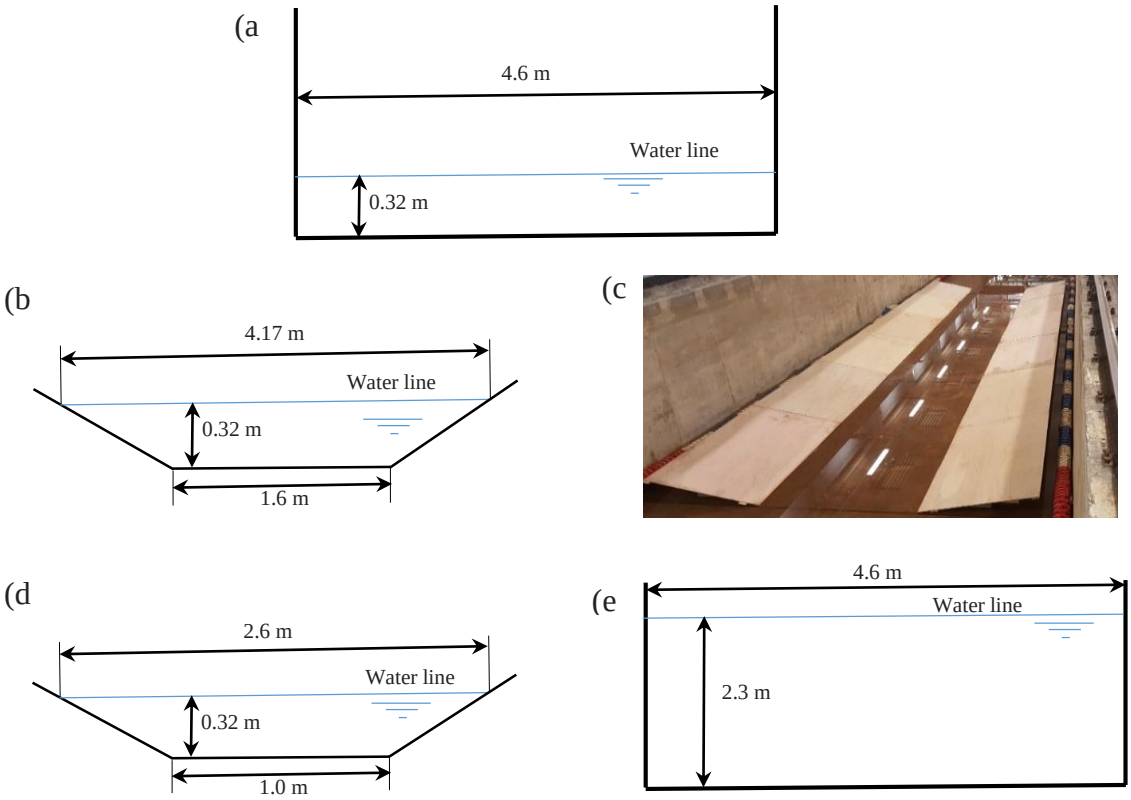

Figure 11 Depictions of the four cases with schematic drawing; a: case I, b & c: case II, d: case III. E: case IV

Table 2 Blockage effect for all cases at T =0.144 ($\overline{W}$ is the mean tank width)

		Model		Tank		Cross sectional area		Blockage ratio (K)
H/T	Case	B (m)	T (m)	$\overline{W}$ (m)	H (m)	A_m (m^2)	A_{tank} (m^2)	$(B*T)/(\overline{W}*H)$
2.2	I	0.429	0.144	4.6	0.32	0.062	1.472	0.042
2.2	II	0.429	0.144	2.88	0.32	0.062	0.8448	0.067
2.2	III	0.429	0.144	1.8	0.32	0.062	0.576	0.10725
15.97	IV	0.429	0.144	4.6	2.3	0.062	10.58	0.0058

3.2.2. Model and Experimental Test Setup

A KCS model was used to study squat characteristics test, as mentioned earlier (see Figure 12). The full scale and model scale ship particulars are given in

Table 3. The model tests were carried out at a range of ship speeds (seeTable 4) and ship drafts.

Two Linear Variable Differential Transformers (LVDTs) were employed to measure trim and sinkage. The sinkage LVDT1 was attached at the mid ship point to measure the heave motion in dynamic mode and the trim LVDT2 was attached at the model forepeak, using the configuration as illustrated in Figure 13. The trim angle was then calculated according to Equation (2).

$$Trim = tan^{-1}\left(\frac{L_2 - L_1}{d}\right) \quad (2)$$

where L_1 and L_2 are the $LVDT_1$ and $LVDT_2$ vertical displacement, respectively.

A load cell was used to measure the water resistance force. This load cell was attached at the mid ship point. The model was restricted to move only in the vertical plane (heave and pitch motion) while being restricted in all other directions. One of the main features of the model test in the towing tank is the possibility of extrapolating the model results to the full scale, because in this test the Suez Canal cross section and KCS model were constructed with a scale factor of 75. It should be noted that the Reynolds number (Re) for the full scale KCS ship at 7 knots calculated to be $6.68*10^8$ and the Reynolds number for the model scale is $1.07*10^6$. The formulation of Reynolds number given in equation (3).

$$Re = \frac{V*L}{\upsilon} \quad (3)$$

where L is the model or ship length at the water line and υ is the water kinematic viscosity which is equal to 1.2532*10-6 m2/s for seawater and 1.2012*10-6 m2/s for fresh water at 13 C^o which was the temperature of water during the test (26th ITTC Specialist Committee, 2011)

Figure 12KCS Model

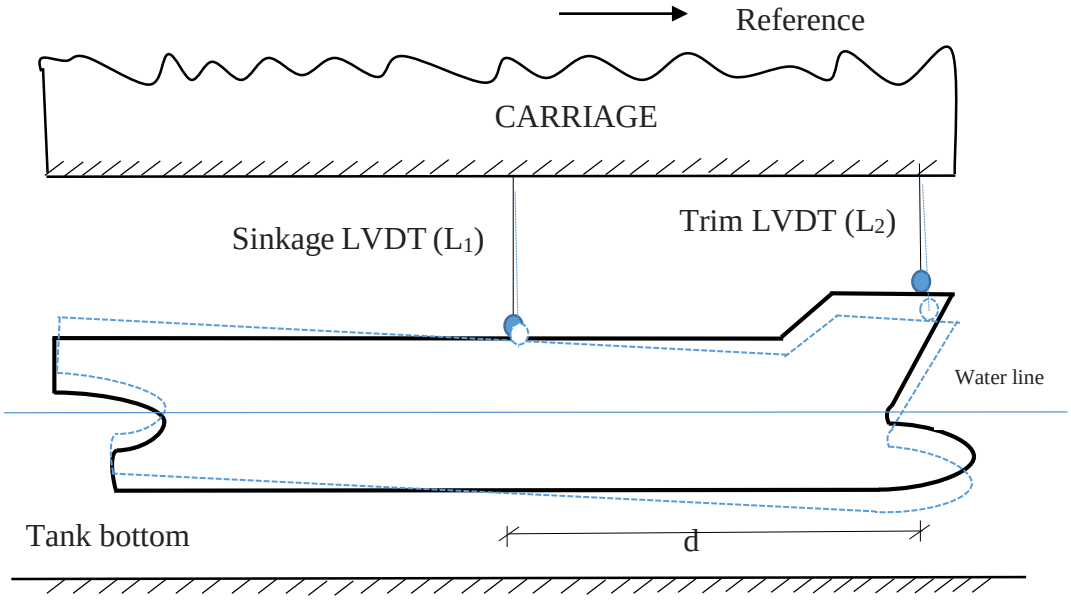

Figure 13 Schematic drawing for trim and sinkage measurements using LVDTs

Table 3 KCS main particulars ("KCS Geometry and Conditions, SIMMAN 2008)

Parameters	**Full scale**	**Model scale with scale factor 1:75**
Length between the perpendiculars (m)	230	3.067
Length at water line (m)	232.5	3.1
Breadth at water line (m)	32.2	0.429
Depth (m)	19	0.25
Draft (m)	10.8	0.144
Displacement (m^3)	52030	0.123
Wetted surface area w/o rudder (m^2)	9530	1.694
Block coefficient	0.651	0.651
Midship section area coefficient	0.985	0.985
Longitudinal centre of buoyancy (%), fwd+	-1.48	-1.48

Table 4 Velocities during the tests

Full-scale speed (knots)	Full-scale speed (m/s)	Froude Number for model scale (Fh=V/√(g*H))	Model-scale speed (m/s)
2	1.01	0.067	0.119
3	1.54	0.1	0.178
4	2.06	0.134	0.238
5	2.57	0.167	0.297
6	3.09	0.2	0.356
7	3.6	0.235	0.416
8	4.12	0.268	0.475
9	4.63	0.302	0.535
10	5.14	0.335	0.594
14	7.2	0.469	0.832
17	8.74	0.57	1.010
20	10.29	0.671	1.188
22	11.32	0.738	1.307
23	11.83	0.771	1.366

3.3 Calibration of Equipment

Before performing any runs, it is of key importance to check the precision and calibration of the measuring devices used for the tests. These are composed mostly of strain transducers and motion sensors.

3.3.1. Calibration for motion measuring instrument

Firstly, calibration of the vertical motion sensor used to measure the amplitudes was performed. This was done with a standard distance rule that the arm of the sensor would measure in a stepwise manner. The measuring arm has to only measure the difference between distances to calibrate itself. The standard rule is made extremely precise and, provided the motion arm is zeroed prior to each test, it can measure distance very precisely. The LVDT for measuring the sinkage and the bow motion were calibrated using a 3D printed block with known distances marked on it. The voltage measured was recorded and the results are shown in Figure 14 and 15. A linear relation was fitted to the result variation. The systematic error is negligible.

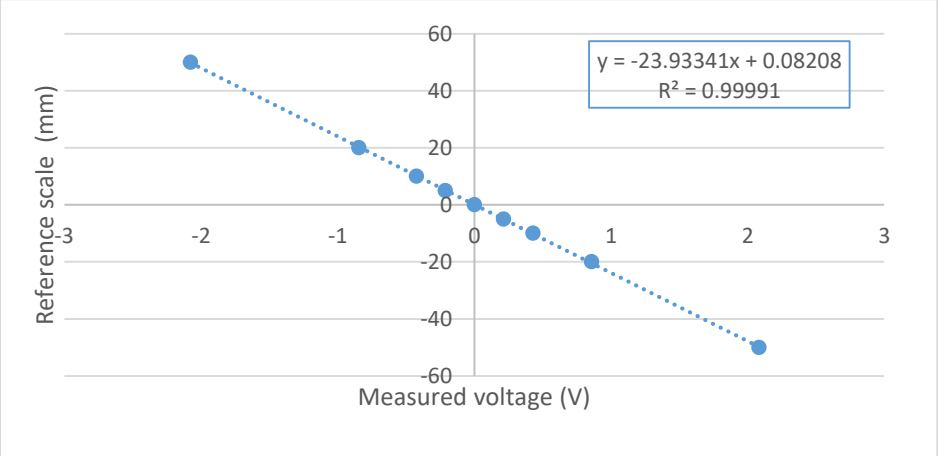

Figure 14 Calibration result of the LVDT sinkage

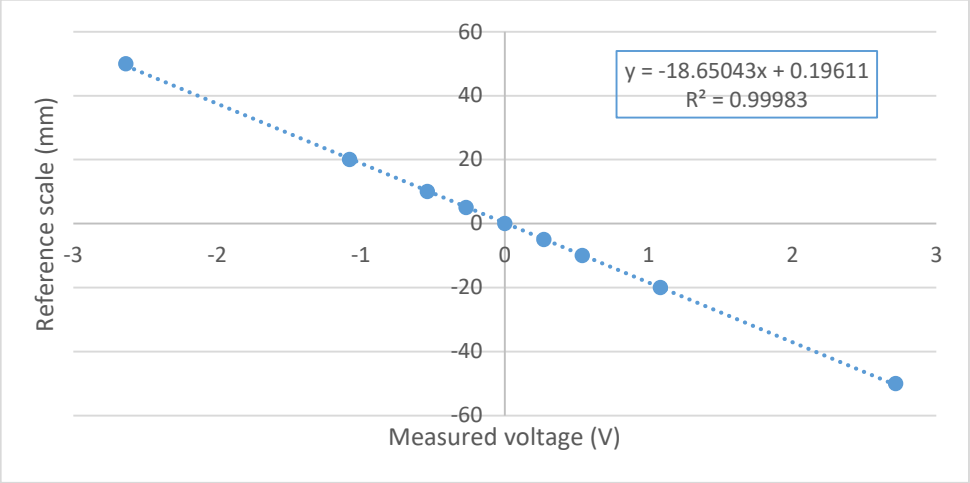

Figure 15 Calibration results of the LVDT bow

3.3.2. Calibration for resistance measuring instrument

For the strain transducers calibration, known weights were hung from the device, measuring the voltage induced so that a correlation and a zero value could be found. The weights were increased gradually to produce a proportionality curve for the voltage induced against weight. This allowed the transducer to easily measure force in Newtons. For the load cell, the calibration process consisted of measuring the voltage produced from the change in resistance due to loaded weights from 0.1 to 10 kg. 10 kg was chosen as the maximum weight as the predicted maximum resistance was approximately 100 N, therefore the load cell was calibrated to work in the region 0 – 100 N. The graph from the load cell calibration is shown in Figure 16. A linear relation between the load and measured voltage was introduced.

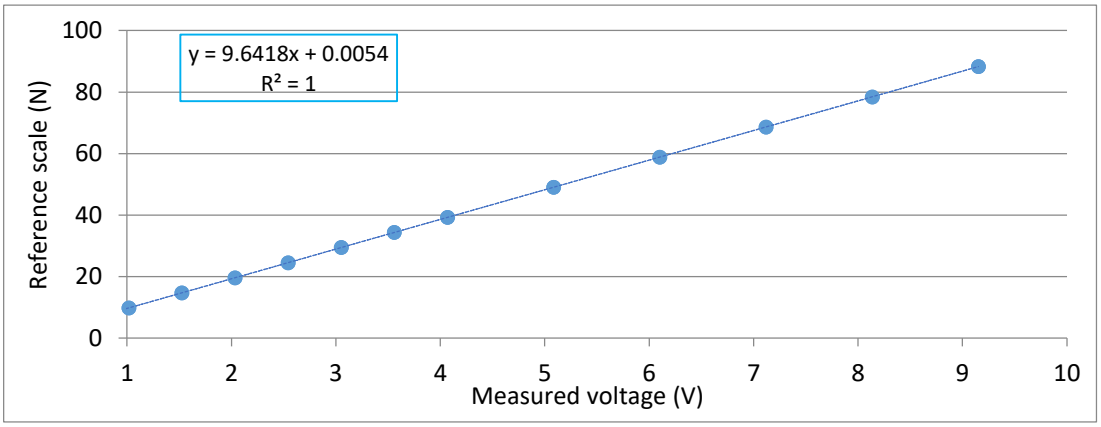

Figure 16 Load cell calibration

3.4 Uncertainty analysis

It is well known that any experiment designed to determine an effect, validate a theoretical model, or estimate the numerical value of a physical variable will be always affected by errors due to instrumentation and calibration devices. Thus, estimation of experimental uncertainty is needed to assess the confidence in the presented results. The uncertainty is divided into two types A and B, based on the way that the uncertainty is evaluated. Type A is precision and type B is bias as introduced in (ITTC, 2014).

3.4.1. Type A Standard uncertainty

This is a method of determining standard uncertainty by evaluation of a statistical analysis of a series of repeated observations. This is also termed 'random uncertainty' (ISO GUM, 2008).

Equation 12 shows how to measure uncertainty using the Type A (u_A) method:

$$u_A = \sqrt{\frac{S^2}{i}} \tag{12}$$

where i is the number of repeat observations and S is the standard deviation of the values (see Equation 13).

Note: the test was repeat for 5 times for two condition, one at high speed V=1.426 and at v= 0.416 at H/T=2.2

$$S = \sqrt{\frac{\sum_{j=1}^{i}(e_j - \overline{e})^2}{i-1}} \tag{13}$$

where e_j is the jth repeated reading and $\overline{e}$ is the mean value of all the repeated readings (see Equation 14).

$$\overline{e} = \frac{\sum_{j=1}^{i} e_j}{i} \tag{14}$$

To obtain a 95% level of confidence uncertainty, the uncertainty Type A (u_A) is multiplied by a coverage factor k as in Equation 15.

$$U_A = ku_A \quad (15)$$

where k = 1.96 for a 95% level of confidence.

3.4.2. Type B Standard uncertainty

This is a method of standard uncertainty obtained by means other than statistical analysis, for example instrument calibration data and linear regression analyses. It is also termed 'systematic uncertainty'.

In the present work, three calibration data sets from the LVDT sinkage, LVDT bow and load cells were used to obtain a standard error of estimate (SEE), then multiplied by 3 to obtain a 95% level of confidence uncertainty as described by (ITTC, 2017a).

A linear relation was then fitted to the calibration data using Equation 16.

$$y = a + bx \quad (16)$$

where *y* is the independent variable in physical units, *x* is the dependent value in volts from a voltmeter, *b* is the slope and *a* is the intercept. The result of calibration of the two LVDTs and load cells used in the test are presented in Figures 13, 14 and 15.
To obtain a better representation of the statistical character of the data, a residual plot was generated (Equation 17).

$$Resid = y_i - (a + bx_i) \quad (17)$$

The linear regression prediction limit is simply the standard error of the estimate (SEE) (Equation 18).

$$SEE = \sqrt{\frac{SS_R}{(N-2)}} \quad (18)$$

where SS_R is the sum of the square of the residuals (see Equation 19) and *N* is the number of calibration points.

$$SSR = \sum_{i=1}^{N} (y_i - a - bx_i)^2 \quad (19)$$

To calculate Type B with a 95% level of confidence, Equation 20 was used.

$$U_B = SEE * 3 \quad (20)$$

Finally, an evaluation of the standard uncertainty, U, was made using Equation 21.

$$U = \sqrt{U_A^2 + U_B^2} \quad (21)$$

3.4.3. Combined standard uncertainty

The combined standard uncertainty, U_C (y), is the "standard uncertainty of the result of a measurement when that result is obtained from the values of a number of other quantities, equal to the positive square root of a sum of terms, the terms being the variances or covariances of these other quantities, weighted according to how the measurement result varies with changes in these quantities" (ISO GUM, 2008). The combined standard uncertainty is evaluated by the propagation of uncertainty and is given by

$$U_C^2(y) = \sum_i^N \left(\frac{\partial f}{\partial x_i}\right)^2 u^2(x_i) + 2\sum_{i=1}^{N-1}\sum_{j=i+1}^{N}\left(\frac{\partial f}{\partial x_i}\right)\left(\frac{\partial f}{\partial x_j}\right) u\,(x_i, x_j) \quad (22)$$

In some situations, the measurement is not measured directly, but is determined from a number N of other quantities $X_1, X_2, .., X_N$ through a function f as:

$$Y = f(X_1, X_2, \dots, X_N) \quad (23)$$

Where Y is the experimental result determined from N other quantities of the function. The quantity $\frac{\partial f}{\partial x_i}$ and $\frac{\partial f}{\partial x_j}$ is the partial derivative of *f* with respect to x_i and x_j and is called the sensitivity coefficient c_i and c_j respectively.

The combined uncertainty equation can be rewritten as:

$$U_C^2(y) = \sum_i^N c_i^2 u^2(x_i) + 2\sum_{i=1}^{N-1}\sum_{j=i+1}^{N} c_i c_j\ u\,(x_i, x_j) \quad (24)$$

3.4.4. Trim uncertainty

In the present experiment the trim was measured and combined between two standard uncertainties which came from LVDT sinkage and LVDT bow.

$$U_{trim}^2 = \left(\frac{\partial Trim}{\partial LVDTbow}\right)^2 * U_{Sbow}^2 + \left(\frac{\partial Trim}{\partial LVDTsinkage}\right)^2 * U_{Ssinkage}^2 \quad (25)$$

$$Trim = tan^{-1}\left(\frac{L_2 - L_1}{d}\right) \quad (26)$$

where *d* is the distance between the two LVDT's (=1666 mm).

3.4.5. Uncertainty results

In this chapter the uncertainty is calculated twice, once at high speed of V= 1.426 m/s and again at a low speed of V= 0.416 m/s.

At high speeds, the uncertainty of sinkage, trim and total resistance has been found to give reasonable values (3.47%, 4.64% and 0.79%) respectively. At low speeds, although the uncertainty of resistance gave a relative large value (2.20 %), the uncertainty for both sinkage and trim were calculated to be more than 90% also, high uncertainty results is reported in (Degiuli et al., 2007) the measuring of uncertainty at very low speed is large. This can be justified because at low speeds, the squat is always recorded in the range of 1 or 2 mm. Since Type A uncertainty is the dominant value in the total uncertainty, and is independent of the ship speed, the percentage uncertainty during low speeds will be high when compared to the uncertainty during high speed. This happens due to the LVDT resolution, where the minimum measurable sinkage is quite similar to the ship sinkage during the low speed.

3.5 Experimental results

Squat and total resistance coefficients for the KCS in a full tank width with restricted depth (Case I)

Figure 17 shows model sinkage ratio (S/Lpp) variations versus depth Froude number for different H/T values. It is clearly noted that, no significant change in the sinkage values occurred over the depth Froude Number range up to 0.33 for all H/T values tested. Past this Fnh range, the sinkage values start to increase with the increase of Fnh and decrease of H/T values.

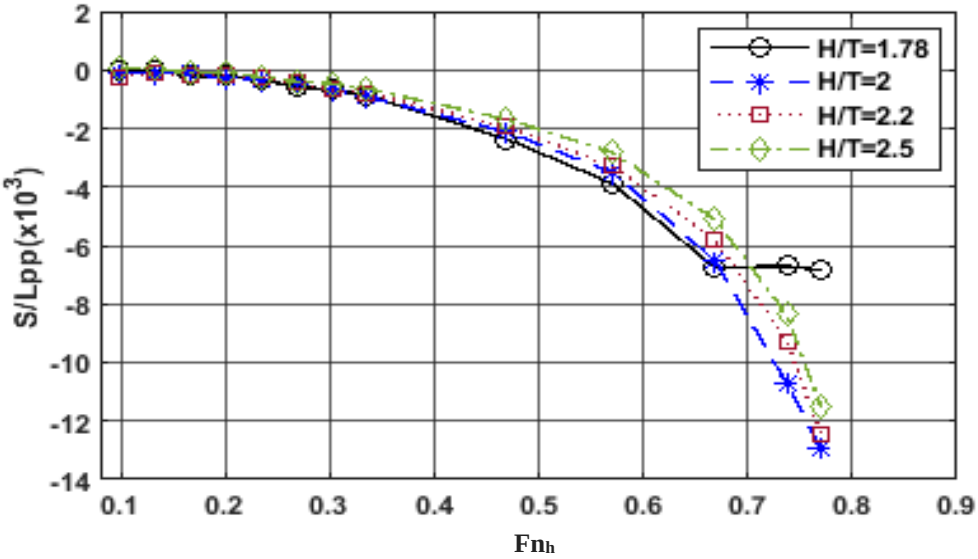

Figure 17 Sinkage per L_{pp} vs depth Froude number for different (H/T)

Figure 18 presents model trim angle variations against depth Froude number for different H/T values. It can be observed that, similar to the sinkage behaviour described above, trim experiences no significant change up to Froude Number value of 0.4 for all H/T values tested. At Froude Numbers greater than 0.45, the ship trim angle tends to increase by aft. The speed at which trim by bow peak value occurs is subject to the considered H/T value. As the KCS model speed gets higher, the model assumes extreme aft trim angles (Refer to Figure 19).

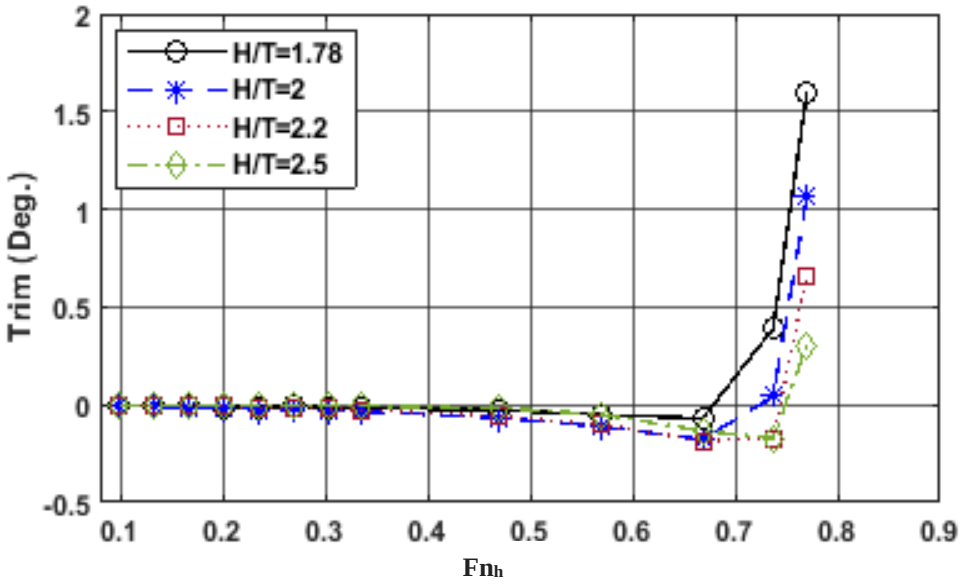

Figure 18 Trim degree vs Froude number for different (H/T)

It is noteworthy that at high speed Fn_h > 0.7 the trim by aft assumes extreme values. As a result, at high ship speed the velocity of return flow around the ship section cannot increase further and a pressure waves will be induced in front of the ship model due to accumulates of water in front of ship model (Lataire et al., 2012) (refer to Figure 19). Furthermore, as Bernoulli principle, the velocity at ship model stern will decrease and the pressure will increase (refer to Figure 19). Albeit, the pressure force acting on the bow will be stronger than on the stern. This therefore explains the reason behind getting high aft trim at that low under keel value.

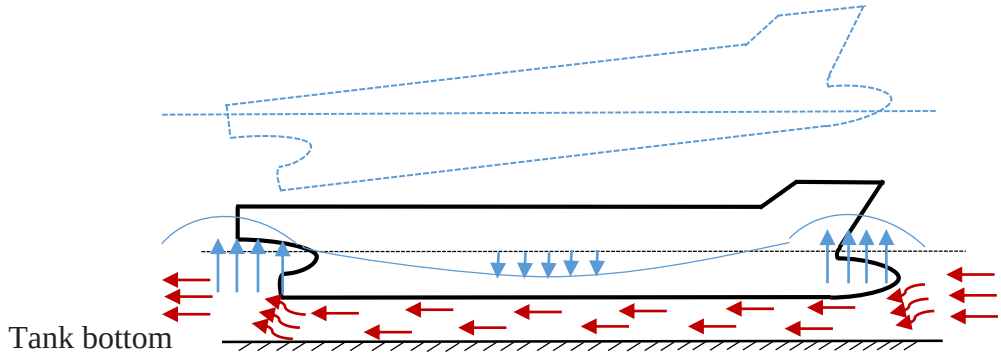

Figure 19 Schematic drawing for the KCS model at high depth Froude number

On other hand, the force acting on the ship model stern at subcritical speeds still not strong enough to create net force at the bow to decrease the sinkage of the model. However, once the blockage effect becomes critical the speed under the keel will became higher and will induce induced high pressure change at stern which leads to high force effect on the ship model stern. Accordingly, the net force acting on the ship model will increase and the sinkage will start to decrease, or remains constant when the blockage ratio exceeds critical value.

To calculate the critical blockage ratio, using Equation 27 (Lataire et al., 2012).

$$K_{crit} = 1 - \sin\left(3arcsin\left(\frac{Fn_h^{2/3}}{2}\right)\right) \quad (27)$$

At Fn_h= 0.74 the critical blockage ratio K_{crit} is 0.0466 and the actual blockage ratio (K) for the KCS model at H/T=1.78 is 0.052 which means that the model has exceeded the critical blockage ratio. Observations on Figure 20 may also help to explain the model behaviour at that speed and blockage ratio.

(a)

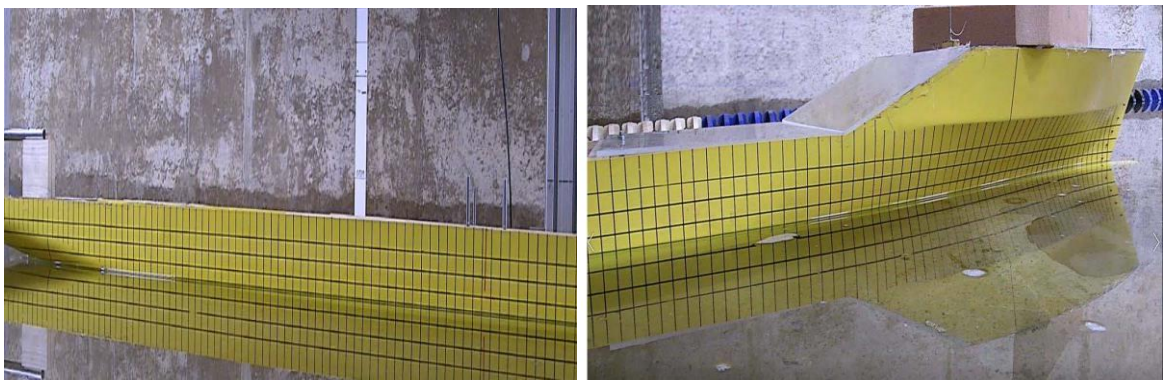

(b)

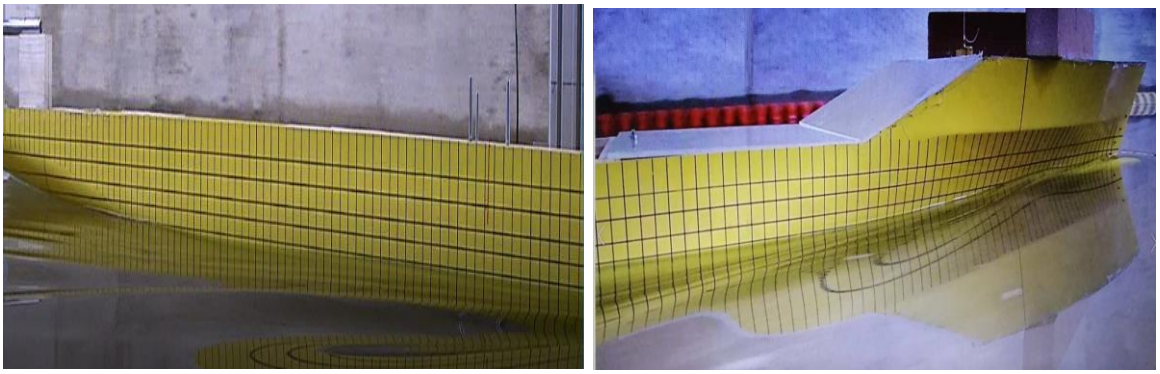

(c)

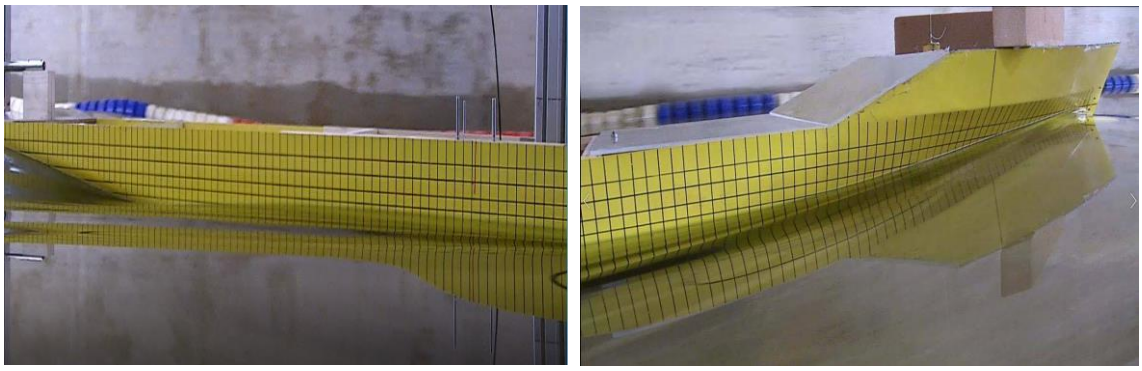

Figure 20 The KCS model during the experiments at different depth Froude number; a: KCS model with Fn_h=0 and K_{CRIT}=1, b: KCS model with Fn_h=0.667 and K_{CRIT}=0.077 and c: KCS model with Fn_h=0.74 and K_{CRIT}=0.046

Figure 21 displays total resistance coefficient variations versus depth Froude number for different H/T values. Very low values with almost negligible change with respect to both speeds and depth to draft ratios were recorded. The total resistance coefficient C_T starts to increase at relatively high rates for Froude Numbers above 0.6 for all H/T values tested. At any depth Froude Number greater than 0.6, the resistance experienced by the model is proportional to the H/T value. In other words, shallow water effects are more pronounced for smaller values of H/T.

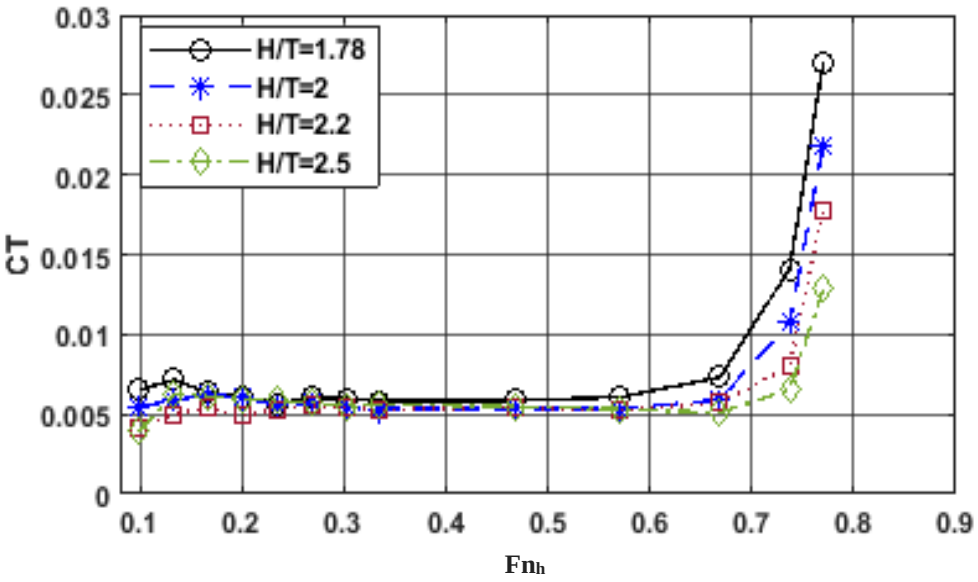

Figure 21 Total resistance coefficient vs Froude number for different (H/T)

Figure 22a and b shows the effect of under keel clearance on sinkage and trim where *H* is water depth and *T* is ship draft at different model depth Froude Numbers. For low speeds corresponding to deep water depth, depth Froude numbers Fn_h=0.235 and Fn_h=0.335 gave almost no sinkage variations. However, with Fn_h = 0.771 the model speed resulted in relatively large sinkage. Trim behaves in a similar way as shown in Figure 22b for a high speed which corresponds to Fn_h= 0.768. The trim degree changes from stern to bow trim as the under keel clearance (H-T)/T decreases.

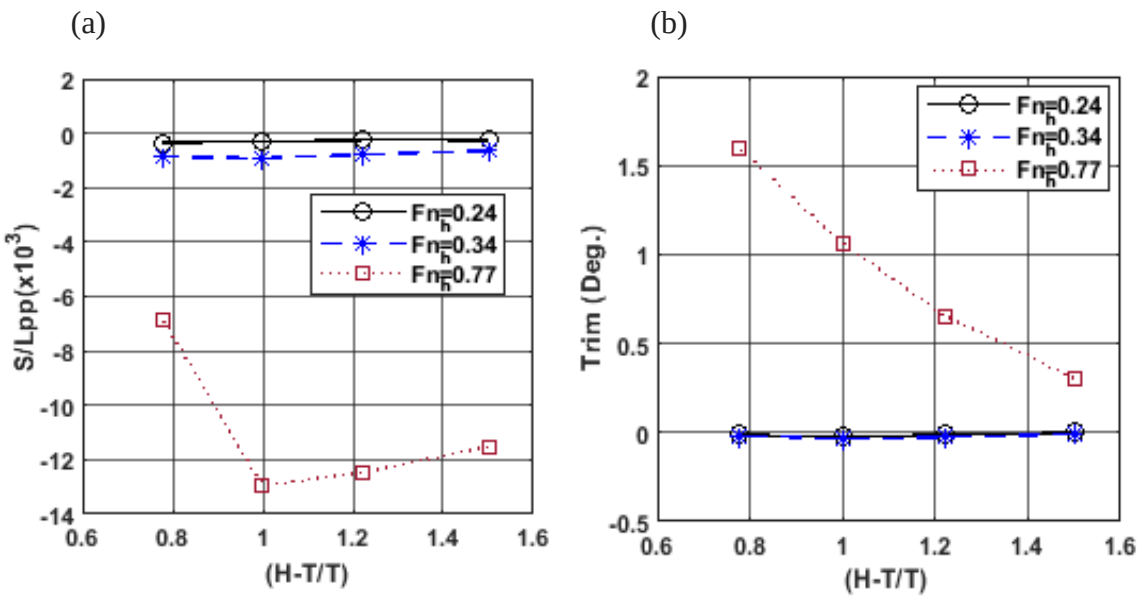

Figure 22 Effect of under keel clearance on sinkage (a) and trim (b) for different depth Froude number

3.5.1. **Comparing the squat and total resistance coefficient between Case I and Case II at different (H/T)**

Figure 23a and b show that the more pronounced sinkage and total resistance coefficient are exhibited for Case II where the combined effect of restricted depth and width are manifested for the range of depth Froude numbers tested. Figure 24a and b (at H/T = 2.2) exhibit the same trend. This can be explained because as the ship sails through the canal, the blockage effect appears, which is the effect of boundaries on the flow around a ship. This means that the flow speeds increase in the canal are higher than those before the ship entered the canal. According to Conn, et all (1953), the blockage correction, which is the correction of restricted flow caused by boundaries, is unnecessary if Equation 28 is satisfied:

$$B_{model} < \frac{B_{tank}}{10} \rightarrow \frac{B_{tank}}{15} \text{ or } T_{model} < \frac{h_{tank}}{10} \rightarrow \frac{h_{tank}}{20} \quad (28)$$

For this case $B_{model} = 0.429m$ and B_{tank} at highest point $= 4.17m$ so $B_{model} > \frac{B_{tank}}{10}$. The same applied for $T_{model} > \frac{h_{tank}}{10}$ so the blockage correction was necessary for this case. To prove the effect of boundaries on the flow in the case I used Conn's method:

$$\left(\frac{V_1}{V}\right)^3 \frac{{F_n}^2}{2} - \left(1 - \frac{a}{bh} + \frac{{F_n}^2}{2}\right)\frac{V_1}{V} + 1 = 0 \quad (29)$$

where *v* is the carriage speed, V_1 is the flow speed after the ship enters the Canal, *a* is the mean cross sectional area of the submerged model, *b* is the tank breadth and *h* is the tank depth.

The flow speed was calculated after entering the Canal at Fn_h = 0.57, b at highest point = 4.16m and h =0.32m.

$$\left(\frac{V_1}{1.01}\right)^3 \frac{0.57^2}{2} - \left(1 - \frac{0.0412}{4.16*0.32} + \frac{0.57^2}{2}\right)\frac{V_1}{1.01} + 1 = 0 \quad (30)$$

$$0.157672V_1^3 - 1.12036V_1 + 1 = 0 \quad (31)$$

Solving this equation using Matlab based on the above conditions, a flow velocity V_1= 1.06 m/s results. If $\overline{B}$ = 2.88 m is used, which is the mean tank width in the case II, V_1 increases to 1.1m/s. The underlying reason is the rise in flow velocity after the ship enters the canal. In consequence, the drag force increases since the drag resistance is a function of flow speed (refer to Equation 32 where ρ is water density, C_D is drag coefficient and *S* is wetted surface area). Drag resistance is one of many factors with an effect on the total resistance of a ship. This explains why the total resistance coefficient increases when the ship enters the Canal

$$F_d = 0.5\,\rho C_D S V^2 \quad (32)$$

The C_T curves (Figures 23b and 24b) represent the total resistance coefficient variation against ship speed (or Froude's number). The ship total resistance is composed of frictional resistance (or viscous resistance in 3D approach) and residuary resistance component (or the wave making resistance component C_w in the 3D approach). The last component; C_w is characterized by humps and hollows due to interference of different wave systems generated by different parts of the ship particularly the bow and stern.

(a)

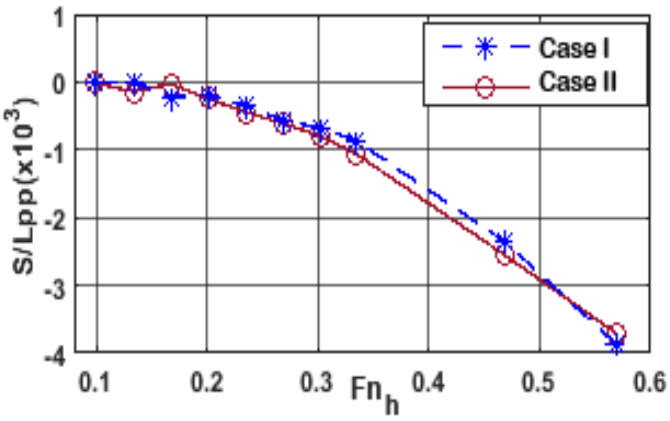

(b)

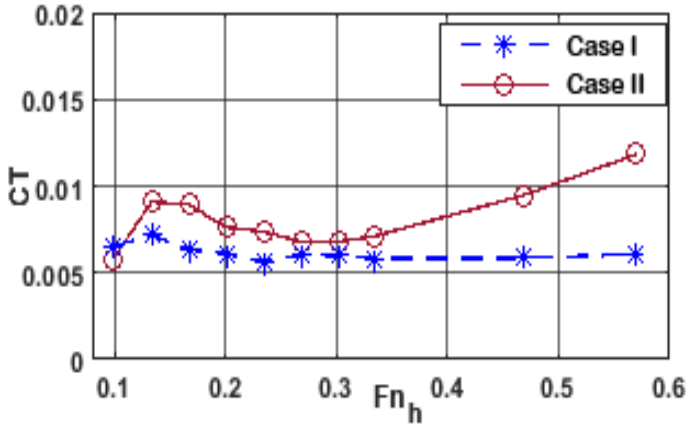

Figure 23 Effect of Canal on (a) sinkage and (b) total resistance coefficient for H/T = 1.78

(a)

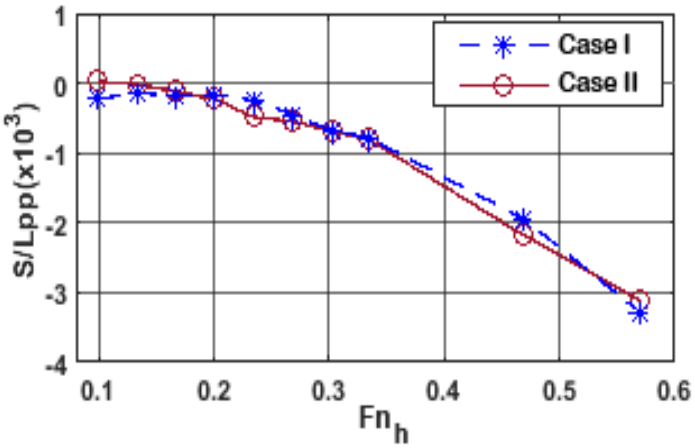

(b)

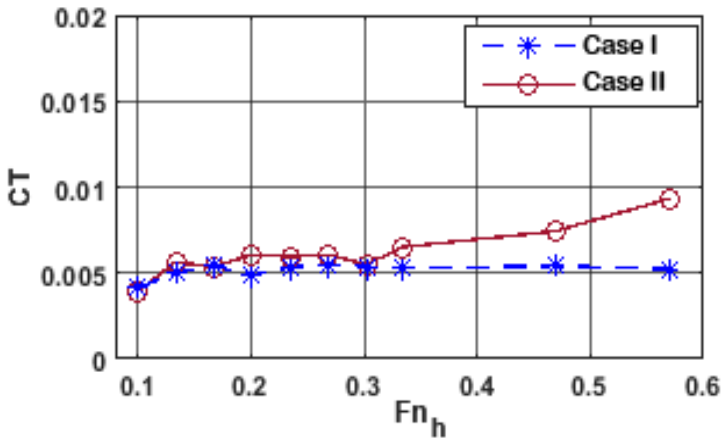

Figure 24 Effect of Canal on (a) sinkage and (b) total resistance coefficient for H/T= 2.2

3.5.2. Comparing the squat and total resistance coefficient between Case II and Case III at different (H/T)

The measured squat and total resistance coefficient while moving in realistic canal is plotted versus Froude Number in Figure 25, 26 and 27 for three values of H/T ratio for two conditions. The first condition is with the actual cross sectional area of the Suez Canal and the second condition is after reducing the width of the Canal to 62.5% of its real-life cross sectional area. For the three H/T values it is clearly seen that higher values for the sinkage, trim and total resistance coefficient are recorded for case III due to the effect of higher blockage ratio.

It can also be noticed that at low value of H/T =1.78 and high depth Froude number value the sinkage is increased by 25.9% more than at H/T value 2.2 in case II and III. Meanwhile, for the total resistance coefficient value at H/T=1.78 and depth Froude number 0.57 increased by 30% for case II than at H/T= 2.2 and increased by 33.4% for case II than at H/T= 2.2. The total resistance coefficient increased because at low values of H/T the blocgae effect became more restricted and the flow velocity around the ship hull will rise. As is well known the drag resistance is a function of the flow.

On the other hand, the trim in case III at H/T = 1.78 and depth Froude number = 0.57 increased by 83% and as explained in section 3.5.1, at high speed Fn_h > 0.4 for case III

the trim by aft assumes extreme values. As a result, at high ship speed the velocity of return flow around the ship section cannot increase further and pressure waves will be induced in front of the ship model due to accumulated water in front of ship model. Also the velocity at ship model stern will decrease and the pressure will increase (albeit, the pressure force acting on the bow will be stronger than on the stern. This therefore explains the reason behind getting high aft trim at that low under keel value. The above occurs when the critical depth Froude number is reached or exceeded.

(a)

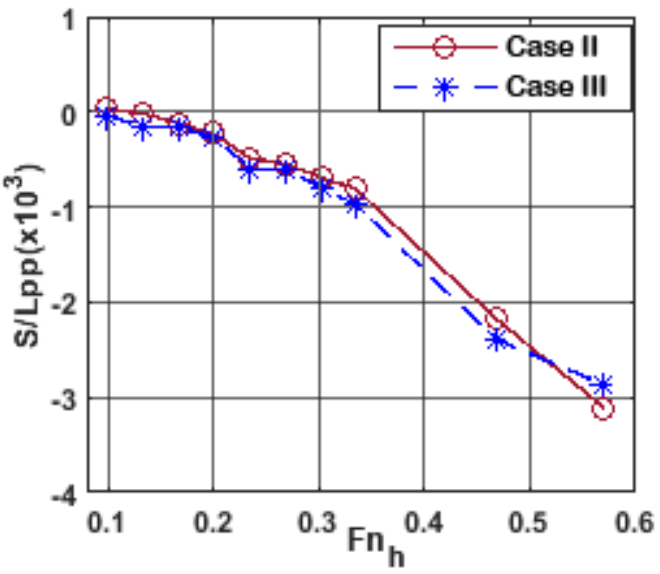

(b)

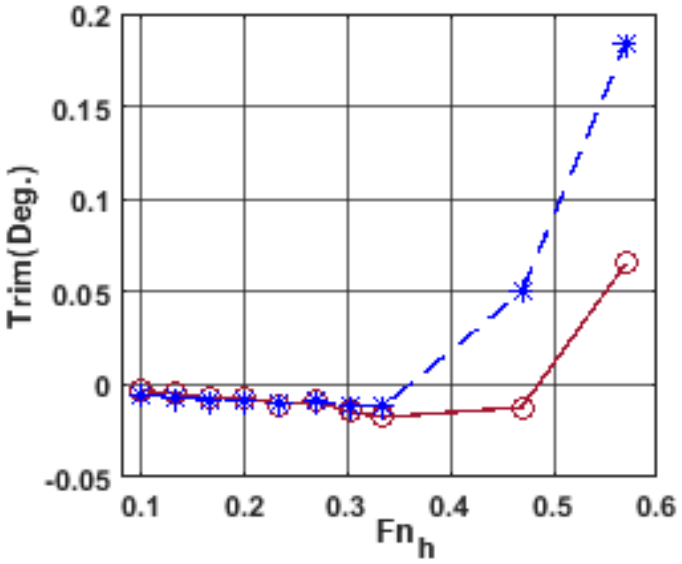

(c)

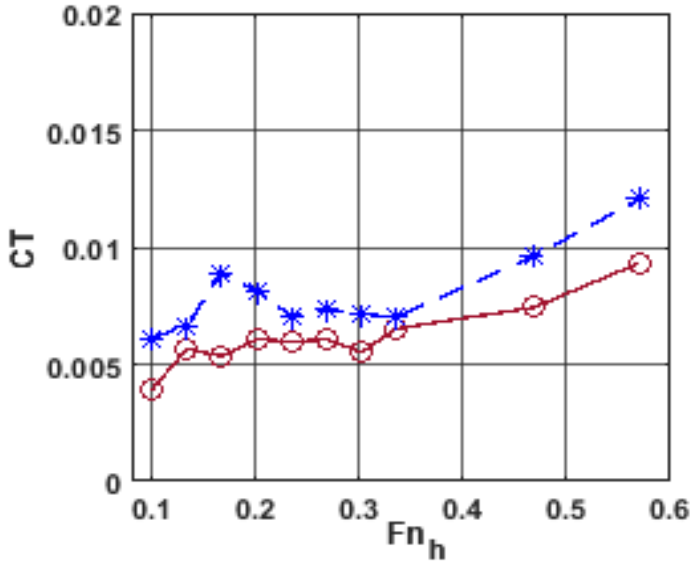

Figure 25 Side wall effects on (a) sinkage, (b) trim and (c) total resistance coefficient for H/T=2.2

(a)

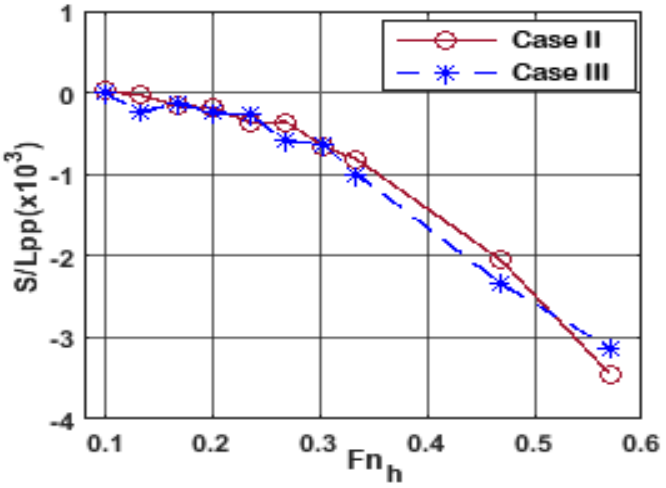

(b)

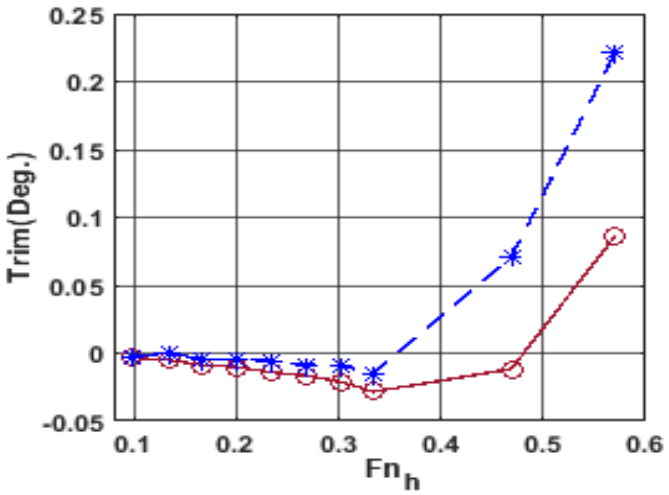

(c)

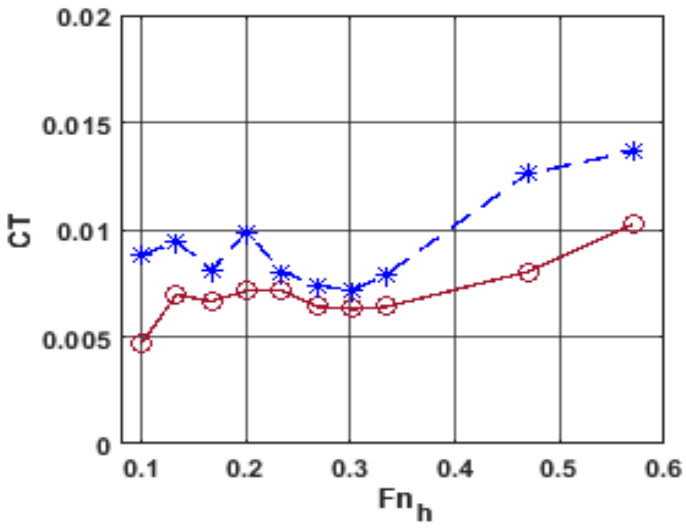

Figure 26 Side wall effects on (a) sinkage, (b) trim and (c) total resistance coefficient for H/T=2

(a)

(b)

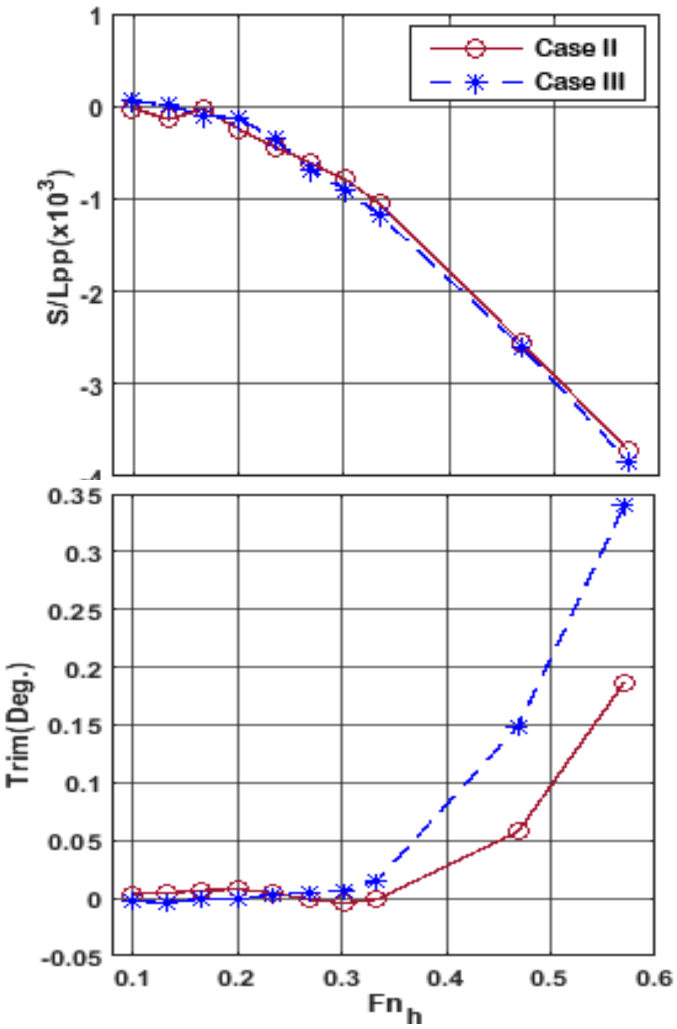

(c)

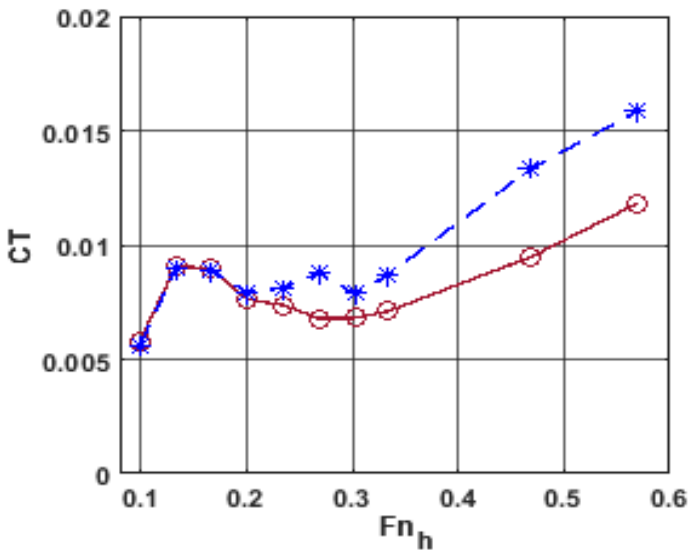

Figure 27 Side wall effects on (a) Sinkage, (b) Trim and (c) Total Resistance Coeff. for H/T=1.78

3.5.3. Comparing the squat and drag coefficient between Case I and Case IV at ship draft 0.144m.

Figure 28 illustrates model sinkage variations against depth Froude number for model at draft 0.144 m for Case I and Case IV. Case IV represents mostly deep water behaviour, whereas case I covers more range of shallow water characteristics manifested in much higher values for squat due to operating at high depth Froude numbers.

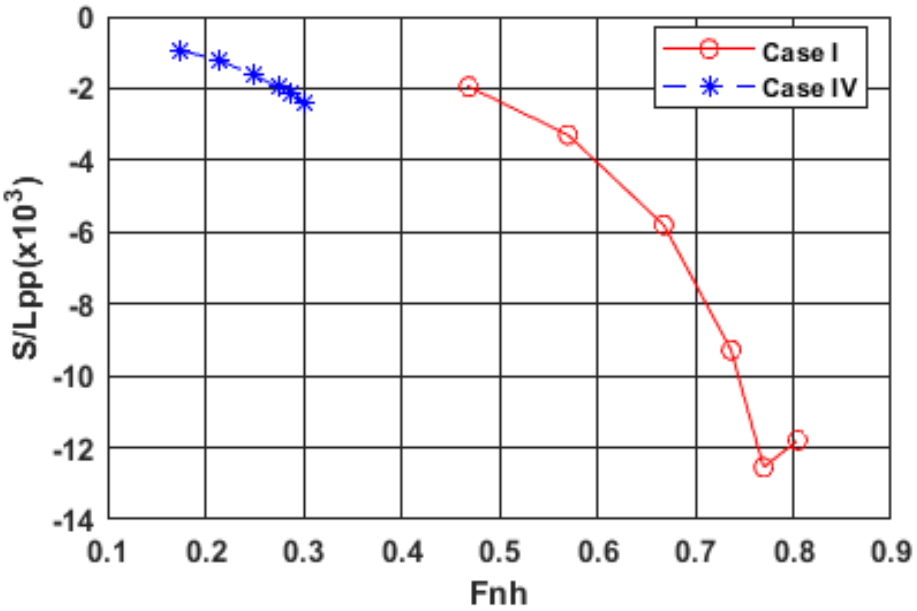

Figure 28 Model experimental results for sinkage per L_{pp} vs depth Froude number for draft 0.144 m

Figure 29 illustrates model trim variations against depth Froude number for model draft 0.144 m for Case I and Case IV. Negligible trim values for deep water operating (case IV) whereas higher trim values are obtained near critical depth Froude number (case I).

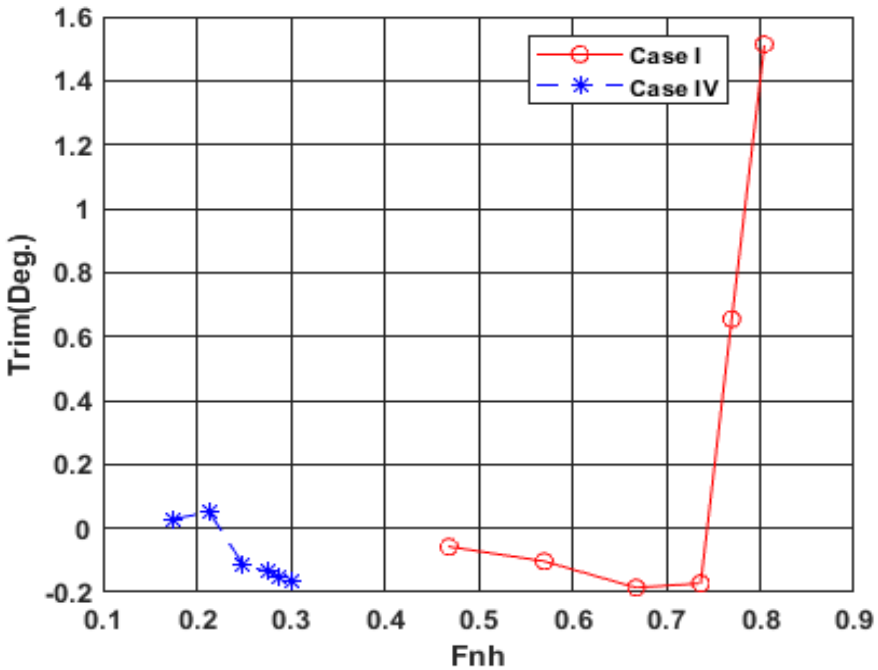

Figure 29 Experimental model trim (degree) vs depth Froude number for draft 0.144 m

Figure 30 shows the total resistance coefficient C_T variations against depth Froude number for model draft 0.144 m for case I and case IV. Again Case IV results indicated deep water characteristics as no significant variation in total resistance coefficient (C_T) values up to 0.3 Fn_h. On the otherhand case I provides useful data for total resistance coefficient (C_T) values particularly when approaching critical Fn_h values.

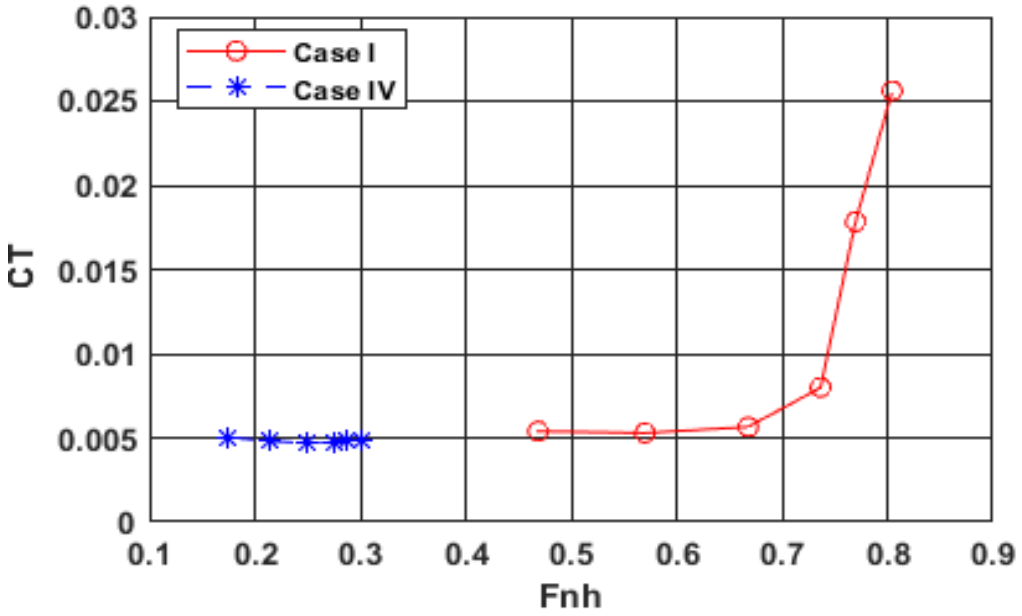

Figure 30 Total resistance coefficient vs depth Froude number for draft = 0.144m

3.6 Form Factor

The form factor (1 + k) is the ratio between the viscous resistance of the hull and the frictional resistance of a flat plate with the same length and wetted surface area. The form factor is assumed to be the same for model scale as for full scale. In experiments, this factor is determined for each individual hull form from low speed resistance measurements where the wave resistance components are supposed to vanish according to a certain rule:$(1 + k) = \lim_{F_n \to 0} \frac{R}{R_F}$, R_F where is flat plate resistance.

The measured model resistance data was used to determine a form factor value for the KCS. Following the (ITTC, 2002) the wave making resistance coefficient C_W is a function

of total resistance coefficient (C_T), friction resistance coefficient (C_F) and form factor (1+k), as in Equation 33.

$$C_W = C_T - (1 + k)C_F \tag{33}$$

The total resistance coefficient (C_T), friction coefficient (C_F) and wave making resistance coefficient (C_W) are calculated according to the following:

$$C_T \equiv R_T/(0.5 * \rho * S * V^2) \tag{34}$$

$$C_F \equiv R_F/(0.5 * \rho * S * V^2) \tag{35}$$

$$C_W \equiv R_W/(0.5 * \rho * S * V^2) \tag{36}$$

where R_T is the model total resistance, R_F is the friction resistance, R_w is the wave making resistance, ρ is the water density, S is the wetted surface and V is model ship speed.

The ITTC 57 friction correlation line equation is used to calculate C_F as following:

$$C_F = 0.075/(\log Re - 2)^2 \tag{37}$$

An experimental test was carried out for two cases of blockage ratio 0.073 and 0.1073 for Case II and Case III respectively for H/T = 2.2 to determine the form factor (1+k) of the KCS hull at these to conditions. It is assumed that at these low speeds the wave making resistance is a function of Fn^4, where Fn is the Froude number based on ship length.

$$F_n = \frac{V}{\sqrt{g*L}} \tag{38}$$

where g is gravitational acceleration.

From Equation (33) the form factor can be found as:

$$(1 + k) = \lim_{F_n \to 0} \frac{C_T}{C_F} \tag{40}$$

Based on Prohaska's method (PROHASKA, C.W, 1966), a plot of CT/CF versus Fn^4/CF is prepared the value of CT/CF at Fn^4/CF = 0 would represent the form factor (1+k), since the wave making resistance coefficient would equal zero and the total resistance coefficient would represent the viscous resistance coefficient, $CV = CF *$(1+k). Figure 30a and b shows CT/CF, where the y-axis intersection is CV/CF = (1+k).

(a)

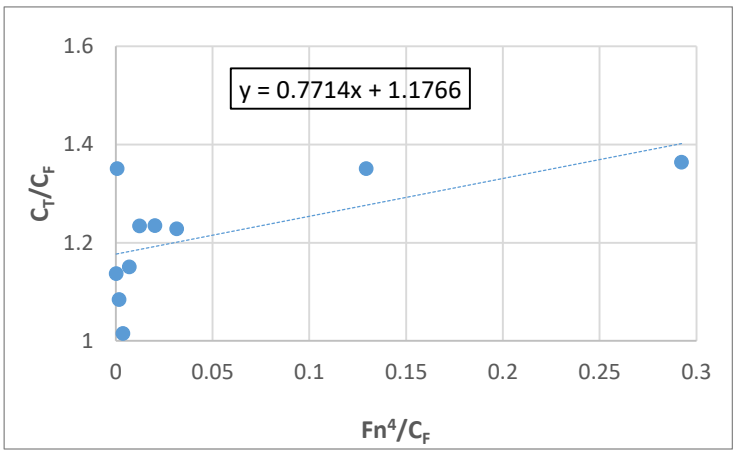

(b)

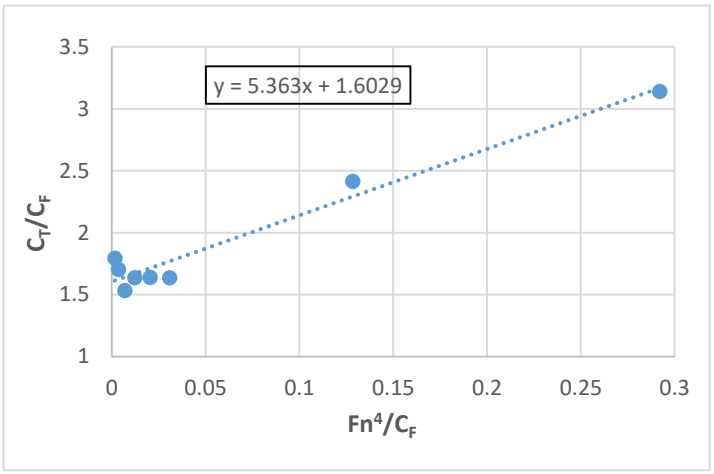

Figure 31 Form factor calculation (a) blockage ratio = 0.042 (Case I) and (b) blockage ratio = 0.1073 (CaseIII) based on Prohaska's method at H/T = 2.2

After fitting a linear trend line through the plot it becomes clear that the resistance tests suggest a form factor (1+k) = 1.1766 for the lower blockage ratio and (1+k) = 1.603 for the higher blockage ratio.

Figure 32 shows the side wall effect on the wave making resistance coefficient in shallow water. It can be concluded that the side wall effect on wave making resistance are more significant for Fn_h values greater than 0.35. The curves exhibit a typical oscillatory behaviour, which is attributed the interference generated by the wave system.

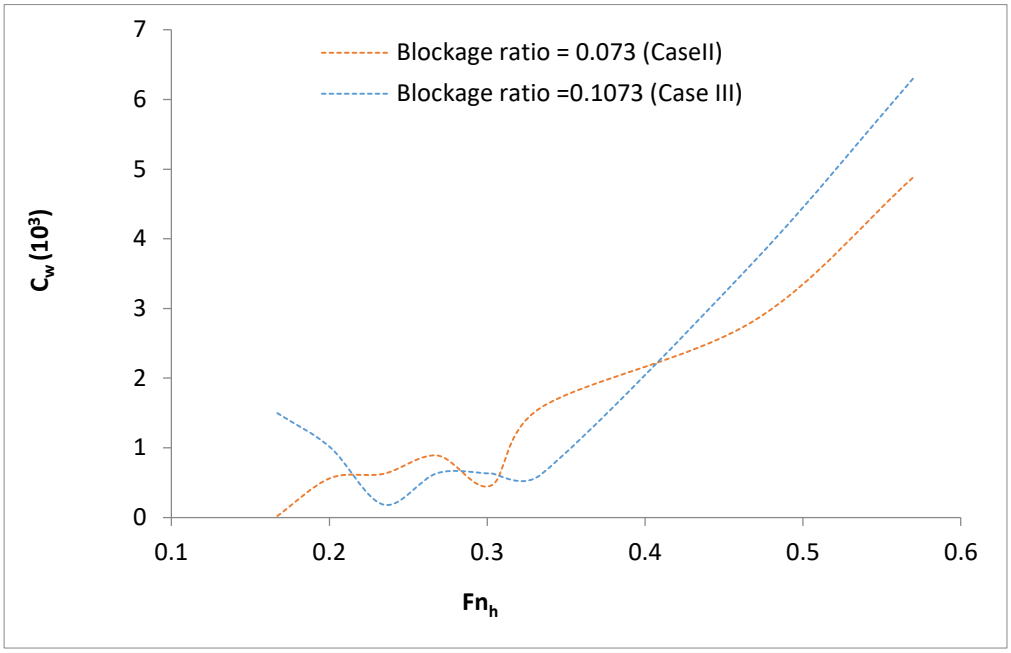

Figure 32 Side wall effects on wave making resistance coefficient at H/T = 2.2

It was found out that higher blockage ratio results in significant squat, trim and added resistance (e.g. 20% increase in wave making resistance for the higher blockage values (0.1073) than the lower are (0.073) at depth Froude number =0.57) see figure 32.

As evident from the current study, the effect of side wall on wave making resistance coefficient in shallow water is greater than in deep water at $Fn_h > 0.35$.

Taking into consideration that a KCS ship model is used in the current study, the calculated values of form factor exhibit a similar trend to (Toxopeus, 2013) in which computational fluid dynamics (CFD) were employed to calculate the viscous flow for KLVCC2 and showed that the form factor varies with condition change from shallow to deep water. It is observed from figure 33 that there exists a clear relation between the form factor (1+k) and water depth-to-ship model draft ratio (H/T). This process is replicated experimentally in this study to calculate the form factor of the KCS ship at a given water depth.

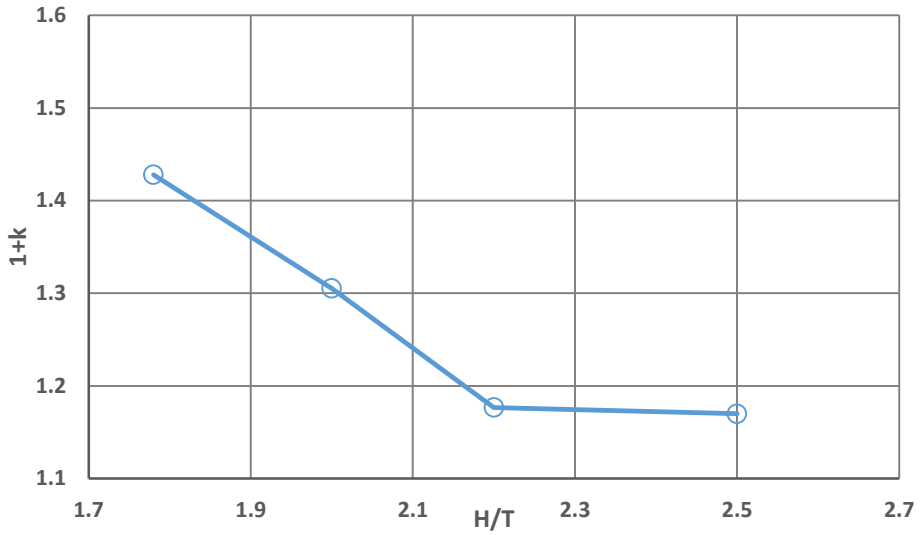

Figure 33 Effect of change of (H/T) on form factor for case I

3.7 Extrapolation of the experimental results.

In model tests, we measure the total resistance, not the separate components. As well known the total resistance is due primarily to two components: friction and waves. But, while the wave resistance is modelled correctly, the frictional resistance is not, which means that the total resistance is not. So, it has to calculate frictional resistance for both the model and ship using empirically based equations. One such approach was established by the International Towing Tank Conference (ITTC-78 method), which is summarized below.

Tow the model at constant speed over a range of speeds from low speeds to speeds exceeding the design, or trial speed. Measure total resistance, and from the test results model total resistance C_{TM} were calculated as equation (3).

$$C_{TM} = \frac{R_{TM}}{0.5\rho V_M^2 S_M} \tag{41}$$

where R_{TM} is the measured total model resistance, ρ is the fresh water density, V_M is the model speed and S_M is the model wetted surface.

Then, Calculate the model frictional resistance coefficient C_{FM} using the ITTC-57 Model-Ship Correlation Line at each speed see equation 42

$$C_{FM} = \frac{0.075}{(log_{10}R_{nM}-2)^2} \quad (42)$$

where R_{nM} model Reynolds number see equation 43

$$R_{nM} = \frac{V_M L_M}{\nu_M} \quad (43)$$

where L_M is the model length and ν_M is the kinematic viscosity which is a function of the fresh water temperature.

As the residuary resistance coefficient C_R is the same at model and full scales. The residuary resistance coefficient at each speed can calculated from equation 44.

$$C_R = C_{TM} - (1+k)C_{FM} \quad (44)$$

To calculate the ship frictional resistance coefficient C_{FS} using the ITTC-57 Model-Ship Correlation Line at each speed, see equation 45.

$$C_{FS} = \frac{0.075}{(log_{10}R_{nS}-2)^2} \quad (45)$$

where R_{nS} ship Reynolds number, see equation 46.

$$R_{nS} = \frac{V_S L_S}{\nu_S} \quad (46)$$

where L is the model length and ν_S is the kinematic viscosity which is a function of the fresh water temperature.

To calculate the total resistance coefficient for a smooth ship, using equation (47).

$$C_{TS} = (1+k)C_{FS} + C_R + \Delta C_F + C_A + C_{AAS} \quad (47)$$

where ΔC_F is the roughness allowance and C_A is correlation allowance see equation (48 and 49). C_{AAS} is the air resistance

$$\Delta C_F * 10^3 = 44\left[\left(\frac{k_S}{L}\right)^{1/3} - 10Re^{-1/3}\right] + 0.125 \quad (48)$$

$$C_A = (5.68 - 0.6\log Re) * 10^{-3} \quad (49)$$

To calculate the total ship resistance & effective power for each speed, see equation 50

$$R_{TS} = 0.5 C_{TS} \rho V_S^2 S_S \quad (50)$$

3.7.1 Full scale results

The results were extrapolated for case I, which simulate a rectangular tank cross section (4.6 m wide and 0.32 m water depth). This is to simulate water depth effects only on ships sailing characteristics. Channel bank effects are excluded. Case II simulated the cross sectional area of the New Suez Canal for different water depth to ship draft ratio (H/T) has been extrapolated.

Figure 34 and table 5 illustrate total resistance variations versus depth Froude number for different H/T values for case I. Very low values with almost negligible change with respect to both speeds and depth to draft ratios were recorded. The total resistance starts to increase at relatively high rates for Froude Numbers above 0.6 for all H/T values tested. At any depth Froude Number greater than 0.6, the resistance experienced by the model is proportional to the H/T value. In other words, shallow water effects are more pronounced for smaller values of H/T.

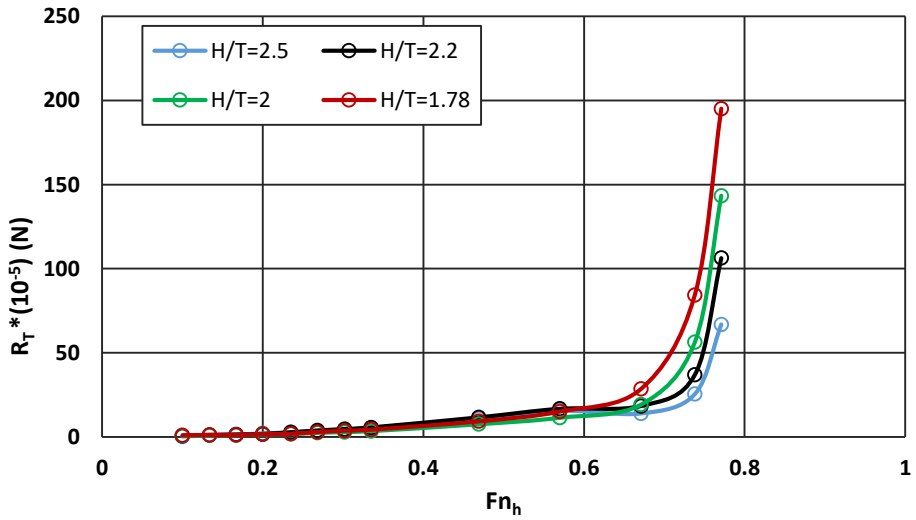

Figure 34 Total resistance vs depth Froude number for various H/T values (case I)

Table 5 Total ship resistance & total ship resistance coefficient for each speed and full scale KCS for case I

H/T=2.5													
Ship speed (knots)	3	4	5	6	7	8	9	10	14	17	20	22	23
(Fn_h)	0.1	0.134	0.167	0.2	0.235	0.268	0.302	0.335	0.469	0.57	0.671	0.738	0.771
(C_T)*10^3	2.09	4.79	4.80	4.71	4.74	4.69	4.55	4.61	4.67	4.57	2.95	4.45	10.73
R_T (N)*10^{-5}	0.22	0.90	1.41	2.00	2.73	3.54	4.33	5.41	10.75	15.51	13.90	25.38	66.78
H/T=2.2													
(C_T)*10^3	4.70	5.62	4.09	3.66	4.20	4.49	4.41	4.31	4.57	4.48	3.56	5.91	15.63
R_T (N)*10^{-5}	0.54	1.16	1.31	1.70	2.64	3.70	4.59	5.53	11.52	16.62	18.29	36.81	106.27
H/T=2													
(C_T)*10^3	5.24	3.82	2.83	2.82	2.53	2.74	2.56	2.48	2.76	2.83	3.44	8.33	19.46
R_T (N)*10^{-5}	0.65	0.85	0.98	1.42	1.72	2.45	2.89	3.46	7.53	11.39	19.18	56.22	143.36
H/T=1.78													
(C_T)*10^3	7.40	4.44	2.78	2.71	2.43	2.94	3.01	2.83	3.12	3.46	4.73	11.57	24.51
R_T (N)*10^{-5}	1.00	1.07	1.04	1.47	1.79	2.84	3.67	4.26	9.21	15.01	28.46	84.32	195.14

Figure 35 and table 5 illustrate total resistance variations versus depth Froude number for different H/T values for case II which simulated the cross sectional area of the New Suez canal. It can be seeb that the more pronounced total resistance is exhibited for Case II where the combined effect of restricted depth and width are manifested for the range of depth Froude numbers tested. It was also of notice that the total resistance for case I exhibits the same trend for case II. Albeit, in case II the total resistance starts to increase at relatively high rates for Froude Numbers above 0.45 for all H/T values tested and at any depth Froude Number greater than 0.45, the resistance experienced by the model is proportional to the H/T value. In other words, shallow water effects are more pronounced for smaller values of H/T. This can be explained because as the ship sails through the canal, the blockage effect appears which is the effect of boundaries on the flow around a

ship. This means that the flow speeds increase in the canal is higher than that before the ship entered the canal.

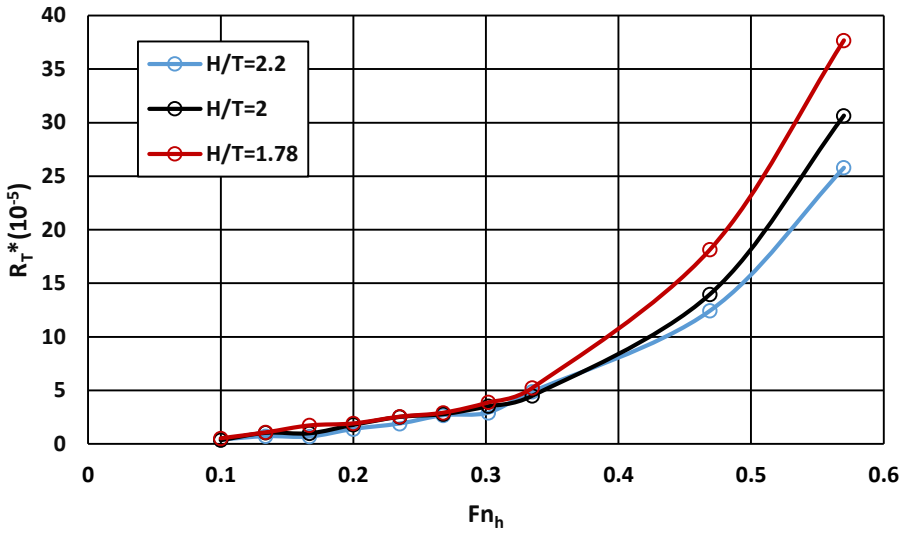

Figure 35 Total resistance vs depth Froude number for various H/T values (case II)

H/T=2.2										
Ship speed (knots)	3	4	5	6	7	8	9	10	14	17
(Fn_h)	0.1	0.134	0.167	0.2	0.235	0.268	0.302	0.335	0.469	0.57
(C_T)*10^3	3.51	3.48	2.13	3.00	3.02	3.25	2.80	3.80	4.94	6.95
R_T (N)*10^{-5}	0.40	0.72	0.68	1.39	1.90	2.68	2.92	4.87	12.44	25.80
H/T=2										
(C_T)*10^3	2.88	4.69	2.89	3.57	3.71	3.13	3.13	3.24	5.12	7.62
R_T (N)*10^{-5}	0.36	1.05	1.01	1.79	2.53	2.79	3.53	4.50	13.98	30.65
H/T=1.78										
(C_T)*10^3	3.92	4.48	4.61	3.52	3.45	3.02	3.18	3.48	6.15	8.67
R_T (N)*10^{-5}	0.53	1.08	1.73	1.91	2.55	2.92	3.88	5.23	18.15	37.68

Table 6 Total ship resistance & total ship resistance coefficient for each speed and full scale KCS for case II

In the extrapolated results the total resistance coefficient equation 49 which takes into consideration the roughness allowance ΔC_F and correlation allowanceC_A. In Figure 36 the effect of roughness allowance and correlation allowance on the total resistance coefficient are shown. It was noticed that at the percentage of the different values of total resistance coefficient when the roughness allowance and correlation allowance were added ranges from 30% to 40% at low value of depth Froude number and ranges from 7% to 9% at high value of depth Froude number. This is means its high recommended when the total resistance results extrapolated take into account the effect of the roughness allowance and correlation allowance coefficients.

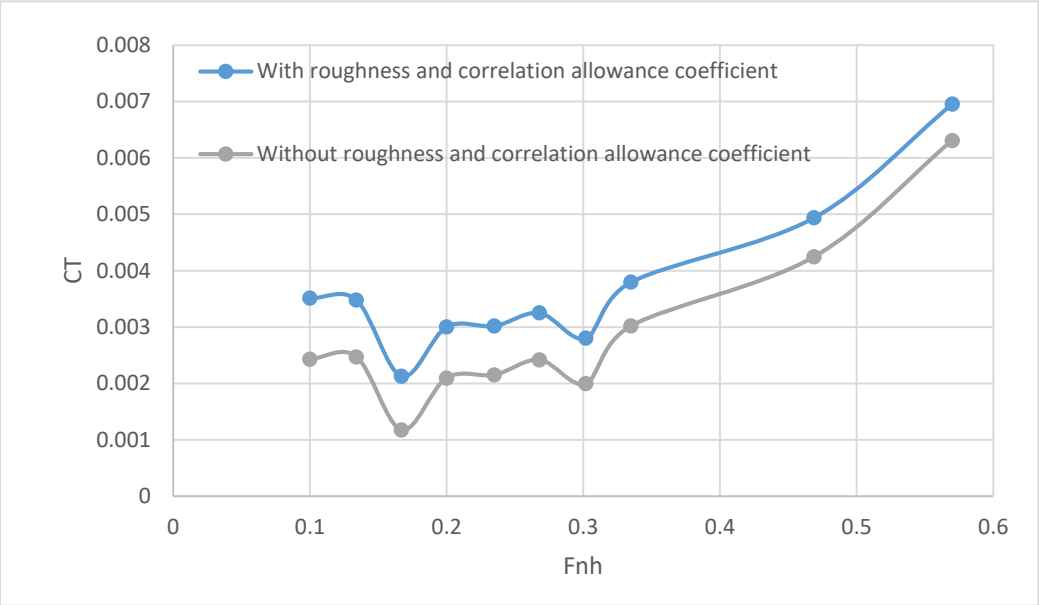

Figure 36 effect of the roughness allowance and correlation allowance coefficients on the total resistance coefficient values for case II at H/T = 2.2.

Regarding the trim angle results that's not needed to extrapolate because it is an angle it will be the same for full scale and model scale. The sinkage results are multiplied by the scale factor which is 75.

3.8 Concluding Remarks

This chapter has provided and documented very useful data regarding container ships sailing in shallow water, restricted channel or very narrow canals. It also experimentally approaches a very interesting phenomenon (squat, trim, and increased resistance) in shallow and narrow waters. Implementing uncertainty analysis on the test procedures and results increases the reliability and quality of the research findings. All plots are produced in nondimensional format such that they can be extended to similar cases. For example, the increasing in total resistance coefficient in Case I when the model run for H/T= 1.78 which present model draft 0.18 is 14% compared with the same case for H/T= 2.5 at Fn_h= 0.57. The same for sinkage/l_{pp} is increasing with 37.7%. Furthermore, the model trim by bow increase with 3.1% when the H/T for model decrease from 2.5 to 1.78 at the same case and Fn_h=0.57. Moreover, all data will be used as a benchmark to verify the CFD simulation analysis.

Finally, the study revealed that ship motions behaviour significantly changes in shallow water and restricted water compared to those in deep water. It would be very interesting to investigate experimentally high speed ship model more than Fn_h = 0.6 for Case II and Case III. Another piece of interesting in this study would be can use this benchmark for any type of ship as dimensionless parameters was performed in this chapter.

Chapter Four

4. AN EXPERIMENTAL INVESTIGATION OF THE TRIM EFFECT ON THE BEHAVIOUR OF A CONTAINERSHIP IN SHALLOW WATER

Accurate prediction data for ship squat and under keel clearance is crucial. This chapter presents the results of experimental work carried out at the Kelvin Hydrodynamic Laboratory at the University of Strathclyde, Glasgow, to study the effect of trim on containership sailing characteristics in shallow waters using KCS model. This chapter presents a series of model tests measuring the resistance, sinkage and trim variations with speed, water depth and loading conditions under different trimming angles. This was done to examine the range of ship trim for safe and efficient sailing in restricted water in both depth and width. The results indicated that for depth Froude numbers higher than 0.4, the ship model sinkage is less for aft trim than for level trim or forward trim. Concurrently, it can be observed that there is less water resistance for aft trim than for forward trim, albeit level trim shows the least resistance. The test was conducted for one value of model draft which was 0.144 m. Side bank effect was also examined.

4.1 Introduction

A series of model tests were conducted to measure the resistance, sinkage variations with speed, water depth and loading conditions under different trimming angles at 1:75 scale. The objective of this chapter's work is to examine the range of ship trim for safe and efficient sailing in restricted water in both depth and width. The study also aimed to provide data to be used in validating numerical computations to be carried on the same type of vessel to detect the best trim angle for ships during sailing in restricted waters to reduce resistance and therefore fuel consumption.

This chapter is organised as follows. Section 2 contains the specific details of the experimental setup, while section 3 presents uncertainty analysis. Section 4 is devoted to the obtained results and relevant discussion. Finally, the conclusion is given in Section5.

4.2 Experimental Setup

This experimental work has been conducted at the Kelvin Hydrodynamics Lab at the University of Strathclyde, as mentioned previously. The towing tank dimensions are illustrated in section 3.2.1 and Figure 37. The maximum speed of the towing tank carriage is 5 m/s which is driven along rails by a computer-controlled digital driven DC motor. The tank is equipped with a wavemaker able to generate regular and irregular waves up to 0.5 m high. The tank is also fitted with computer controlled unit for variable water depth. The water depth at the tank was set at 0.32 m for shallow water tests see Figure 37.

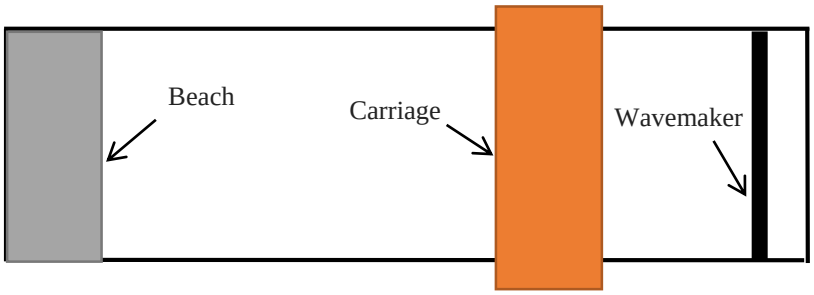

Figure 37 Schematic drawing of the towing tank

A KCS model was used to experimentally test squat and resistance characteristics at different speeds and loading conditions under different trimming angles in shallow water. Full scale and model scale particulars are given in Table 7.

Two LVDTs were employed to measure trim and sinkage. The sinkage $LVDT_1$ was attached at the mid ship point to measure the heave motion in dynamic mode and the trim $LVDT_2$ was attached at the model forepeak. Furthermore, a load cell was used to measure the water resistance force. This load cell was attached at the midship point, using the configuration described in Section 3.2.2.

The towing tank at Kelvin Hydrodynamic Lab was prepared for three test conditions and different blockage ratio conditions; each case at various speed. Furthermore, various trim angle for Case I are examined.

- ✓ Case I: This is similar to Case II in Section 3.2.1
- ✓ Case II: Similar to Case I but with reduced water surface width and bottom width. This case was designed for studying higher value of the blockage factor. (Refer to Figure 38a, b and Table 7)
- ✓ Case III: This is similar to Case I in Section 3.2.1

(a)

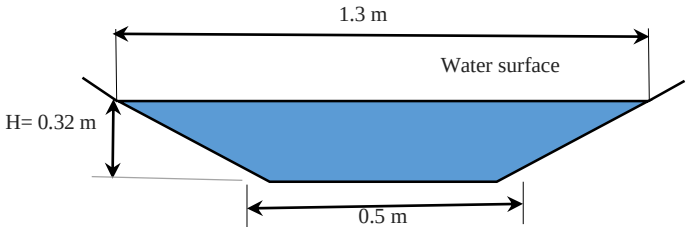

(b)

Figure 38 Depictions of the Case 2, a) schematic drawing and b) real photo from tank setup

Table 7 Blockage effect for Cases I, II and III ($\overline{W}$ is the mean tank width, T is the ship model draft and B is the ship model width)

	Model		Tank		Blockage ratio (K)
Case	B (m)	T (m)	$\overline{W}$ (m)	H (m)	$(B * T)/(\overline{W} * H)$
I	0.429	0.144	2.88	0.32	0.067
II	0.429	0.144	0.9	0.32	0.2145
III	0.429	0.144	4.6	0.32	0.042

All tests in three mentioned cases were performed in fresh and calm water. The model was only allowed to move in heave and pitch while others motions were restricted. Model resistance, trim, sinkage and actual speed of the model were recorded during the runs.
For a draft of 0.144 metres the tests were carried out for various number of trim angles at different model speeds. Selected trim angle range were 0, 0.3 by aft, 0.3 by fwd, 0.9 by aft and 0.9 by fwd.
Ballast brick inside the model were arranged in such a way to achieve the required trim see Figure 39. This trim was fine-tuned using the $LVDT_1$ and $LVDT_2$ with their inputs were fed to the "Spike" software within the tank acquisition system.

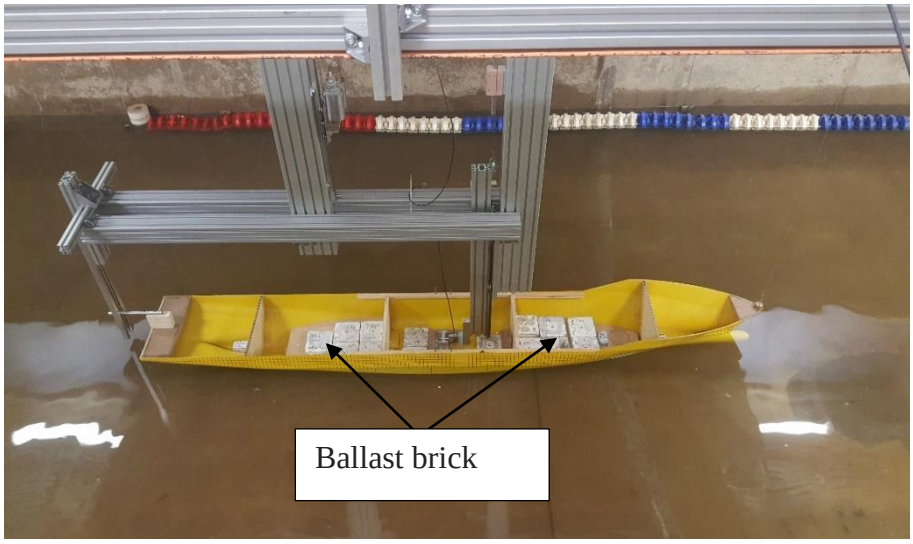

Figure 39 Free weights inside the KCS model

4.3 Uncertainty Analysis

The uncertainty values for total resistance, sinkage and trim at model scale speed 1.426 m/s are shown in Table 8. The resistance, sinkage and trim of this model are estimated at $\pm$ 0.45 %, $\pm$ 1.86 % and $\pm$ 4.92 % respectively at 95% of confidence level.

Table 8 Uncertainty of measurements for total resistance, sinkage and trim

Total resistance (RT)				
m/s	U_A (N)	U_B (N)	U (N)	Percentage
1.426	0.21	0.0286	0.212	± 0.45
Sinkage				
m/s	U_A (mm)	U_B (mm)	U (mm)	Percentage
1.426	0.428	0.572	0.714	± 1.86
Trim				
m/s	Combined Uncertainty U_C (deg.)			Percentage
1.426	0.0789			± 4.92

4.4 Experimental results and desiccation

In the present chapter, the total resistance, sinkage and trim of KCS hullform were measured in depth and width restricted water at different depth Froude number and blockage ratio. In this study one draft of 0.144 m was investigated for various depth Froude number between 0.1 to 0.67 and five different trim values; ranging from 0 to 0.9 degrees for case I.

3.4.1. Resistance

No significant change in the resistance values experienced by the model as far as trim is concerned up to 0.4 depth Froude Number (refer to Figure 40). Past Fnh = 0.4, level trim angle gave the lowest resistance. The test also reveals that resistance is a little higher for the trimmed by bow case than stern trimmed case.

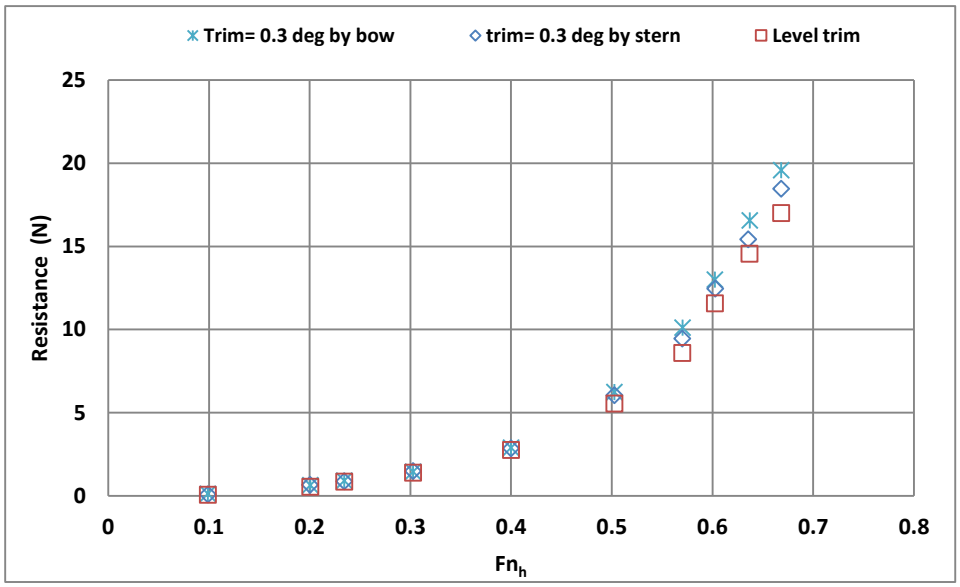

Figure 40 Total resistance comparisons between level trim and ±0.3 deg. trim

Figure 41 displays resistance variation with depth Froude numbers for a wider trim range (± 0.9°). Similar trend to Figure 40 was observed except for higher resistance due to trim.

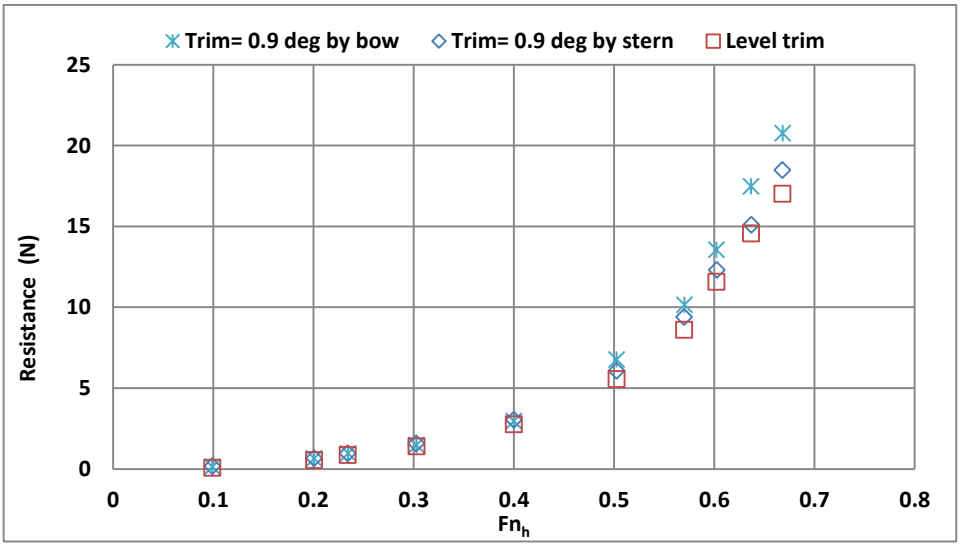

Figure 41 Total resistance comparisons between level trim and ± 0.9 deg. trim

Figure 42 displays total resistance variations versus positive and negative trim angle at 0.23 and 0.67 depth Froude numbers respectively. It is clear that for the high depth Froude number significant increase in total resistance when model was trimmed by bow by 18% for 0.9 degree and 13% for 0.3 degree, compared to level trim condition. In contrast, total resistance increases by 7.88% for 0.3 degree and 7.86% for 0.9 degree when model was trimmed by stern. Meanwhile, no variation in resistance with either aft or forward trim at relatively low Fn_h.

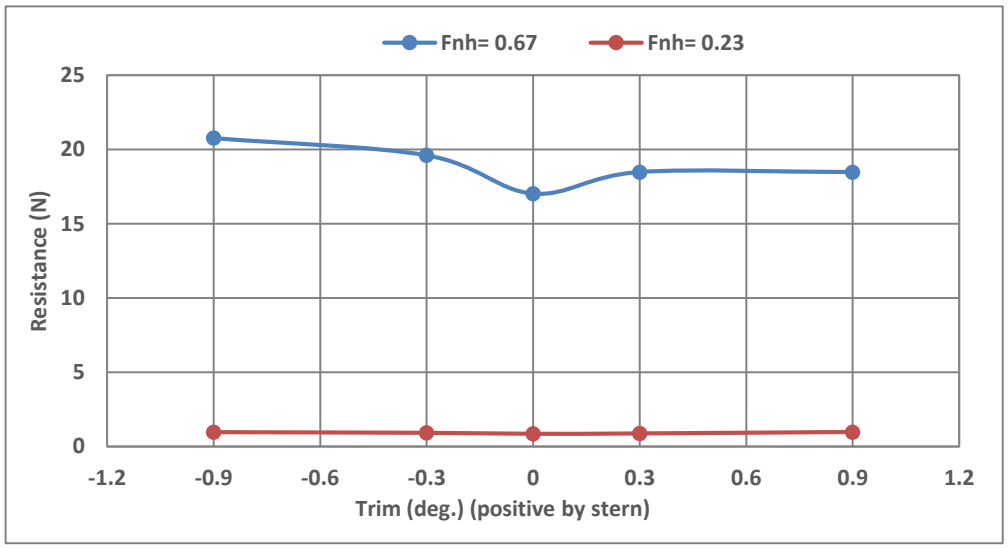

Figure 42 Total resistance for various trim angle at high and low speed.

3.4.2. Sinkage

Negligible change in the sinkage values was observed over the depth Froude Number range up to 0.4 as shown in Figure 43. Trimming by bow exhibits the lowest value of sinkage at about $Fn_h = 0.6$, lower sinkage values are observed past this Froude's number value for the three trim values tested.

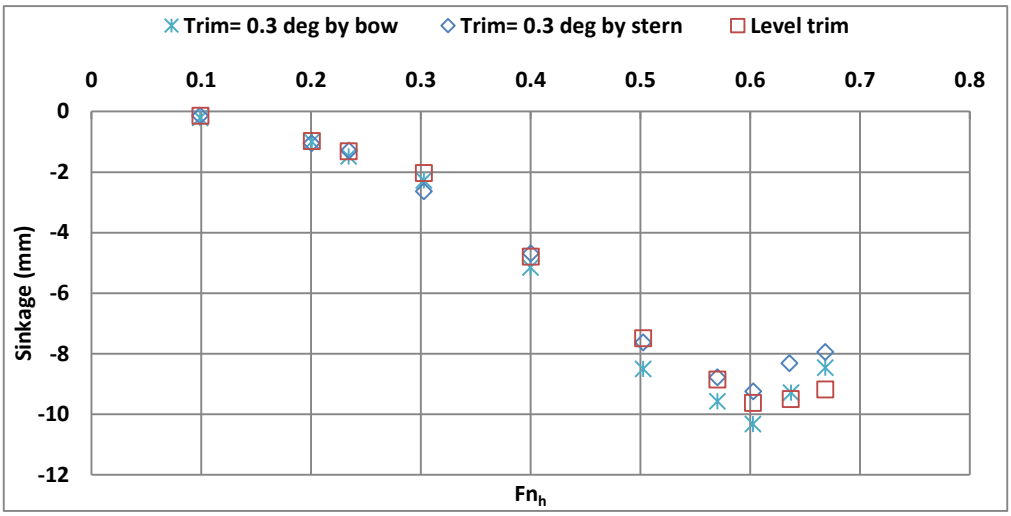

Figure 43 Sinkage comparisons between level trim and ± 0.3 deg. trim

Figure 44 shows sinkage variation with Fn_h at 0.9 degree aft and forward trim. It can be observed that, similar to the 0.3 trim by aft and forward behaviour, aft trim case indicated less sinkage values.

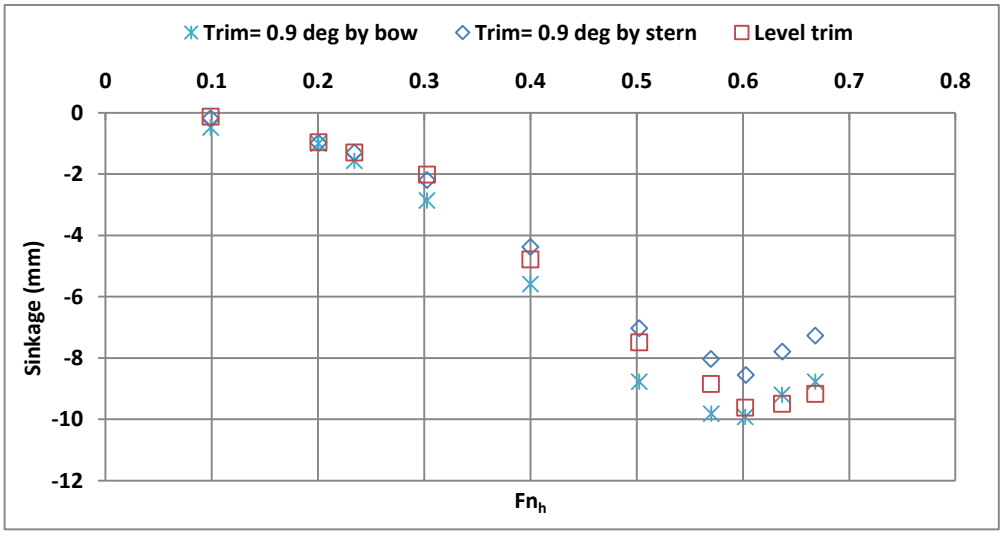

Figure 44 Sinkage comparisons between level trim and ± 0.9 deg. trim

Figure 45illustrates model sinkage variations versus trim at 0.23 and 0.67 depth Froude numbers. It can be noticed that for high depth Froude's number significant decrease in model sinkage when model was trimmed by stern (15.6 % for 0.3 degree and 26% for 0.9 degree), compared to level trim condition. On the other side, model sinkage decreases by 4.5% for 0.9 degree and 8.5% for 0.3 degree when model was trimmed by bow.

Furthermore, very small increase in model sinkage at slow speed when the model is trimmed by bow.

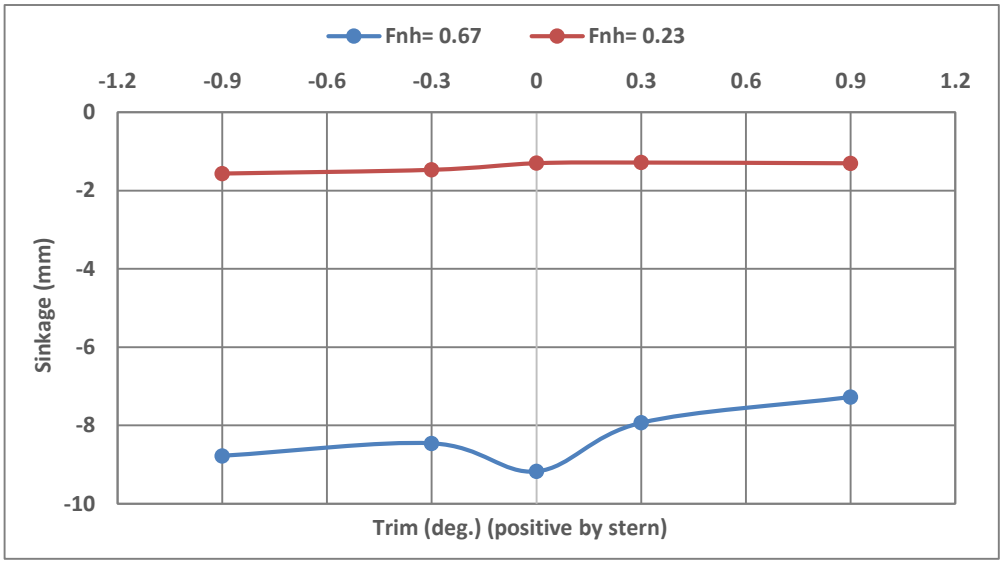

Figure 45 Model sinkage for various trim angle at high and low speed

3.4.3. Trim

Figure 46 and Figure 47 display the change in the model trim angles against depth Froude's number for three different model initial trimmed conditions. It can be observed that, no significant change in trim values for depth Froude Number range up to 0.4. In contrast, at Froude Numbers greater than 0.4, the ship trim angle tends to increase by stern for all values of model initially trimmed conditions. Level trim angle gave the optimum trim degree for high speed, while 0.9 degree by bow initially condition the largest trim degree value by stern.

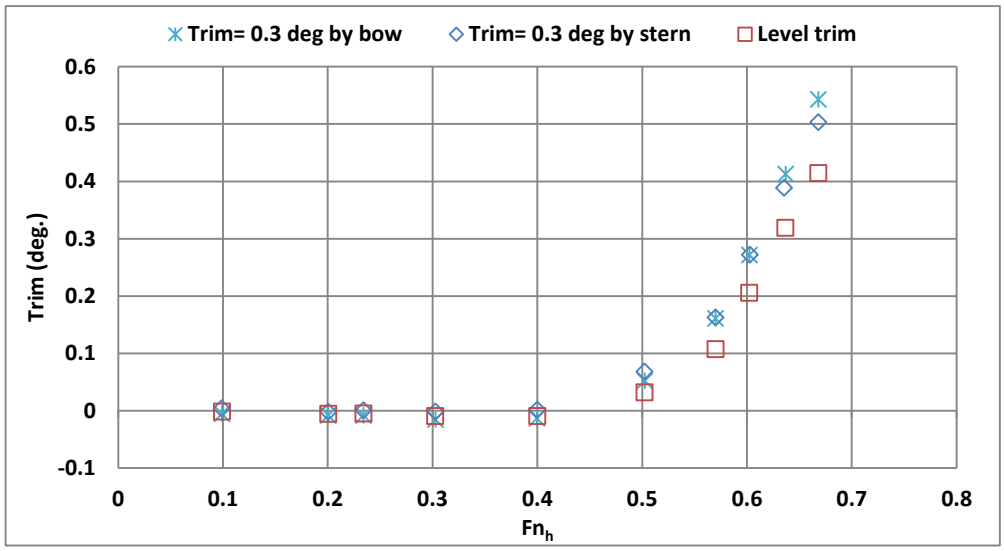

Figure 46 Trim deg. change for the two trim conditions at 0.3 deg. and level trim

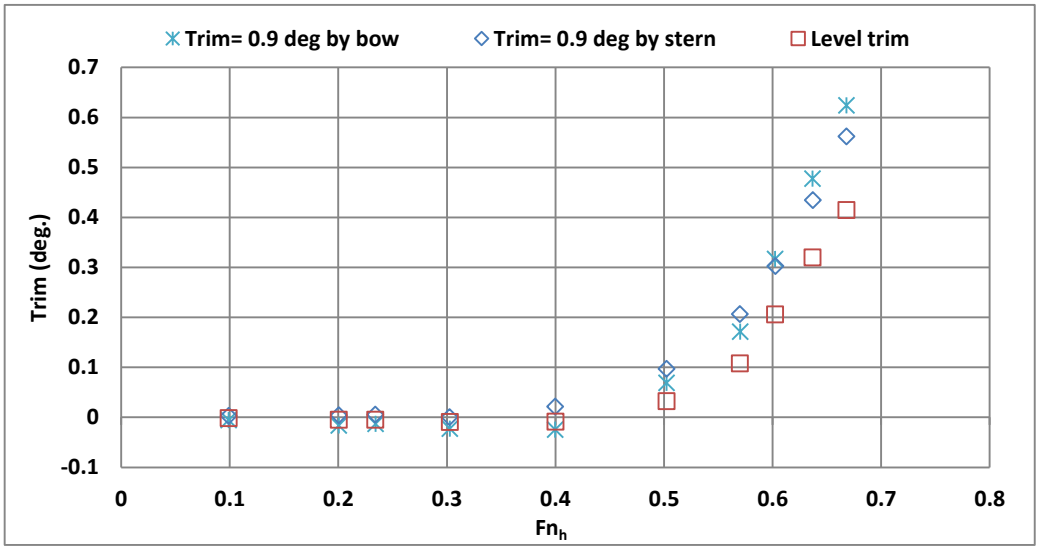

Figure 47 Trim deg. change for the two trim conditions at 0.9 deg. and level trim

Figure 48 illustrates the change in model trim angle variations versus trim angle initial condition by bow and by stern at 0.23 and 0.67 depth Froude number respectively. It can be noticed that for high depth Froude number significant increase in model trim by stern when model was trimmed by stern in initial condition by 33.5 % for 0.9 degree and 23.6% for 0.3 degree, compared to level trim condition. On the other side, model trim by stern increased by 26% for 0.9 degree and 17.6% for 0.3 degree when model was trimmed by bow in initial condition. Furthermore, slight significant change in model trim angle at slow speed when model trimmed by bow and stern.

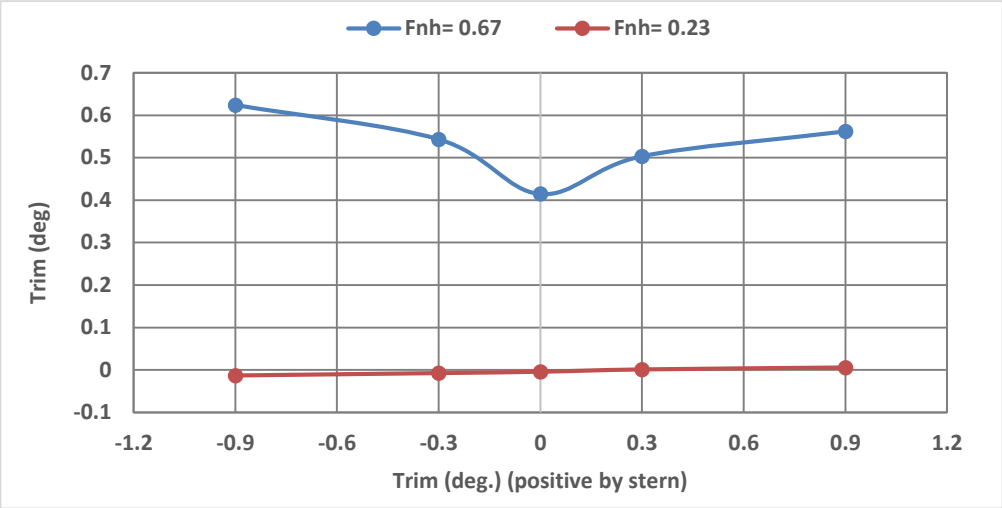

Figure 48 The change in model trim degree for various trim angle at high and low speed.

In summary, the loading condition level trim recorded the lowest value for the total resistance and trim values, while the loading condition trim by forward recorded the highest value of total resistance and trim values. However, the loading condition level trim recoded the highest value for sinkage, while loading condition trim by stern recorded the lowest value for sinkage.

3.4.4. Blockage ratio effect

Figure 49, Figure 50 and Figure 51 illustrate the blockage ratio effect on model total resistance and squat. It is clearly noted that, in Case I and Case II model behaviour change after 0.4 depth Froude number due to the combined effect of depth and width change blockage ratio.

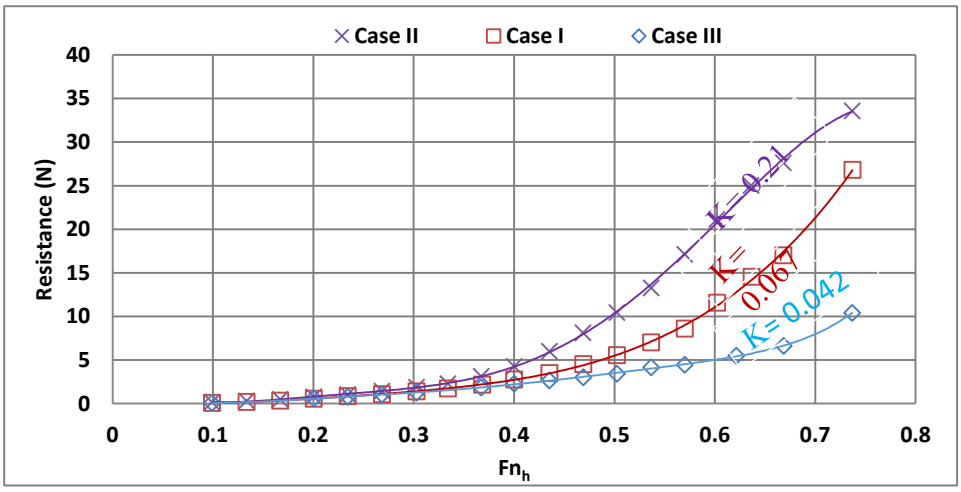

Figure 49 Blockage ratio effect on model total resistance

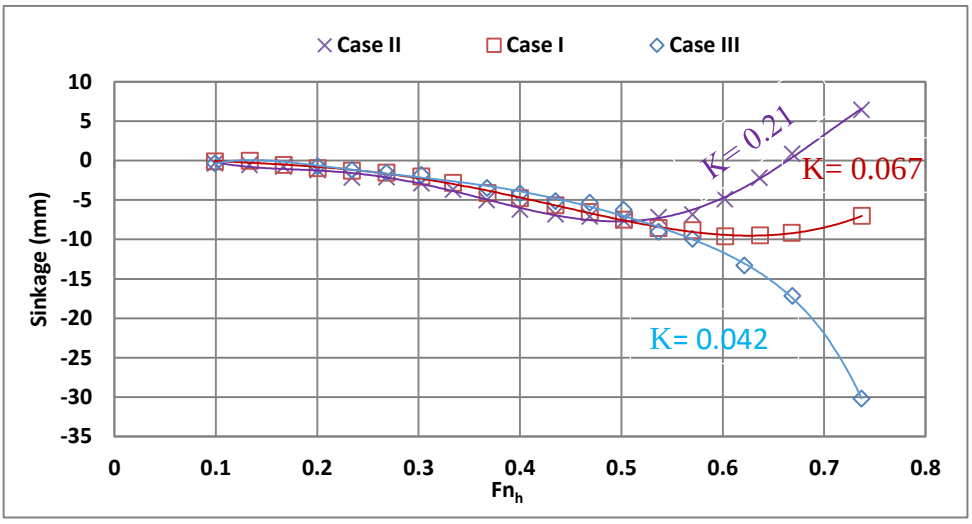

Figure 50 Blockage ratio effect on model sinkage

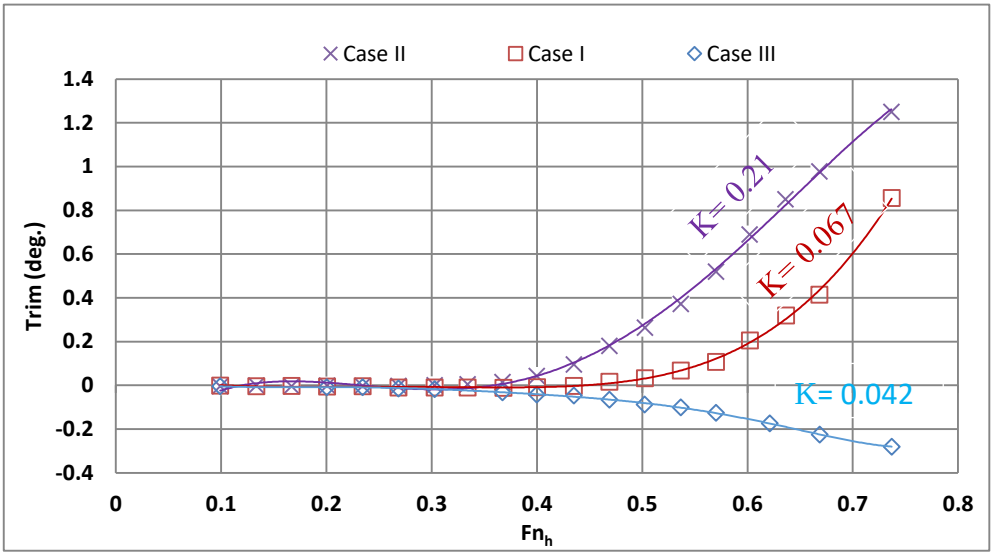

Figure 51 Blockage ratio effect on model trim angle

As a result, at high ship speed the velocity of return flow around the ship section cannot increase further and a pressure wave will be induced in front of the ship model due to accumulated water in the region, Lataire , E., et al(2012) (see to Figure 19). Furthermore, as per Bernoulli's principle, the velocity at ship model stern decreases and accordingly the pressure increases. Albeit, the pressure force acting on the bow will be stronger than on the stern. So, this explains the reason behind getting high aft trim at that low under keel value. On the other hand, the force acting on the ship model stern at subcritical speeds still not strong enough to create net force at the bow to decrease the sinkage of the model.

However, once model is run at critical speed the speed under the keel will became higher and will induce induced high pressure change at stern which leads to high force effect on the ship model stern. Accordingly, the net force acting on the ship model will increase and the sinkage will start to decrease, or remains constant when the blockage ratio exceeds critical value.

To calculate the critical depth Froude numbers for a given blockage ratio (K), using Equation (41) Lataire, E., et al (2012).

$$\mathrm{Fn_{h,crit}} = \sin\left(2\sin\left(\frac{\arcsin(1-\mathrm{K})}{3}\right)\right)^{\frac{3}{2}} \quad (51)$$

For Case 1 the blockage ratio K= 0.067, the critical speed will occur at Fn_h= 0.689 and it clearly noticed in Figure 46 that sinkage starts to decrease and model tends to go up.

Furthermore, for Case 2 the blockage ratio K= 0.214, the critical speed will occur at Fn_h= 0.457 and it also clearly noticed in Figure 50 that sinkage starts to decrease and model tends go up.

On the contrary, for Case III the blockage ratio K = 0.042, (very small) the critical speed will occur at Fn_h = 0.753, so this explains the reason why sinkage in Figure 50 for Case III keeps increasing while the model goes down.

4.5 Concluding Remarks

In this chapter, a series of experimental tests has been carried out for the KCS model focussing on trim optimisation. Furthermore, the influence of trim on ship total resistance, sinkage and initial trim were investigated in shallow water and width restricted channel.

It was observed that no significant impacts on KCS model total resistance, sinkage and trim in all cases studied were recorded over the depth Froude Number range up to 0.4.

It was also observed that level trim resulted in lowest resistance for high speeds. Albeit, there is less ship total resistance for the trim by stern case than for trim by bow case. Trim by bow recorded higher ship total resistance for all speeds.

On the other side, it can be noticed that for high depth Froude numbers model sinkage was significantly decreased when model was trimmed by stern, compared to level condition and trimmed by bow condition. Moreover, the level trim condition recorded the higher sinkage at high speed.

It is also important to consider the effect of both shallow and restricted water either separately or combined on the ship's sinkage, trim and resistance.

Finally, it's also be concluded that the section shape of canal will significant influence on the ship resistance and squat. This is because the blockage factor is a function of submerged midship cross-sectional area and the underwater area of the canal. As showed the change in the blockage factor results in reducing the critical depth Froude's number for deep water operation. The reduced $Fn_{h,crit}$ can be obtain by equation (32) where K is the actual blockage ratio and $Fn_{h,crit}$=f (H, K), if K=0 (for unlimited width) the equation 32 yields the known $Fn_{h,crit}$ of unity. In this study the deep water range is also reduced to lower value that of unrestricted (0.4 value) to 0.3.

Chapter Five

5. NUMERICAL STUDY ON HYDRODYNAMIC PERFORMANCE OF SHIPS ADVANCING THROUGH DIFFERENT CANALS

In international shipping, there are several waterways that are widely viewed as bottlenecks. Among these is the Suez Canal, where recent expansions have taken place. Although the Suez Canal has a high importance in international shipping, little research has been carried out in maximising the number of ships capable of traversing for a set period of time. The present chapter aims to examine hydrodynamic phenomena of ships advancing through the Suez Canal in the allowed speed range to determine the relative effects of the canal depth and /or width restrictions on the overall ship sailing performance. A rectangular canal is also included as a reference to gauge the effects of varying canal cross-section. The present study combines experimental, numerical, analytical and empirical methods for a holistic approach in calm water. As a case-study, the KCS hullform is adopted, and analysed experimentally, via Computational Fluid Dynamics, using the slender body theory, and empirical formulae. An in-house code is used to solve the slender body theory equations and empirical equations to compare results. The results reveal strong coupling between the canal's cross section and all examined parameters.

5.1 Introduction

When a ship enters shallow waters, it has been observed that the distance between the keel of the ship and the seabed decreases as the speed increases, and on occasion, the ship has been known to strike the bottom. This phenomenon is known as ship squat (Constantine, 1960). Because of the Bernoulli effect the free water surface around the ship drops. There is a vertical motion downwards and trim resulting in a decrease in the under-keel clearance (UKC). Thus all vessels squat as they move, even in deep water, although the magnitude of the squat is usually small. This phenomenon is a function of the shape of the hull and the forward speed through the water (Millward, 1996).

Ship squat is increased further when a vessel enters confined channels or rivers, since the velocity of water must increase due to the greater degree of restriction. Furthermore, a significant increase in resistance arises due to this hydrodynamic interaction. A drop in speed in the region of 30% can be expected upon entering shallow waters, which and may rise up to 60% if the ship is advancing through a confined channel such as a river or a canal (Barrass and Derrett, 2012).

Much research has been devoted to accurately predict ship squat, leading to a plethora of methods and approaches to the problem. Some of these are empirical methods, which are easy to use, but are reliable only for an early design stage (Barrass and Derrett, 2012; Rotteveel and Hekkenberg, 2015). Empirical formulae can quickly estimate the squat according to the ship dimensions, coefficients, speed, and underwater topology. These formulae are typically obtained from a series of model tests. Alternatively, analytical methods have been developed by researchers that make use of the assumptions inherent in potential flow theory such as slender body theory (Tuck, 1966). Namely, the flow is inviscid, irrotational and incompressible. Naturally, experimental investigations provide the most accurate results, and should be performed if possible (el Moctar et al., 2012; Zeraatgar et al., 2011). However, the availability of testing facilities, time required to perform the experiment, and the cost are highly prohibitive.

Finally, numerical, or Computational Fluid Dynamics (CFD) methods have been more recently developed and can be easily used for predicting ship squat. Although this approach has its own limitations, such as the computational cost, and knowledge required to perform a simulation, it is rapidly gaining popularity (Stern et al., 2013).

The present chapter combines all methods mentioned above. To elaborate, empirical formulae applicable in canal case-studies are used. The sinkage and trim of the ship are also analysed via the slender body theory as it is one of the most widely applied methods in this context. CFD simulations are also performed to replicate the experimental results and demonstrate the versatility of the numerical method. The analysis is performed on the KCS hullform, for which experimental data in shallow water is available for the specific case-studies examined herein chapter 3 and chapter 4.

This chapter is organised as follows. Section 2 contains the specific details relating to the implementation of each method. Section 3 is devoted to the obtained results and relevant discussion. Finally, the conclusion Remarks are given in Section 4.

5.2 Empirical, analytical and numerical methods

As alluded to in Section 1, experimentation has several drawbacks. In an attempt to circumvent the use of expensive and time consuming physical model tests, researchers have developed a wide variety of tools. Naturally, each of these is associated with a set of assumptions and limitations. There assumptions and limitations are discussed in the following sections.

5.2.1. Reynolds-averaged Navier-Stokes (CFD)

Perhaps the most rapidly developing field in ship hydrodynamics involves the use of Reynolds-averaged Navier-Stokes (RANS) methods. These solve for the 3D fully nonlinear viscous flow around the ship. The rapid development of supercomputers, coupled with the RANS method's ability to resolve complex flow phenomena with good accuracy has meant that many researchers have adopted the RANS method in their toolkit.

In this chapter, the rectangular canal depicted in Figure 57 will be modelled. Naturally, the speeds examined replicate the model-test parameters. This implies that all ship dimensions and parameters follow those, prescribed during the experimental investigation. The commercial available RANS solver, Star-CCM+, version 13.02.011 is used in this study. Star-CCM+ is a finite-volume based solver, which uses the integral form of the governing equations and divides the computational domain into a finite number of adjoining cells.

5.2.1.1 Mesh generation

For the present investigation, hexahedral cells of minimal skewness are used. This is known to provide superior predictions in ship hydrodynamics when compared to tetrahedral cells (Jones and Clarke, 2010). The mesh is generated via the automatic facilities of Star-CCM+. To accomplish this, the trimmed cell mesher is used to construct

all cells outside the immediate vicinity of the ship. The near-wall cells are prescribed via the prism layer meshes, which is set to ensure a $y^+<1$ over the wetted area of the ship. In doing so, high local wall-based Reynolds numbers, which require the use of wall-functions are avoided. This is done in view of the fact that wall functions are incompatible with separation and complex phenomena, such as stagnation and recirculation (Durbin and Pettersson Reif, 2011). The resulting cell numbers can be consulted in **Error! R eference source not found.**. The generated mesh is depicted in **Error! Reference source not found.** for both case-studies figure 52. Figure 53 depicts the mesh resolution as generated for both case-studies on the fore and aft of the ship surface, including the distribution of the near-wall cells on a plane, coincident with the undisturbed free surface. While the resulting y^+ values distribution on the hull are shown in figure 54**Error! R eference source not found.**.

The depicted mesh is achieved by imposing concentric volumetric refinements in the vicinity of the ship. In particular, the location where the Kelvin wake is expected has been refined considerably in the rectangular canal case. For the Suez Canal, the refinements are concentrated near the lateral extents of the canal. As will be shown in Section 5.3, the manner in which the waves interact with the bottom is important. The mesh density required in these areas is increased when compared to other locations. In any case, the mesh in the Suez Canal is sufficiently refined to capture the waves everywhere in the domain. Although this implies that the cell numbers have increased dramatically, as shown in table 9**Error! Reference source not found.**, the heightened computational e ffort is considered justified.

Table 9. Cell numbers

Case-study	Simulation type	Number of cells
Rectangular canal	Multiphase	1446076
	Double body	1055015
Suez Canal	Multiphase	1954292
	Double body	1038586

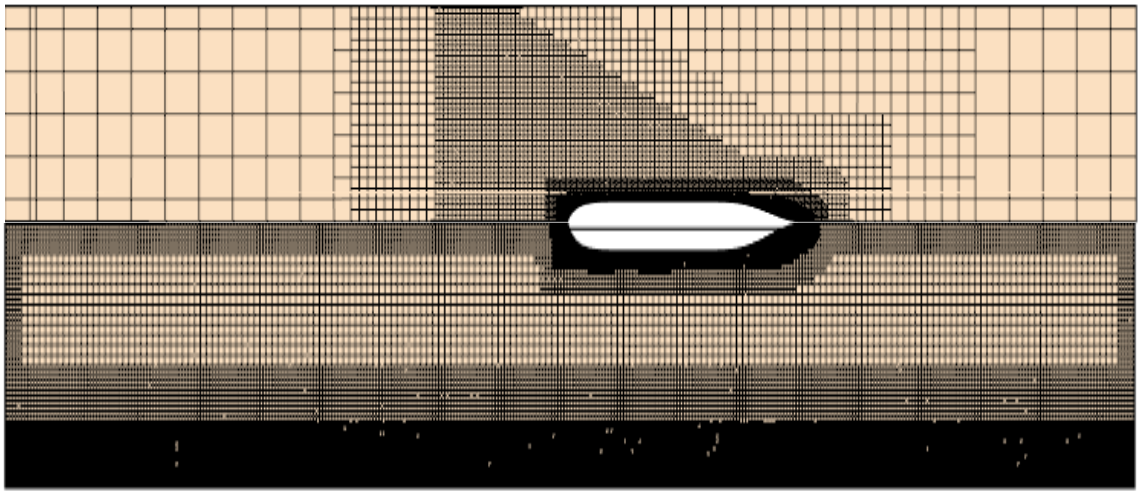

Figure 52. Top view of the generated mesh for the rectangular canal (top half) and Suez Canal (bottom half) – not to scale.

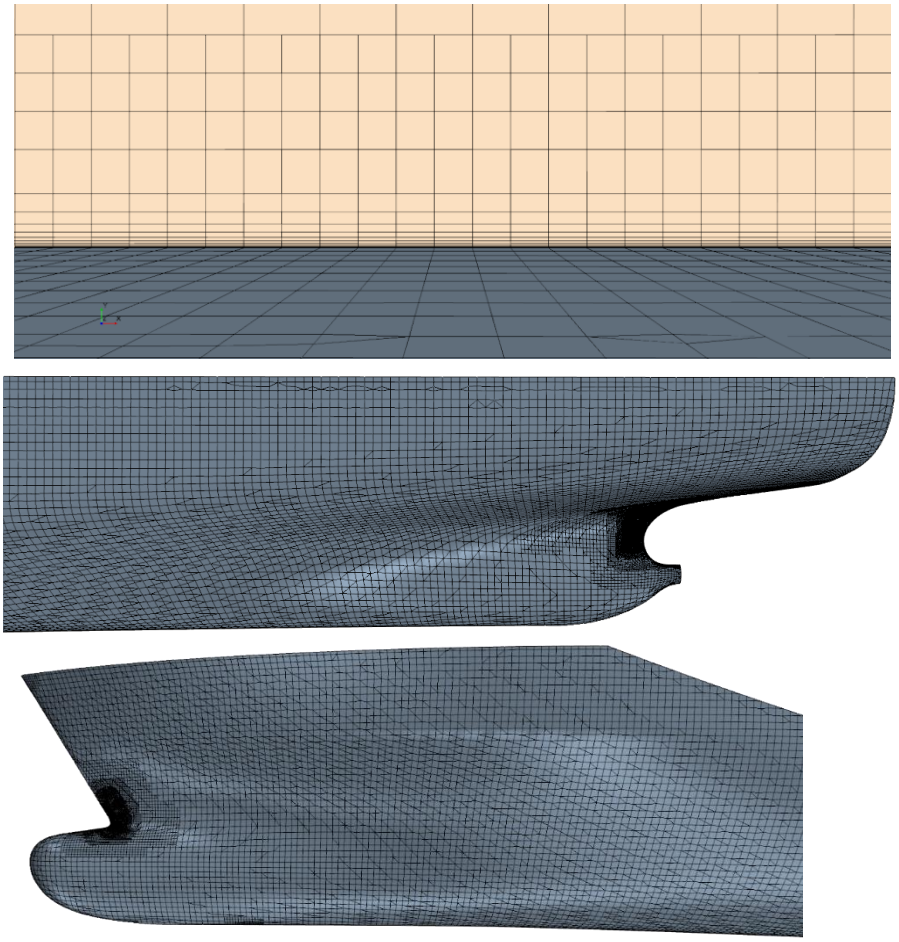

Figure 53 Mesh on the ship hull, as generated for all case-studies. Top: near-wall cell distribution, middle: forward, bottom: aft

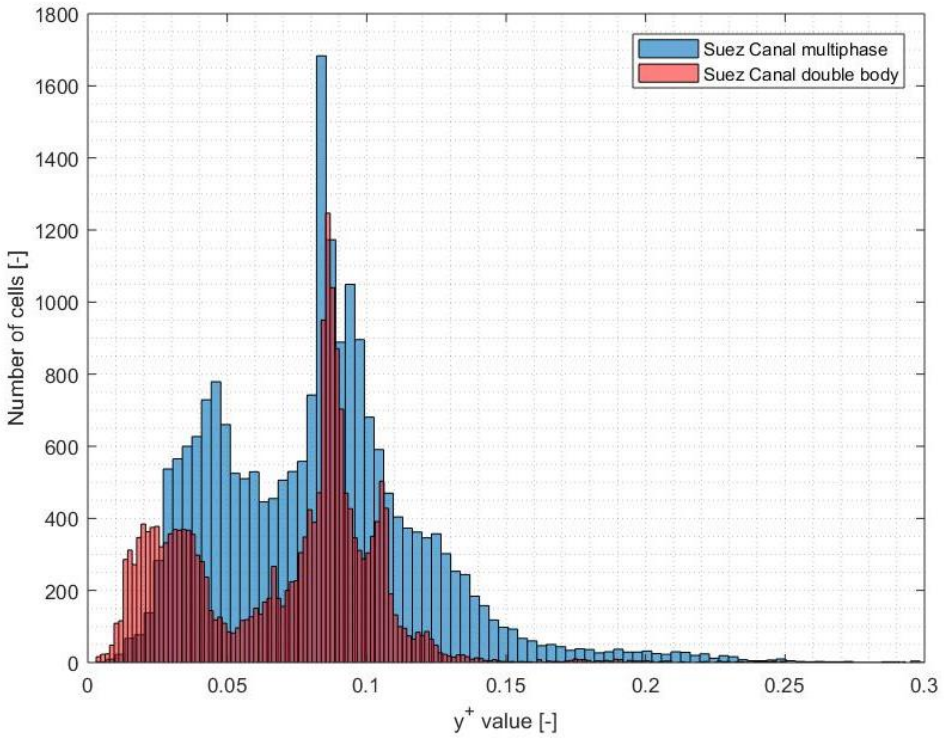

Figure 54. Distribution of y^+ values in multiphase and double body modes for the Suez Canal at F_h =0.2439.

5.2.1.2 Numerical set-up

In terms of numerical set-up, the recommendations of Terziev et al. (2019b) are followed. Namely, a 2nd order convection scheme is adopted and the k – ω turbulence model is used, which showed reliable predictions over a range of similar case-studies (Terziev et al., 2018; Wilcox, 2006). The k – ω turbulence model exhibited good, consistent predictions over a range of case-studies, similar to those examined here. The wall time, required per iteration was also found to be the lowest of all two equation turbulence models, making it a highly attractive choice. Additionally, the k – ω turbulence model does not require any modifications if applied near solid boundaries, when attempting to resolve boundary layer phenomena, which govern resistance. The present study will also serve to validate the assertion that the k – ω turbulence model provides good predictions over a greater range of case-studies. The expectation is that the resistance will be predicted with a small, negative error based on previous experience (Terziev et al.,

2019b). The temporal term of the Navier-Stokes equations is discretised via a 1st order accurate scheme, with a time-step of t=0.0035×L/V, following Tezdogan et al. (2016). In the present simulations, the mesh remains constant for all speeds, while the time step is varied according to the aforementioned formula.

To model ship squat, the Dynamic Fluid Body Interaction (DFBI) module is used. This computes the normal (pressure) forces and tangential (shear or frictional) forces on the ship hull and adjusts its position to achieve equilibrium. In the examined case-studies, only motions in the vertical plane (y – z) are allowed. To dampen the initial shock, resulting from the initiation of the simulation, the ship is constrained during the first 10 seconds, which is imposed to allow the flow to develop before the ship is allowed to move. Once this time limit has been overcome, the solver gradually applies forces and moments on the hull during an additional 10 seconds.

5.2.1.3 Computational domain

The domain dimensions follow the recommendations of the ITTC (2017). While the domain bottom, set as a velocity inlet, and side (slip wall) are prescribed to match the experimental set-up, the domain top is placed at a distance of 1.5×L from the undisturbed water surface level. The inlet is also positioned 1.5×L upstream of the forward perpendicular, where a velocity inlet condition is imposed. The outlet is located 2.5×L ship lengths downstream of the aft perpendicular, and is set to maintain the hydrostatic pressure figure 55. To calculate the hydrostatic pressure, model current velocities, and capture free-surface deformations, the Volume of Fluid method is utilised (Hirt and Nichols, 1981). Domain dimensions and boundary conditions are summarised in **Error! R eference source not found.** for the rectangular canal (top) and Suez Canal (bottom).

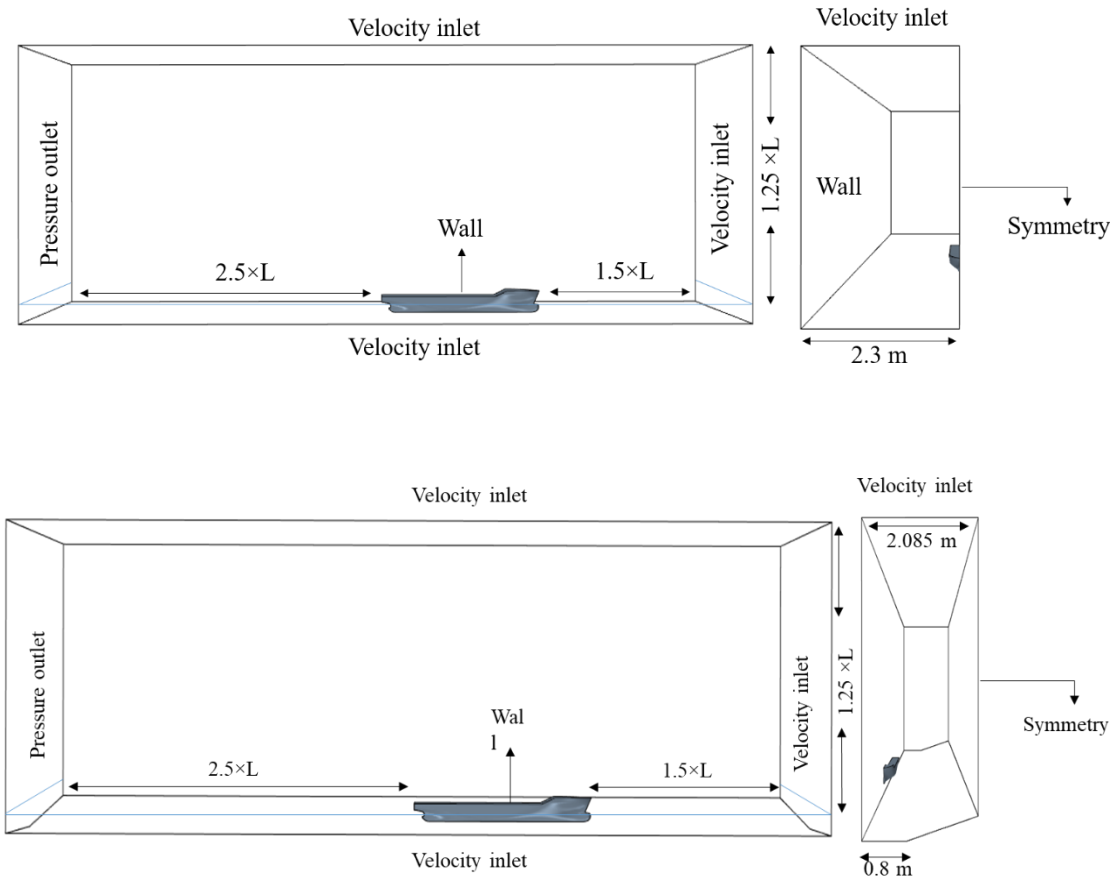

Figure 55. Domain dimensions and boundary conditions in all multiphase simulations. Top: rectangular canal, bottom: Suez Canal (not to scale).

In an attempt to demonstrate changes in the components of ship resistance, a multiphase simulation is insufficient. As mentioned previously, the RANS solver computes forces as normal and tangential. These translate into frictional and pressure resistance coefficients upon division by $0.5\rho SV^2$, where ρ=997.561 kg/m^3 is the fresh water density, S is the ship's wetted area, and V is the ship speed. On the other hand, the resistance extrapolation procedure, endorsed by the ITTC (2017b) decomposes the total differently. Namely, the form factor approach is used, suggested by Hughes (1954), which splits the resistance as shown in Eq. (52).

$$C_T = C_F \times (1 + k) + C_W \quad (52)$$

where C_T is the total resistance coefficient, C_F represents the frictional component, (1+k) is the abovementioned form factor, and C_W is the wave resistance coefficient. C_W and (1+k) are assumed constant with scale, while C_F is predicted via a friction line (Molland et al., 2017). Since CFD cannot be used to predict all of these components via a multiphase simulation, one may replace the free-surface with a symmetry plane (Kinaci et al., 2016). Essentially, this is equivalent to removing C_W from Eq. (3), since there are no longer any waves present in the simulation (Farkas et al., 2017). Doing this renders the VOF method inapplicable. For this reason, in double body simulations the velocity is prescribed at the inlet as a constant, while the outlet maintains 0 Pa pressure.

To ensure the flow is dissimilar only due to the absence of waves, the ship's vertical position is adjusted, according to the result obtained by the multiphase simulation (Terziev et al., 2019c). Performing double body simulations allows for the calculation of the wave resistance simply by subtracting the C_T achieved in multiphase and double body regimes (Min and Kang, 2010). Furthermore, the form factor is simply the double body total resistance, divided by the double body frictional component. These will enable the prediction of changes in (1+k) and C_W with speed as well as bathymetry. For the typical cell numbers, achieved for the double body simulations, **Error! Reference source not found.** can be consulted.

The double body approach is primarily adopted in this chapter to determine the wave resistance of the KCS under different conditions. Utilising the resistance decomposition shown in Eq. (84), it is possible to circumvent the complexity of wave resistance estimation. To elaborate, wave resistance estimation in shallow water is a particularly difficult problem. While there are many theories capable of providing an estimate of the sinkage and trim of the ship, resistance in the subcritical range has proved elusive (Beck et al., 1975; Tuck, 1967a, 1966). That is, although deep-water wave resistance can be estimated with the same theory (Tuck and Lazauskas, 2008). Three-dimensional potential flow theories are required to predict ship shallow water wave resistance, which are characterised by a substantial increase in implementation difficulty. For example, Yuan's (2018) method can be used in this respect. However, in the absence of commercially available software, where the above theory has been implemented, one cannot apply it in practice routinely.

The generated computational domains, for multiphase and double body regimes in both canals are shown in Figures 56

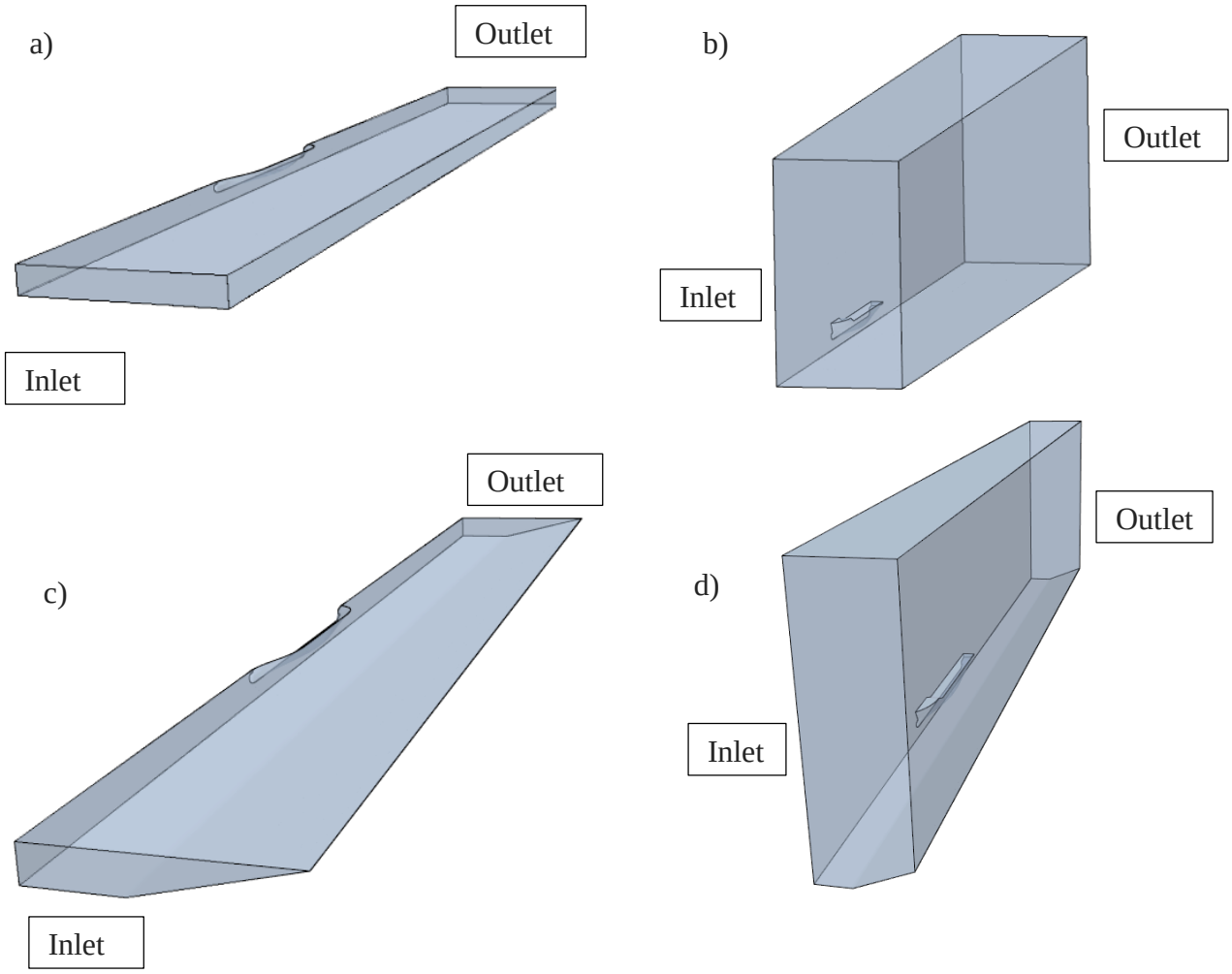

Figure 56 a double body tank geometry in the rectangular canal. B multiphase tank geometry in the rectangular canal. C Double body tank geometry in the Suez canal. D. Multiphase geometry in the Suez canal.

The problems associated with wave resistance in shallow water are further magnified by two factors. Firstly, shallow water flows are highly three-dimensional. As demonstrated recently by Terziev et al. (2019b), the boundary layer of the ship is predicted to come in contact with the seabed in very shallow water cases. This brings about the second

difficulty, referred to previously, namely, non-linear effects. The presence of such phenomena suggests that the vast majority of shallow water theories are inapplicable, even if they provide non-zero predictions. For instance, the extension of the slender body theory to account for ship-ship interactions of Gourlay (2009) can be supplemented by additional non-linear terms, as shown by Yeung (1978). In fact, the supplementing terms, introduced in the latter reference have been shown to be of similar magnitude as the original terms, formulated by Tuck and Newman (1976).

Non-linearity and three-dimensional effects are not a distinctive problem when it comes in CFD predictions. The RANS equations feature both of the above characteristics. Therefore, CFD can provide insight into the phenomenology of the underlying physics without user intervention, or knowledge of separate linear/non-linear and 2D/3D effects. These are captured automatically in the computational model. In this context, the prediction of the form factor, which is typically used to account for 3D effects is trivial in the presence of data from multiphase and double body simulations. The prediction of the form factor is of importance because of its central role in resistance extrapolation.

In the likely event where the expected routes the ship will spend the majority of its operational lifetime are known, it is of critical importance to predict the full-scale resistance under these conditions. The manner in which this is typically done is via the resistance decomposition, shown in Eq. (86). Naturally, the use of this relationship requires adequate knowledge of each component on the left-hand side of the equation. As explained previously, wave resistance is associated with a distinct set of challenges. The form factor is also an elusive parameter, which is not sufficiently understood in shallow waters. Frictional resistance in shallow water is also subject to some debate, because as will be shown in Section 5.3, the ITTC line cannot capture shallow water effects. Zeng et al. (2018) provided a basis for a correction based on the depth over draught ratio (h/T), but their formulation is applicable for flat ship bottoms. This is certainly not the case in the vast majority of cases due to the occurrence of ship squat, and is therefore not applied here.

In the presence of continual debate regarding each component of the resistance decomposition shown in Eq. (86), and indeed the relationship itself, it is thought prudent to investigate the RANS solver's performance in predicting these parameters. The

availability of experimental data to compare the numerical predictions against is used to establish confidence in the numerical model where appropriate. To the best of the knowledge, form factor and wave resistance studies in shallow waters are few, especially with changing channel cross-section. Thus, the present investigation would serve to supplement knowledge in the field by predicting the expected changes in all factors discussed above.

The results and relevant discussions are given in Section 5.3, while the following Section provides an overview of the errors and uncertainties induced as a result of the RANS method.

5.2.2. Numerical verification

As referred to in the previous section, RANS solvers require a time step and grid size to discretise the governing equations temporally and spatially, respectively. The set of partial differential equations, modelled by the solver (the RANS equations) are thought to represent the physics of the problem with sufficient accuracy (Lesieur, 2008). However, this applies to their continuum form, which are solvable and can be used for relatively simple flows. In any case, analytical solutions to the Navier-Stokes equations in three dimensions are rare, and cannot be derived for a problem as complex as multiphase (or double body) flow about a ship hull. For this reason, verification procedures are devised to estimate the error, resulting from either mode of discretisation, and the corresponding uncertainty by extrapolating the solution to a 0 time step or grid size (Roy, 2005). In other words, the solution estimated as if it were possible to model the continuum form of the partial differential equations.

For the present case, the Grid Convergence Index (GCI) method is used, which was devised by Roache (1998) as a uniform method to report numerical uncertainty. This method uses generalised Richardson Extrapolation (Richardson, 1911), and provides a 95% confidence in the computed uncertainty (Roache, 1997). To elaborate, upon estimating the uncertainty, one can have sufficient grounds to maintain that the exact solution lies within the bracket, calculated as the uncertainty. Therefore, the error is

defined as a quantity characterised by a magnitude and sign, whereas the uncertainty simple provides an interval, within which the error must be located 95 out of 100 times.

The first step in the verification procedure is to define a refinement ratio (r), which is used to magnify the grid size, or time step. Here, the recommendation of the ITTC (2008) are adopted in this respect, namely r=$\sqrt{2}$. The refinement ratio is used to generate a triplet of solutions, which are used to predict the numerical error (Celik et al., 2008). Here, it is useful to define the modes of convergence or divergence. These are characterised by the convergence ratio, R, whose value defines four possibilities:

1. Monotonic convergence: $\mathbf{0} < \boldsymbol{R_\kappa} < \mathbf{1}$
2. Oscillatory convergence: $\mathbf{R_\kappa} < \mathbf{0} \cup |\boldsymbol{R_\kappa}| < \mathbf{1}$
3. Monotonic divergence, $\boldsymbol{R_\kappa} > \mathbf{1}$
4. Undefined error or uncertainty

Where the subscript refers to the κ^{th} input parameter. In the present context, *R* is defined as the ratio of the difference between medium and fine solutions $\varepsilon_{21} = (\varphi_2 - \varphi_1)$, and the difference between coarse and medium solutions $\varepsilon_{32} = (\varphi_3 - \varphi_2)$. Once these are known, the observed order of accuracy is estimated as shown in Eq. (53):

$$p_\kappa = \frac{\ln(\varepsilon_{\kappa 23}/\varepsilon_{\kappa 21})}{\ln(r_\kappa)} \tag{53}$$

The next step is to predict the extrapolated value, formulated in Eq. (54):

$$\varphi_{ext} = (r_\kappa^p \times \varphi_1 - \varphi_2)/(r_\kappa^p - 1) \tag{54}$$

Then, the approximate relative error and extrapolated relative error are calculated as shown in Eq. (55) and Eq. (56), respectively.

$$e_a^{21} = \left|\frac{\varphi_1 - \varphi_2}{\varphi_1}\right| \tag{55}$$

$$e_{ext}^{21} = \left|\frac{\varphi_{ext^{21}} - \varphi_2}{\varphi_{ext^{21}}}\right| \tag{56}$$

Once the quantities estimated by Eq. (55) – Eq. (56) are known, the uncertainty can be calculated as expressed in Eq. (57):

$$GCI_{fine}^{21} = \left|\frac{1.25 \times e_a^{21}}{r_k^p - 1}\right| \quad (57)$$

The computed data for this case is shown in **Error! Reference source not found.**, where g rid discretisation uncertainty is reported. **Error! Reference source not found.** presents estimates of the temporal discretisation-induced uncertainty. The procedure has been carried out for sinkage, trim and total resistance. Since the total is simply the sum of the pressure and shear, it is not thought necessary to extend the reported results for the remaining parameters. The uncertainty analysis presented in this section was performed for the rectangular canal for F_h =0.469. This is used as a representative case, providing guidelines in terms of uncertainty for the remaining case-studies.

It is interesting to note that sinkage and trim exhibit super convergence with mesh refinement, but are close to the theoretical order of accuracy (p_t=2) when subjected to temporal refinement (Roy, 2005). The opposite is true in terms of resistance.

Table 10. Spatial uncertainty in the rectangular canal, F_h =0.469.

	Sinkage (m)	Trim (°)	Total resistance (N)
r (-)	$\sqrt{2}$	$\sqrt{2}$	$\sqrt{2}$
φ_1 (1446076 cells)	-0.0052	-0.0675	2.8896
φ_2 (773798 cells)	-0.0054	-0.0682	2.9559
φ_3 (542400 cells)	-0.0104	-0.0756	3.0935
R (-)	0.04	0.096573	0.4818
p (-)	9.2877	6.7445	2.1068
φ_{ext}^{21}	-0.005	-0.066831	2.8233
e_a^{21} (%)	0.0192	0.009	0.021
e_{ext}^{21} (%)	0.08	0.0204	0.0469
GCI_{fine}^{21} (%)	7.5321	1.9867	2.463

Table 11. Temporal uncertainty in the rectangular canal, F_h =0.469

	Sinkage (m)	Trim (°)	Total resistance (N)
r (-)	$\sqrt{2}$	$\sqrt{2}$	$\sqrt{2}$
φ_1	-0.0052	-0.0675	2.8896
φ_2	-0.00517	-0.0674	2.8883
φ_3	-0.005169	-0.0670	2.8823
R (-)	0.41748	0.50193	0.21667
p (-)	2.5205	1.9889	4.4129
φ_{ext}^{21}	-0.0051831	-0.067718	2.8909
e_a^{21} (%)	0.00019	0.263	0.045
e_{ext}^{21} (%)	0.059678	0.0111	0.0009
GCI_{fine}^{21} (%)	0.077	0.2926	0.0775

To ensure that the solution has converged sufficiently, the residuals are monitored, requiring a minimum drop of at three orders of magnitude, following the recommendations of the ITTC (2011). To assess iterative errors, the non-intrusive, *a* posteriori method of (Roy and Blottner,2001) is used (Phillips, 2012). The results from this analysis indicate that absolute errors are in the range of 10^{-5} – 10^{-6}. To achieve the here reported levels of iterative convergence, the solution is allowed to evolve for a minimum of 200 s physical time. The iterative errors must be several orders of magnitude smaller than the discretisation error to enable the applicability of the GCI (or any other) discretisation uncertainty estimator technique (Eca and Hoekstra, 2014). For the present purposes, this condition is thought to have been satisfied.

5.2.3. Empirical method

Empirical methods are typically derived based on a regression technique, employed on a dataset. A common problem with this approach is that upon extrapolating variables beyond the range contained within the dataset introduces errors. The abovementioned dataset is usually experimental (Duffy, 2008). In the realm of ship hydrodynamics, the number of parameters, one must account for are high, rendering the problem difficult. A superimposed issue is that a slight alteration in any of the modelled (or otherwise)

independent parameters induces a substantially different case-study than what the empirical method is suited for. For example, introducing a slope in the bathymetry changes the flow physics, versus a rectangular canal.

The empirical methods used here require idealised conditions, which are rarely present (PIANC, 2014). Although these conditions are also assumed idealised in the remaining methods, their applicability is not restricted in the same manner due to their ability to encompass different conditions. For instance, one can model waves using RANS (Tezdogan et al., 2016b), and using potential flow (van Oortmerssen, 1976) in shallow water if required to assess the operational condition. Other applications include ship-ship interactions, which create the same restrictions (Kok et al., 2018; Tuck and Lazauskas, 1998; Yuan and Day, 2015), as well as ship-bank interactions (van Hoydonck et al., 2018; Yuan, 2018).

In the present case, the hullform is also of critical importance. Even slight variations in the wetted shape of the ship can have dramatic consequences in terms of the behaviour and performance of a ship (Tezdogan et al., 2016a). Coincidently, this is also the main motivation of hull form optimisation studies (S. Zhang et al., 2017; Zhang et al., 2018a, 2018b). A change in depth or width also invalidates any analysis that was not performed using a similar set-up. This is the main problem of empirical methods: their predictions may be excellent for the case-study used in their inception, but this is far from the case in any other case-study. This drawback stems from the range and number of parameters required to describe the flow around a ship. A simple length to beam, draught, depth etc. is insufficient to provide information on the actual flow characteristics. For the present chapter, the Suez Canal is modelled as shown in Figure 57, and explained in the following section (Section 5.2.2).

For the purposes of this research, several empirical formulae derived from experimental databases were employed in this study. Naturally, only those applicable to canal case-studies are examined, although the MATLAB-based in-house code, first utilised in Terziev et al. (2018) is capable of employing a wide variety of empirical formulae for unrestricted (U), restricted (R) and canals (C). The full description of the mathematical background, of the empirical formulae are as follows:

Barrass, (1981), proposed a formula for bow squat S_b based on validation with full-scale measurements as in Equation 58.

$$S_b = \frac{C_B S_2^{2/3} V^{2.08}}{30} \quad (58)$$

where C_B is the block coefficient of the ship, V is the ship speed and S_2 is the velocity return factor.

$$S_2 = \frac{A_S}{A_C - A_S} \quad (59)$$

where A_C is channel cross sectional area and A_S is the ship cross sectional area.

In order to use this formula requires to be effective width of waterway W_{eff} be at least equal to 8 beam widths for unrestricted channels. The effective width of waterway can calculated from equation 60:

$$W_{eff} = C_M B = [7.7 + 45(1 - C_{WP})^2] \quad (60)$$

where C_M is midship section coefficient, B is ship beam amidships and C_{WP} is water plane coefficient.

Eryuzlu and Hausser (1978) conducted physical model tests of large, fully-loaded self-propelled tankers in unrestricted channels, and got the following expression for S_b

$$S_b = 0.113B\left(\frac{1}{h/T}\right)^{0.27} Fn_h{}^{1.8} \quad (61)$$

Eryuzlu et al. (1994), conducted physical model tests to predict bow squat in restricted channels bow squat S_b, as given by Equation 62.

$$S_b = 0.298\frac{h^2}{T}\left(\frac{V}{\sqrt{gT}}\right)^{2.289}\left(\frac{h}{T}\right)^{-2.972} K_b \quad (62)$$

where K_b is the correction factor as shown in Equation 63.

$$K_b = \frac{3.1}{\sqrt{W/B}} \text{ for } W/B < 9.61 \text{ and } 1 \text{ for } W/B \geq 9.61 \quad (63)$$

The effective channel W_{eff} should be used for the channel width W for unrestricted channels.

Hooft (1974) developed a formula to predict bow squat by combining Tuck's (1966) separate formulations for squat from sinkage and trim in unrestricted channels as in Equation 64.

$$S_b = 1.96 \frac{\nabla}{L^2} \frac{Fn_h^2}{\sqrt{1-Fn_h^2}} \tag{64}$$

where ∇ is the volumetric displacement.

ICORELS (1980), predicted a bow squat formula similar to Hooft's formula, as given by Equation 65.

$$S_b = 2.4 \frac{\nabla}{L^2} \frac{Fn_h^2}{\sqrt{1-Fn_h^2}} \tag{65}$$

Millward (1990) conducted physical model tests with towed models for several different ship types in unrestricted channels and he tested his models for a limited range of ship lengths, which tends to make his squat predictions of limited use for the newer and longer vessels. Millward (1992) rearranged his test results and presented a formula to predict bow squat as given by Equation 66.

$$S_b = 0.001L(61.7C_b \frac{1}{L/B} - 0.6) \frac{Fn_h^2}{\sqrt{1-0.9Fn_h^2}} \tag{66}$$

Römisch et al. (1989) conducted a physical model experiments for all three channel configurations to predict a formula for both bow and stern squat. His predicted values for bow S_b and stern squat S_S are given by:

$$S_b = C_V C_F K_T T \tag{67}$$

$$S_s = C_V K_T T \tag{68}$$

where C_V is a correction factor for ship speed, C_F is a correction factor for ship shape, and K_T is a correction factor for squat at ship critical speed.

$$C_V = 8\left(\frac{V}{V_{CR}}\right)^2 \left[\left(\left(\frac{V}{V_{CR}} - 0.5\right)^4 + 0.0625\right)\right] \tag{69}$$

where V_{CR} is ship's critical speed based on the channel configuration.

$V_{CR} = CK_{ch}$ for unrestricted (70)

$V_{CR} = CK_C$ for restricted (71)

$V_{CR} = C_{mT}\left[K_{ch}\left(1 - \frac{h_m}{h} + K_c\left(\frac{h_m}{h}\right)\right)\right]$ for canal (72)

where *C* is wave celerity based on the water depth h, C_{mT} is a wave celerity based on the relevant water depth h_{mT} and the mean water depth h_m, K_C is a correction factor on critical speed for a canal, and K_{Ch} is a correction factor on critical speed for a restricted and unrestricted channel.

$C = \sqrt{gh}$ (73)

$C_{mT} = \sqrt{gh_{mT}}$ (74)

$h_{mT} = h - \frac{h_m}{h}(h - h_m)$ (75)

$h_m = \frac{A_c}{W_{Top}}$ (76)

where W_{Top} is projected channel width at the water surface.

$W_{Top} = W + 2nh$ (77)

where *n* is inverse bank slope.

$K_c = 0.2306log\left(\frac{1}{S}\right) + 0.0447$ (73)

$K_{ch} = 0.58\left[\left(\frac{h}{T}\right)\left(\frac{L}{B}\right)\right]^{0.125}$ (78)

where *L* is the length between perpendicular and *B* is ship beam amidships.

$C_F = \left(\frac{10C_b}{L/B}\right)^2$ (79)

where the value of C_F is equal to 1.0 for the stern squat and C_b is the block coefficient.

$K_T = 0.155\sqrt{h/T}$ (80)

Ankudinov et al. (1996) proposed a formula for maximum squat based on S_{mid} and trim in shallow water. The restriction $Fn_h \leq 0.6$ is applied. The maximum ship squat, S_{Max}, is a function of S_{mid} and trim given by the S_{Max} can be at the bow or stern depending on the value of trim. The negative sign is used for bow squat S_b, and the positive sign for stern squat S_s as in Equation 81.

$$S_{Max} = L_{pp}(S_{mid} \pm 0.5Trim) \tag{81}$$

Ankudinov et al., (1996) proposed a formula for midship sinkage for $Fn_h \leq 0.6$, as given by Equation 82.

$$S_{mid} = (1 + K_P^S)P_{Hu}P_{Fn_h}P_{+h/T}P_{Ch1} \tag{82}$$

where K_P^S is the propeller parameter is defined as 0.15 for ships with single propellers and 0.13 for ships with twin propeller.

where P_{Hu} is the ship hull parameter for shallow water is defined as:

$$P_{Hu} = 1.7C_B\left(\frac{BT}{L_{PP}^2}\right) + 0.004C_B^2 \tag{83}$$

P_{Fn_h} is the ship forward speed parameter, is given by:

$$P_{Fn_h} = Fn_h^{1.8+0.4Fn_h} \tag{84}$$

where $P_{+h/T}$ is the water depth effects parameter is defined as

$$P_{+h/T} = 01 + \frac{0.35}{(h/T)^2} \tag{85}$$

P_{Ch1} is the channel effects parameter for an R or C configuration is defined as:

$$P_{Ch1} = 1 + 10S_h - 1.5(1 + S_h)\sqrt{S_h} \tag{86}$$

where S_h is water depth factor as shown in Equation 87.

$$S_h = C_B\left(\frac{S}{h/T}\right)\left(\frac{h_T}{h}\right) \tag{87}$$

where h_T is the trench height measured from the bottom and *S* is the blockage factor.

$$S = \frac{A_S}{A_c} \tag{88}$$

Ankudinov et al. (1996) proposed a formula to trim prediction as given by Equation 89.

$$Trim = -1.7P_{Hu}P_{Fd}P_{h/T}K_{Tr}P_{Ch2} \quad (89)$$

where P_{Ch2} is the trim correction parameter an R or C configuration is defined as:

$$P_{Ch2} = 1 - 5S_h \quad (90)$$

where K_{Tr} is the trim coefficient is defined as:

$$K_{Tr} = C_B^{nTr} - (0.15K_P^S + K_P^T) - (K_B^T + K_{Tr}^T + K_{T1}^T) \quad (91)$$

where n_{Tr} is the trim exponent is defined as:

$$n_{TR} = 2 + 0.8P_{Ch1}/C_B \quad (92)$$

where K_P^T is the propeller parameter is defined as 0.15 for ships with single propeller and 0.2 for ships with twin propellers, K_B^T is the bulbous bow parameter is defined as 0.1 for ships with bulbous bows and 0 for ships without bulbous bows, K_{Tr}^T is the stern transom parameter which is 0.04 for ships with a stern transom and 0 for ships without a stern transom, K_{T1}^T is the initial trim factor as defined in Equation 83.

$$K_{T1}^T = \frac{T_{ap} - T_{fp}}{T_{ap} + T_{fp}} \quad (93)$$

where T_{ap} is the static draft at the stern or aft perpendicular and T_{fp} is the static draft at the bow or forward perpendicular.

Yoshimura (1986) proposed a formula for bow squat for a U, R and C configuration is given by:

$$S_b = \frac{\left[\left(0.7 + \frac{1.5T}{h}\right)\left(\frac{BC_b}{L}\right) + \frac{15T}{h}\left(\frac{BC_b}{L}\right)^3\right]V_e^2}{g} \quad (94)$$

where $g = 9.81 m/s$ and V_e is the enhanced ship speed term is defined as:

$$V_e = \frac{V_S}{1 - S} \quad (95)$$

where V_S is the ship speed.

The range of applicability for each empirical formula is given in Table 12. Here, several empirical formulae do not have any constraints. This is a consequence of the derivation used by the respective authors, rather than an indication of uniform applicability.

Table 12. Empirical formulae constraints, adopted from Briggs (2006).

Formula	Constrains				Configuration		
	C_b	h/T	L/h	Fn_h	U	R	C
Barrass (1981)	0.5 to 0.9	1.1 to 1.5			✓	✓	✓
Eryuzlu and Hausser (1978)	≥0.8	1.08 to 2.75			✓	✓	
Eryuzlu and Hausser (1978)	≥0.8				✓		
Hooft (1974)					✓		
ICORELS (1980)					✓		
Millward (1990)	0.44 to 0.83		6 to 12		✓		
Millward (1992)			6 to 12		✓		
Norrbin (1986)					✓		
Römisch et al. (1981)		1.19 to 2.25			✓	✓	✓
Ankudinov et al. (1996)*				≤0.6	✓	✓	✓
Yoshimura (1988); Ohtsu et al. (2006)					✓	✓	✓

* Trim, midship sinkage coefficient and squat

5.2.4. Slender body theory

The slender body theory is one of the most successful approaches to computing shallow water trim and sinkage. This is particularly true in the low speed range, because viscous effects play a secondary role (Dand, 1967). The aforementioned theory, utilising a velocity potential function, renders it unable to compute viscous contributions. As such, low speeds and moderate depths are well-suited for predictions using the slender body theory. In the present chapter, an in-house code which solves the equations of Tuck (1966), Tuck (1967), and Beck et al. (1975) will be used. The debut of the code was presented in Terziev et al. (2019a) for dredged channels and canals. The equations used

in the code will be presented in this study, can be found in the open literature (Beck et al., 1975; Terziev et al., 2018; Tuck, 1967a, 1966). Suffice to say the integration of highly oscillatory integrals, representing the Fourier transform of the ship's cross-sectional area and beam (Gourlay, 2014; Tuck, 1967b) is avoided by using the convolution form of the governing equations (Tuck, 1967a, 1966). This is done because, as stated by Gourlay (2014), the convolution form of the equations is favourable for practical applications. The input data for KCS, as modelled for the slender body theory is shown in Figure 58 using a scale factor of 1:75. The principal characteristics of the ship are shown in Section 3.2.2.

The theory begins by supposing that the flow is two dimensional, and satisfies Laplace's equation:

$$(1 - Fn_h)\frac{\partial^2 \varphi}{\partial x^2} + \frac{\partial^2 \varphi}{\partial y^2} = 0 \quad (96)$$

where φ is used to denote the velocity potential. For the cases examined here (subcritical speeds), the solutions of the above equation are elliptical. The boundary conditions are a critical component of the theory. The hull is described by:

$$\frac{\partial(x+\varphi)}{\partial n} = 0 \quad (97)$$

where ∂ / ∂n is the derivative in the normal direction. This also holds for the seabed. To satisfy mass conservation, Tuck (1966) arrived at:

$$\frac{\partial \varphi}{\partial x} = \pm \frac{V}{2h_0} S'(x) \text{ at } y = 0 \text{ i.e. at the hull} \quad (98)$$

where S(x) is the hull cross-sectional area at position x, and prime is used to denote the derivative dS/dx, h_0 is the interior water region depth, and V is the ship speed. The remaining boundary conditions are that the velocity potential must vanish at an infinite distance from the ship. To account for a change in depth, which characterises a dredged channel, Beck et al. (1975) split the flow into interior and exterior regions based on the depth:

$$h(y)\begin{cases} h_o, & |y| < w/2 \\ h_\infty, & |y| > w/2 \end{cases} \quad (99)$$

where *w* is the width of the interior region. Splitting the domain thus creates two different flow regimes. The interior is characterised by the depth h_0 and resulting interior depth Froude number $F_0 = V/\sqrt{h_0 g}$, and exterior depth Froude number $F_\infty = V/\sqrt{h_\infty g}$.

The solution proceeds by defining the function k(x) and θ as follows:

$$\mathrm{k(x)} = \left[\coth\frac{\pi \mathrm{x}}{\mathrm{w}\sqrt{1-\mathrm{F}_0^2}} - 1\right]\exp\left(\frac{2\theta \mathrm{w}}{\mathrm{w}\sqrt{1-\mathrm{F}_0^2}}\right) \tag{100}$$

$$\theta = \begin{cases} \arctan\left(\dfrac{\mathrm{h}_\infty\sqrt{\mathrm{F}_\infty^2-1}}{\mathrm{h}_0\sqrt{1-\mathrm{F}_0^2}}\right) \text{ for } \mathrm{F}_\infty < 1 \\ \mathrm{i}\times \mathrm{sgn(k)}\arctan\left(\dfrac{\mathrm{h}_\infty\sqrt{1-\mathrm{F}_\infty^2}}{\mathrm{h}_0\sqrt{1-\mathrm{F}_0^2}}\right) \text{ for } \mathrm{F}_\infty > 1 \end{cases} \tag{101}$$

where $i = \sqrt{-1}$ and $sgn(k)$ is the signum of the Fourier transform variable k.

The only change between the open shallow water, dredged channel and canal cases are expresed by the θ parameter and the ratio h_0/h_∞. When $\theta = 0$, the above relationships reduce to the canal case-studies. Whereas when $h_0/h_\infty = 1$, the relationships reduce to their the open water variants (Beck et al., 1975).

The next step is to calculate the force and moment coefficients:

$$C_f = \frac{\int b(x) \neg\!\!\!f s'(\xi) k(x-\xi) d\xi dx}{2wL\sqrt{1-F_0^2}\int b(x)dx} \tag{102}$$

$$\mathrm{C_m} = \frac{\int \mathrm{xb(x)} \neg\!\!\!f \mathrm{s'(\xi)k(x-\xi)d\xi dx}}{2\mathrm{wL}\sqrt{1-\mathrm{F}_0^2}\int \mathrm{b(x)x^2 dx}} \tag{103}$$

where $\neg\!\!\!f s'(\xi)k(x-\xi)d\xi dx$ is the convolution mentioned previously, $\neg\!\!\!f$ is used to denote the Cauchy or principle value integral and ξ is the convolution variable.

Once these are obtained, the solution requires the definition of two shape parameters, α and β (Eq. (104) and Eq. (105), which are used to predict the sinkage (C_S) and trim (C_ϑ) coefficients, as demonstrated in Eq. (106) and Eq. (107), respectively.

$$\alpha = \frac{\int xb(x)dx}{L\int b(x)x^2dx} \quad (104)$$

$$\beta = \frac{L\int b(x)xdx}{\int b(x)x^2dx} \quad (105)$$

$$C_S = \frac{C_f - \alpha C_m}{1-\alpha\beta} \quad (106)$$

$$C_\vartheta = \frac{C_m - \beta C_f}{1-\alpha\beta} \quad (107)$$

Once these parameters have been obtained, the sinkage (s) and trim (t) can be calculated:

$$s = \frac{LC_S F_0^2}{\sqrt{1-F_0^2}}\ [m] \quad (108)$$

$$t = \frac{C_\vartheta F_0^2}{\sqrt{1-F_0^2}}\ [radians] \quad (109)$$

In order to predict the parameters of interest in the modelled Suez Canal, the sloped shape is transformed into a rectangular cross-section with equal depth and blockage ratio (Gourlay, 2008). This process is depicted in Figure 57a for the Suez Canal. The equivalent canal is characterised by a depth of 0.32m, and width equal to 2.89m. Then, the application of the abovementioned equations for a canal of constant width and depth are straightforward. This study will serve as a validation of the in-house code. For reference, the rectangular canal is modelled as depicted in Figure 57b.

a

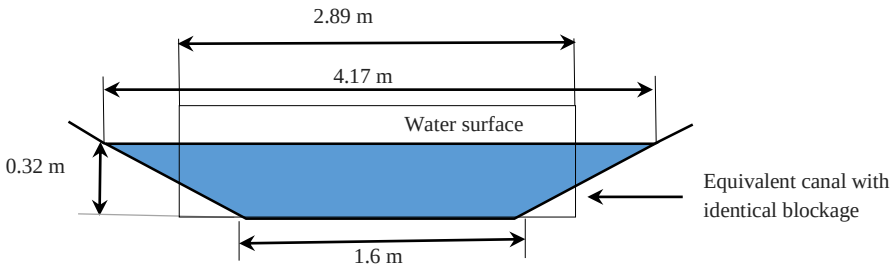

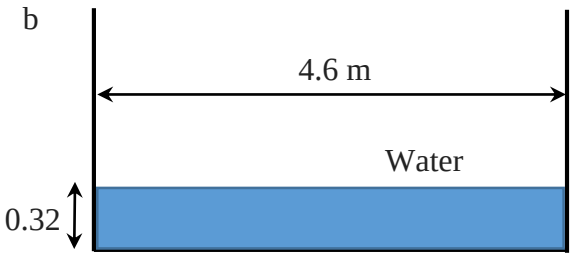

Figure 57. Case-studies: a – Suez Canal case-study, b – rectangular canal

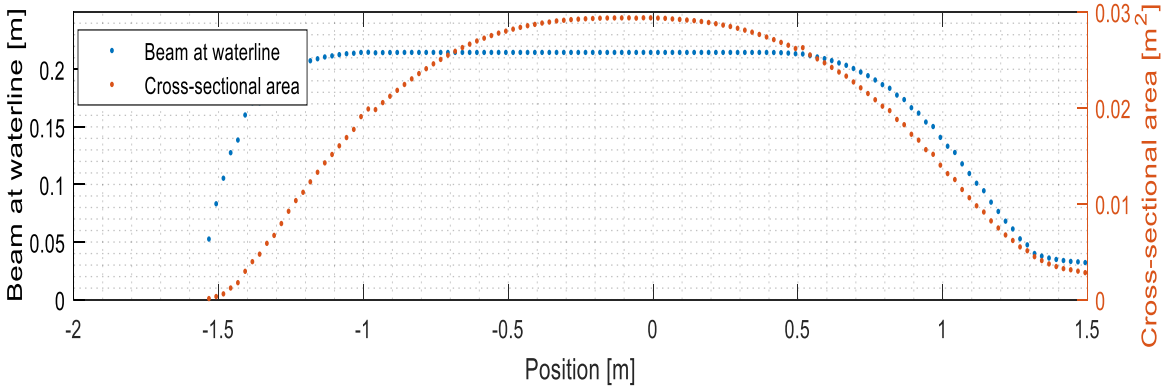

Figure 58. KCS ship model input for slender body calculations

Several researchers have attempted to improve on the predictions of the slender body theory. Most notably, Gotman (2002) and Lazauskas (2009). The former decomposed the monotone and oscillatory parts of Michell's (1898) integral. This allowed her to incorporate viscous effects and achieve great improvement in predictions. Lazauskas (2009) split the space around the ship hull into different parts, and established formulae to account for the viscous-dominated regions in the immediate vicinity of the ship. This was accomplished by utilising the 'equivalent' shape of the ship, which is the underwater ship hull, plus the thickness of the boundary layer. Since no software are available, capable of modelling either of the abovementioned improved integrals, author is confined to the more classical versions of the slender body theory. The fact that researchers in the field of mathematics have driven the development of the slender body theory restricts the ability of engineers to use it independently. This is especially true in the absence of black box style tools, such as RANS solvers, where the user is not required to understand in detail the underlying algorithms.

Research has been carried out to resolve one of the physically unsound problems of the slender body theory: the prediction of a singularity at the critical speed. Lea and Feldman

(1972) modified the underling equations, arriving at a nonlinear solution. Preserving the linear form of the equations, Gourlay and Tuck (2001) presented a trans-critical form of the slender body theory. Mei and Choi (1987), presented a solution to the problem of a ship sailing in shallow water, and later improved on their work to account for the critical speed (Alam and Mei, 2008; Mei and Choi, 1987). More recent contributions include Deng et al., (2014), Z. hong Zhang et al., (2017), and Zhang et al., (2015), who developed, and subsequently expanded on a slender body-based analytical formulation to calculate the pressure field, generated by a ship advancing in subcritical and supercritical speeds, which also include non-linear and dispersive effects. The techniques mentioned in above have only been applied to simple geometries, such as stepped or parabolic hulls. Their validity has yet to be demonstrated to real ship hulls. Coupling this with their mathematical complexity has meant that they are omitted in the assessments performed here.

5.3 Results and discussion

In the following section, the results for both case-studies are presented. To facilitate comparison and discussion, the data from all methods are presented jointly for each case-study.

5.3.1. Ship Sinkage and trim

As mentioned previously, sinkage and trim are of great practical importance in restricted waters (Ferguson, 1977). While it is well-known that smaller canal cross-sectional area causes greater ship squat, the manner in which this occurs requires further investigation. The results shown jointly in Figure 59 and Figure 60 demonstrate that the present CFD model agrees well with experimental observations in the rectangular canal. Moreover, the assertion that the CFD model will have a tendency to provide a small negative error is validated for the entire speed range for sinkage in this case-study. In terms of trim, the CFD model has also performed well, predicting values within a reasonable margin. The slender body theory is shown to perform better for trim than for sinkage, as measured at

the ship centre of gravity. In any case, the results compare well for low speeds, which is where the slender body theory's strengths lie (Tuck and Taylor, 1970). The apparent disagreement in sinkage for very low speeds is exhibited due to the difficulties in measuring displacements smaller than 2 mm experimentally (Elsherbiny et al., 2019b).

For the rectangular canal, the examined speeds range from 0.1 to 0.57 depth Froude numbers. Although the high speed range is unlikely to occur in practice, it is interesting to note that the disagreements between the CFD and EFD curves in sinkage increase with velocity. On the other hand, the differences in trim remain relatively constant. This implies that sinkage is more difficult to predict that trim using the present CFD model. It is important to keep in mind the experimental uncertainty and its effect on the predicted values. It is important to observe that in the region of practical interest (depth Froude numbers smaller than 0.3), the two sets of data agree well.

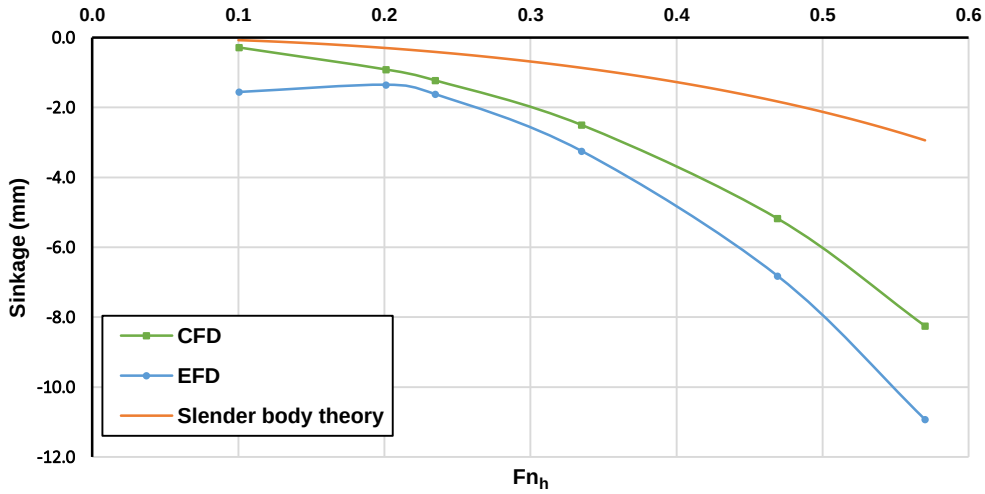

Figure 59. Sinkage for the rectangular canal

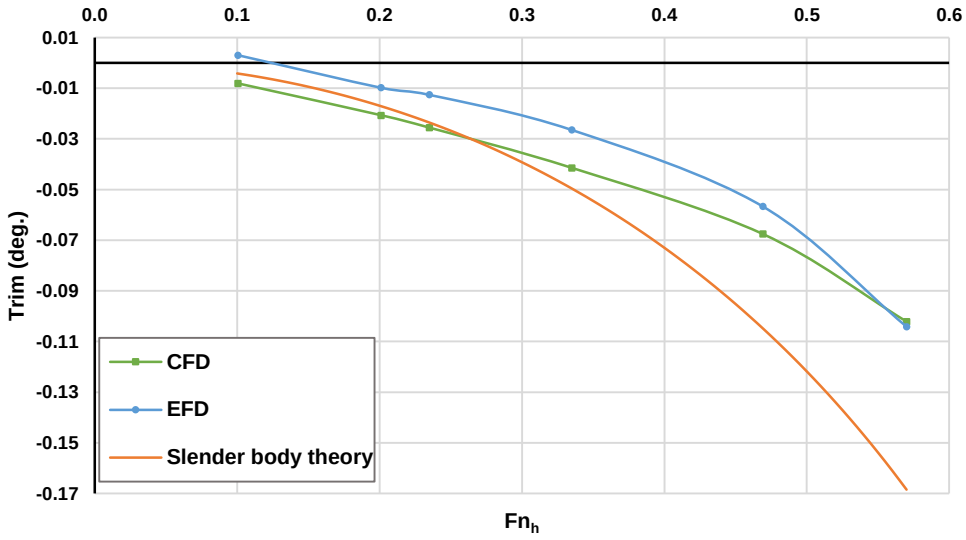

Figure 60. Trim for the rectangular canal

For the Suez Canal, EFD and CFD simulations up to an equivalent of 9 knots in full-scale, which translates to depth Froude numbers between 0.1 to 0.33. This choice is made because the maximum operational speed allowed in the Suez Canal is 7 knots (Suez Canal Authority, 2019b). While it is interesting to examine higher speeds for the present case, they cannot occur in practice due to legal restrictions. The current legal restrictions limit the allowable speed, which restricts the number of vessels per year to approximately 18 000. Therefore, the present investigation focuses on practically relevant operational speeds in the Suez Canal. Additionally, Elsherbiny et al. (2019b) demonstrated experimentally that a change in h/T values within the abovementioned depth Froude number range does not have a significant impact. For this reason, the present study focuses on h/T=2.2 (full-scale depth = 24 m) as a representative case, which translates into the actual full-scale depth of the Suez Canal.

Figure 61 and Figure 62 jointly present the sinkage and trim values obtained for the Suez Canal via CFD, EFD and the slender body theory. The figures indicate that the present CFD model, whose physical modelling characteristics have been carried from the previous case-study, performs adequately in the case of trim. Sinkage once again proves more difficult to accurately estimate. However, the differences between CFD and EFD are smaller than those exhibited by the slender body curves. This may stem from

assumption that the sloped canal is equivalent to a rectangular canal with equal blockage. More research in this direction is left as future piece of work.

The slope and shape of the slender body curves are governed by several parameters. These include the depth and width of the canal, as well as the shape of the vessel. Additionally, as the depth Froude number approaches unity, a singularity is predicted (Gourlay and Tuck, 2001). In other words, the slope of the slender body prediction will increase until the critical depth Froude number is reached, where it will attain an infinite value. This is not predicted experimentally or numerically (Elsherbiny et al., 2019b; Terziev et al., 2018), which restricts the applicability of the slender body theory to low speeds.

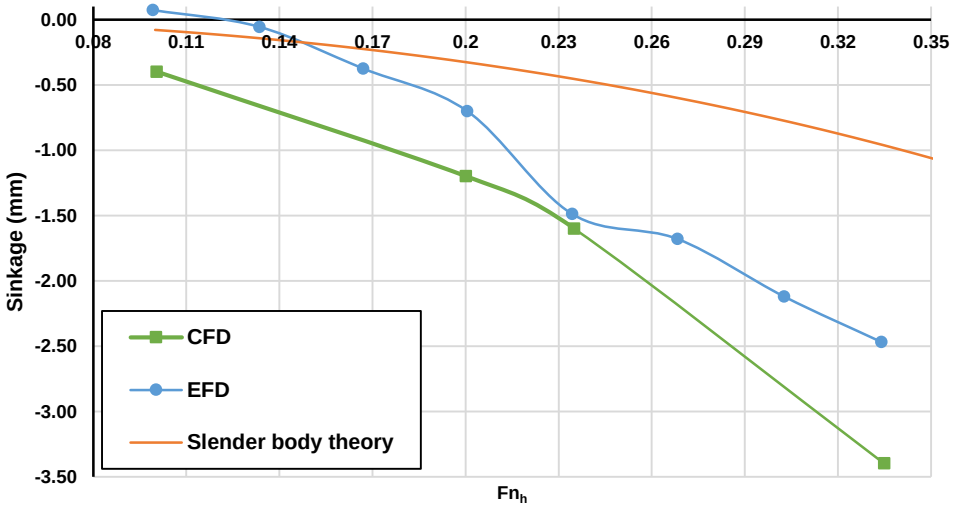

Figure 61. Sinkage for the Suez Canal

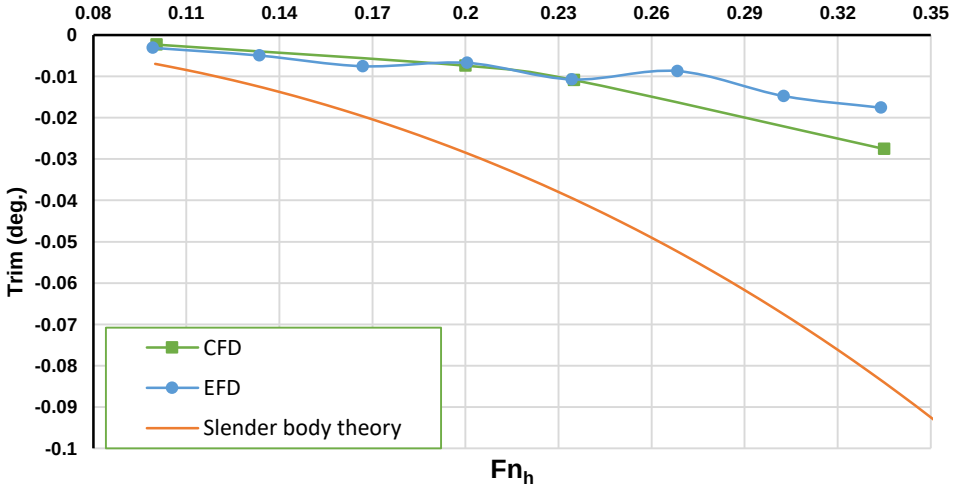

Figure 62. Trim for the Suez Canal

Figure 63 presents a comparison of the measured sinkage values versus the numerical predictions for all case-studies. An apparent pattern, emerging from this figure is that CFD predicts gradual changes in sinkage with the increase of speed. The experimental results show oscillations at certain speeds in the displacement of the centre of gravity of the ship, specifically at $F_h = 0.23$ for the Suez Canal. Coincidently, this dip in the measured sinkage matches the numerically predicted sinkage almost exactly. However, once the dip in measured sinkage has been overcome, the apparent difference between the two sets of data begins to increase anew.

An additional observation, made from Figure 63 is that in the rectangular canal case-study, the CFD model underpredicts the sinkage. However, the behaviour of the numerically predicted values for this parameter are overpredicted in the case of the Suez Canal. This pattern makes the predictions for the Suez Canal match the measured sinkage in the rectangular canal. Conversely, the measured sinkage values in the rectangular canal seem to lie close the Suez Canal, especially in the high speed range. The source of these disagreements is not known. However, one may speculate that a combination of uncertainty, both experimental and numerical, superimposed onto the choices pertaining to the numerics of the CFD model are the source of the disagreements observed above. RANS solutions contain many sources of error, stemming from sources as diverse as boundary conditions, levels of inlet turbulence, iterative and discretisation errors, convection scheme, etc. (Eca et al., 2013; Roy, 2005; Xing and Stern, 2010). Separating each of these components and assessing their impact (when possible) on different aspects of the numerical solution is an ongoing field of research (Eca et al., 2017).

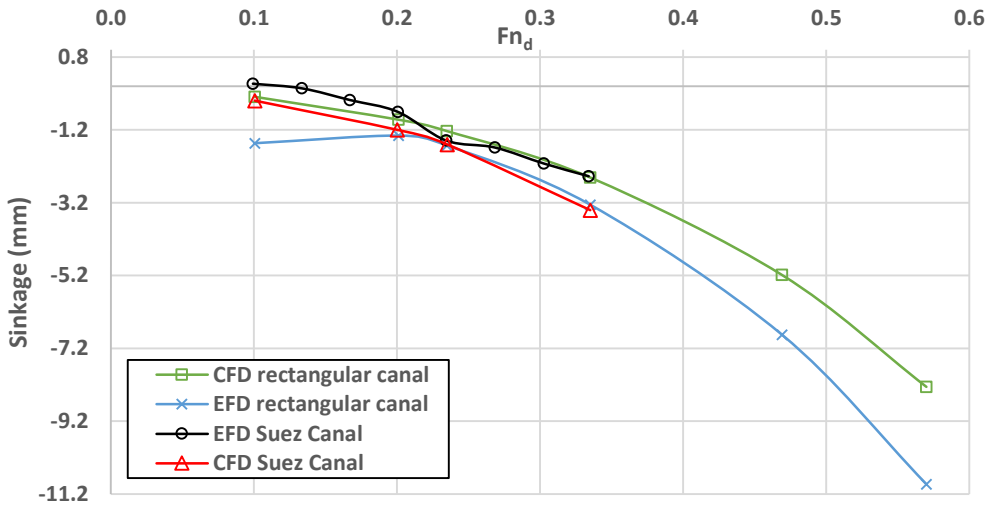

Figure 63. CFD and EFD comparison of sinkage at the ship's centre of gravity for all case-studies

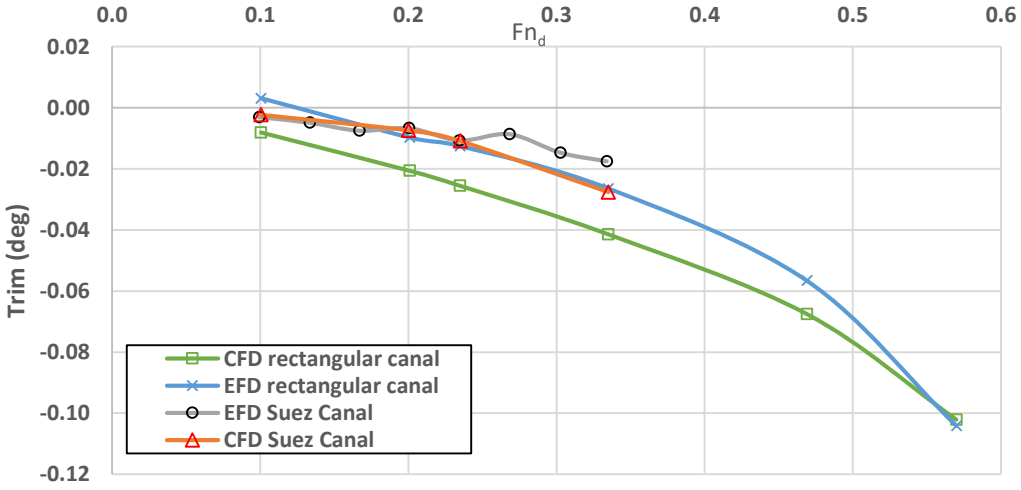

Figure 64. CFD and EFD comparison of ship trim.

The trim predictions, shown in Figure 64 exhibit a different pattern than the sinkage (Figure 63). Although an agreement is observed in the low speed range, the trend is not continued past $F_h = 0.235$ for the Suez Canal. The EFD data for trim show the oscillatory patterns discussed previously, whereas the CFD predictions follow a smooth path. The two sets of data in the case of the rectangular canal show better agreement in terms of trend, but not in the exact location along the y – axis. Instead, the CFD method shows a systematic underprediction. However, due to the sharp decline in the EFD curve, the two sets of data almost coincide for the highest speed examined. That is, although this

particular point on the graph ($F_h = 0.57$) is unlikely to occur in practice. The sources of error, discussed in the case of sinkage, carry forward to trim as well. In fact, it is well known that the two parameters (jointly forming ship squat) are intrinsically linked (Shivachev et al., 2017).

Figure 65 depicts a comparison of different empirical models for both case-studies. In the figure, how the different models compare to each other for the same case have been plotted, as well as across case-studies. These reveal that formulae, containing higher powers of the speed, tend to massively overpredict values in the high speed range. For instance, Römisch (1989) contains more terms involving higher powers of the speed than the remaining empirical formulae examined in Figure 65 (Briggs et al., 2009). The empirical formulae used can be found in the Appendix.

Out of all empirical models compared in Figure 65, only the one due to Ankudinov (whose mathematical basis is explained in detail Briggs (2009) and Briggs and Daggett (2009)), is capable of predicting whether a ship will squat by stern or by bow. Unfortunately, both CFD and EFD methods show that the ship will squat by bow, rather than by stern, which is the prediction made by the abovementioned method. This highlights the need for accurate tools even in the early design stage. This particular formulation predicts virtually identical squat for both case-studies, which make it difficult to distinguish the two curves in Figure 65. The empirical equations are not compared with the previous method because the empirical formulae calculate the squat which is function of sinkage and trim.

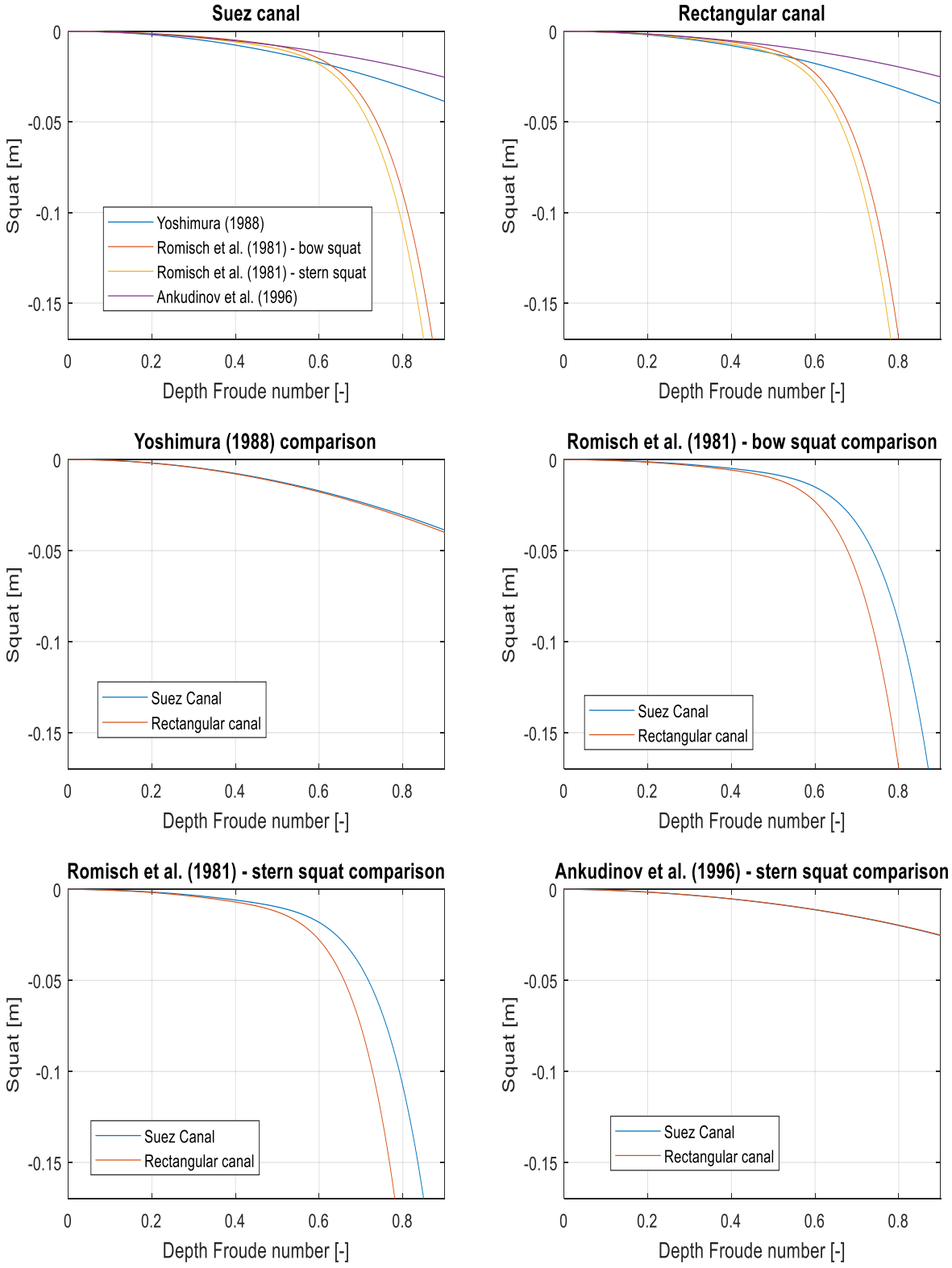

Figure 65. Empirical methods comparison for both case-studies.

5.3.2. Resistance

This section examines the resistance values computed via CFD, EFD and their respective decompositions into constituent components. The discussion begins with the total resistance comparison to establish relative differences between the predicted and measured values.

Over the entire speed range examined for the rectangular canal, the CFD model compares well with the EFD data, as shown in Figure 66. The calculated values show a small underprediction over the majority of the speeds, validating the assertion relating to turbulence modelling. The k – ω turbulence model is therefore proven as a good choice for examinations focusing on towed calm shallow water predictions. The resistance values are shown to grow in a quadratic manner with speed, as expected. When comparing these to the Suez Canal, it is evident that the CFD model does not have a clear tendency to over- or underpredict the EFD data, shown in Figure 67. This is in all likelihood due to the complex nature of the problem.

The CFD method requires the accurate resolution of the free surface to predict the pressure component of resistance. In the rectangular canal this is straightforward. However, the Suez Canal's bathymetry is characterised by a slope, which terminates with an intersection of the water surface. As the waves, shed from the bow approach the bank, they slow down, grow in height and change direction (Lamb, 1932). The manner in which they interact with the bathymetry is not limited to the above. A part of the waves will also reflect back onto the ship upon reaching the beginning of slope, interacting with the hull. Now, the speeds examined for the Suez Canal are low, rendering the waves largely inconsequential near $Fn_h = 0.1$. However, as shown in Figure 68, even for a depth Froude number as low as 0.33, the generated disturbance is substantial. The interaction between the ship and the waves, shed from its bow and stern are significant, making this a highly unsteady case.

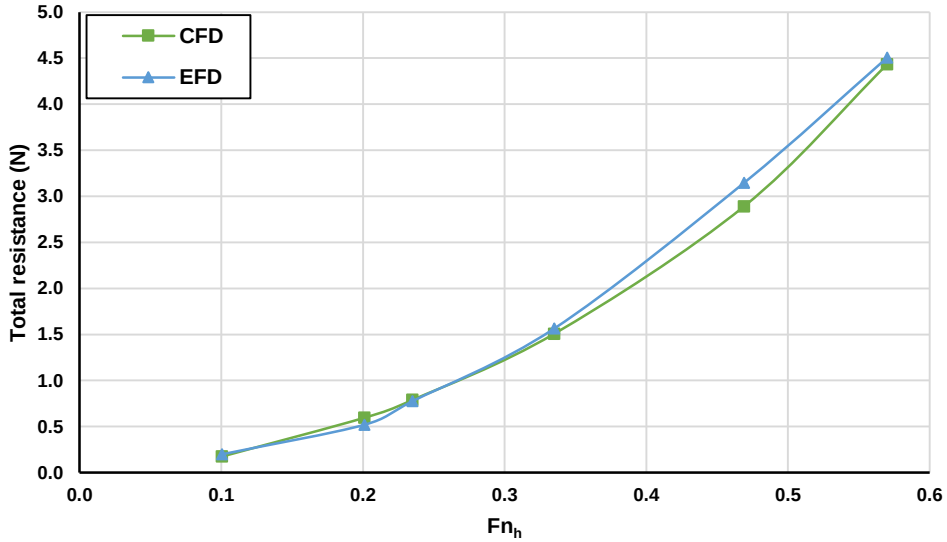

Figure 66. EFD and CFD of total resistance for the rectangular canal

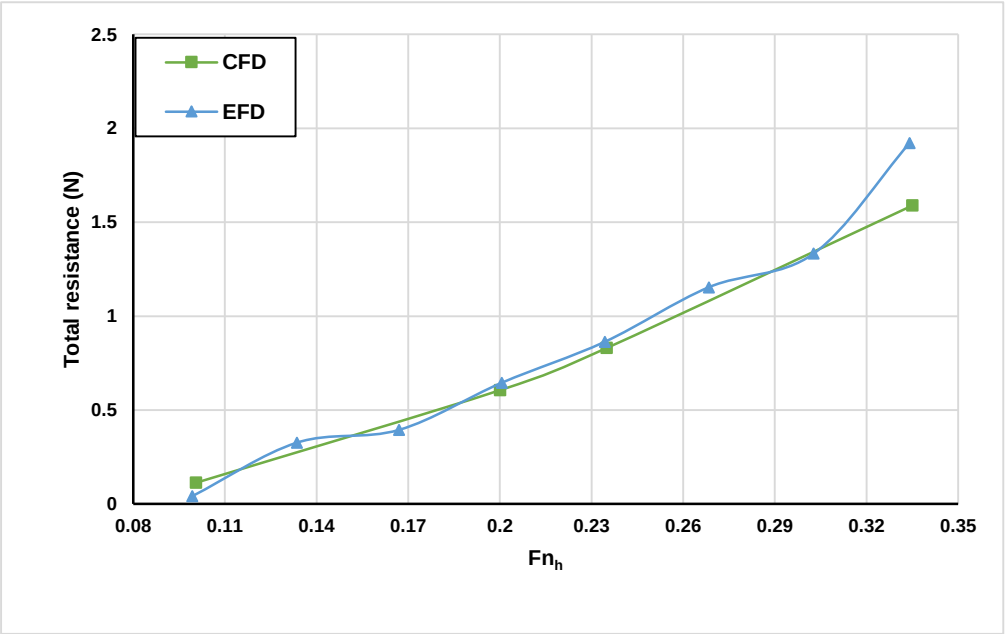

Figure 67. EFD and CFD of total resistance for the Suez Canal

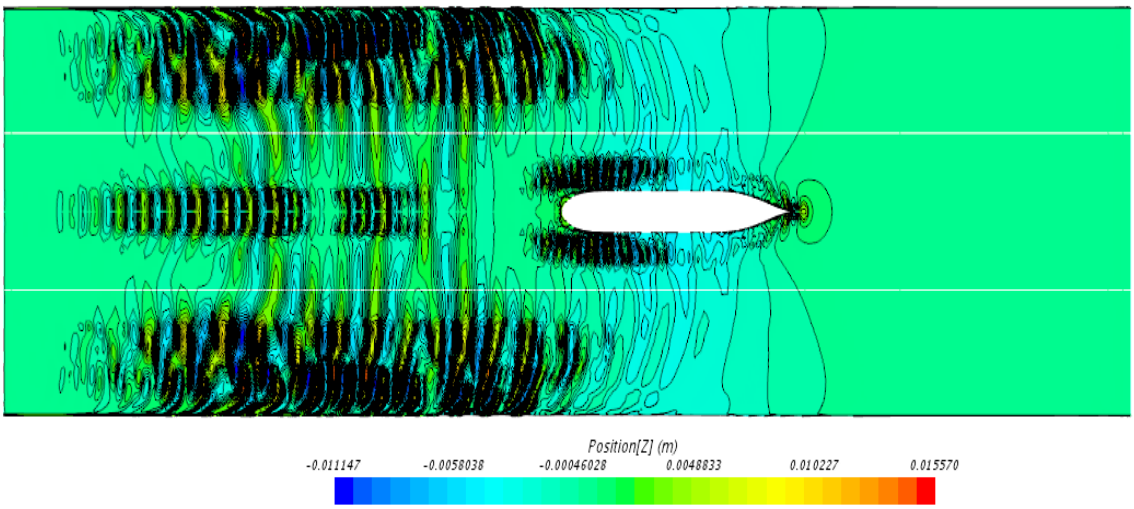

Figure 68. Generated wave patterns in the Suez Canal for $Fr = 0.33$. Mirrored about the central plane

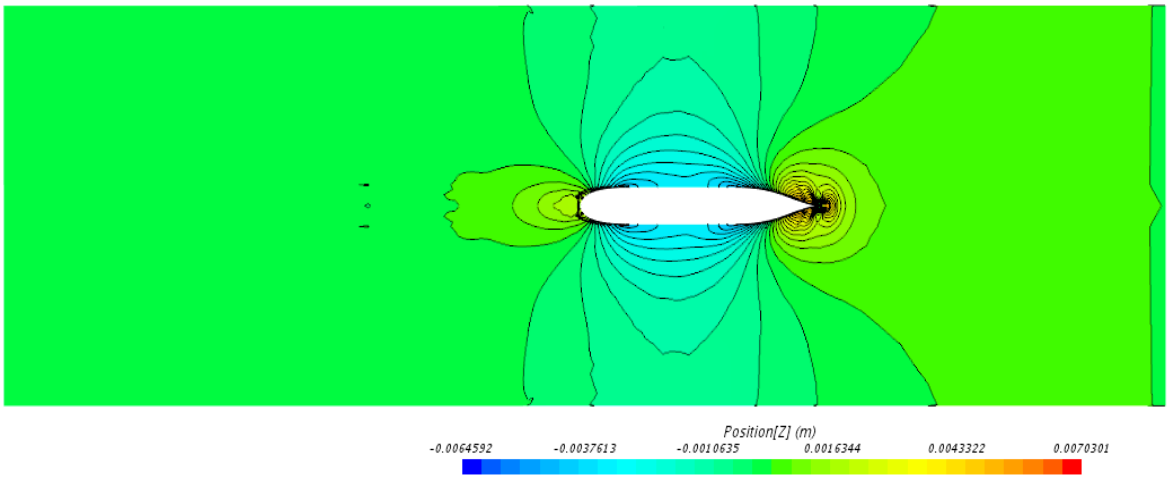

Figure 69. Free surface disturbance, generated in the rectangular canal at $Fr = 0.33$

In Figure 68, the projection of the beginning of the slope onto the free surface (white lines) have been included to enable a better understanding of the underlying phenomena. In particular, it seems that the seabed immediately after the beginning of the slope does not interact strongly with the waves. This is in line with theoretical predictions, which dictate that the effect on the wave pattern depends on the transition in depth. The large waves, appearing with increasing distance from the ship centreline seem to decompose into smaller components with larger wave heights. According to Newman (1965), the energy within waves vanishes at a rate, proportional to the water depth, and wave heights increase accordingly. This is clearly observed in Figure 68, especially near the banks. No wave breaking is identified in the present case near the lateral extremities of the domain.

However, such phenomena may be expected to occur and be visible if the ship speed were to be increased.

It is important to keep in mind that shallow water waves propagate at a speed of $\sqrt{gh}$. This explains the observed curve in the shape of the waves as the bank is approached. The propagation speed diminishes with distance from the ship and the waves fall behind (towards the outlet) at a greater rate than the remaining wave system. The rectangular canal free surface disturbance for the same depth Froude number is shown in Figure 69 for comparison. Here, the ship generates a near-field disturbance only. This is likely due to the low depth Froude number, coupled with the proximity of the canal sides.

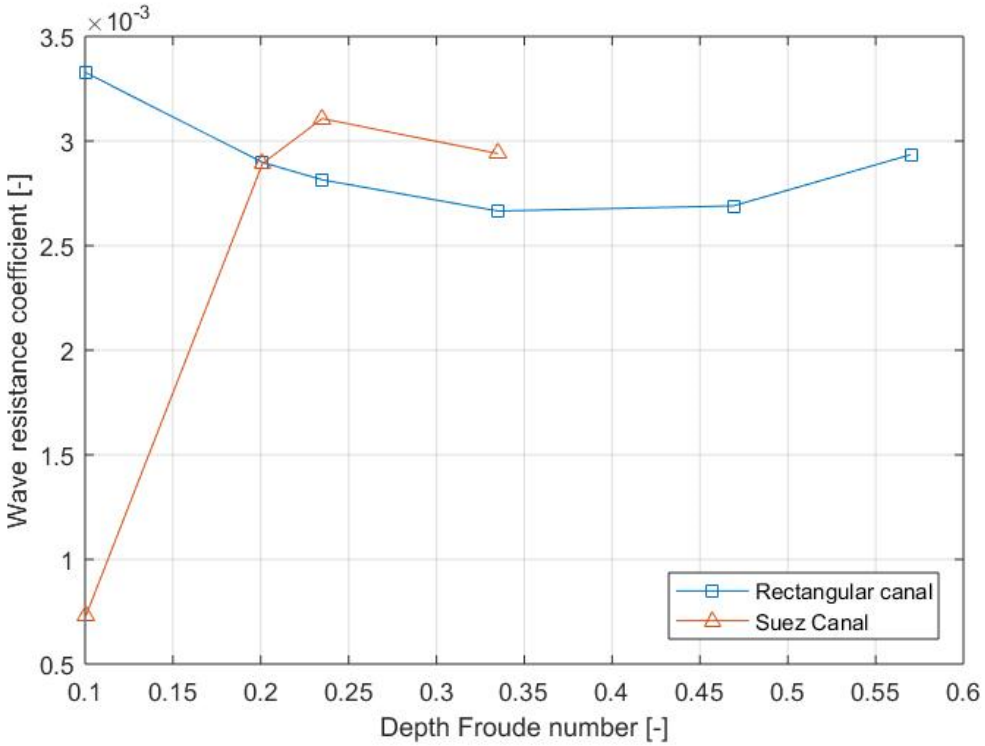

Figure 70. Calculated wave resistance coefficients for both case-studies using CFD

The generated wave patterns induce a wave resistance onto the ship. As explained in Section 4.2.1, in the present chapter the wave resistance coefficient is calculated by subtracting the multiphase total from the double body total resistance in CFD. In the rectangular canal, the predicted values show a smooth variation, characterised by an initial decrease, which recovers with increasing depth Froude number (shown in Figure 70). This pattern repeats in all likelihood as one progresses through the depth Froude

number range, causing the typical oscillatory pattern of wave resistance to emerge (Tuck and Lazauskas, 2008). The Suez Canal wave resistance on the other hand exhibits a sharp rise, following which, the pattern of the rectangular canal seems to be reproduced. This is not surprising, considering the wave disturbance observed in Figure 69. To elaborate, wave effects become more significant as speed is increased at a greater rate than in the rectangular canal.

The wave resistance coefficients presented in Figure 70 show similar behaviour to those experimentally estimated by Elsherbiny et al. (2019b). However, author's predictions are higher than those reported by the abovementioned authors. This can be explained by the choice of friction line, which during the experimental stage (in Elsherbiny et al. (2019b)) was the ITTC line (ITTC, 2017c). The impact of the choice of skin friction coefficient is illustrated in Figure 71. Namely, depending on which method to estimate the skin friction of the ship is chosen, the wave resistance may vary substantially, especially during the experimental stage, where there is no other choice but to calculate C_F via a friction line.

Another interesting property of the results presented herein is that in the rectangular canal, C_W does not show signs of decreasing even when the depth Froude number is as low as 0.1. The Suez Canal results on the other hand exhibit the aforementioned decline. Thus, the zero wave resistance assumption at low speeds may not be valid, depending on the underwater topology.

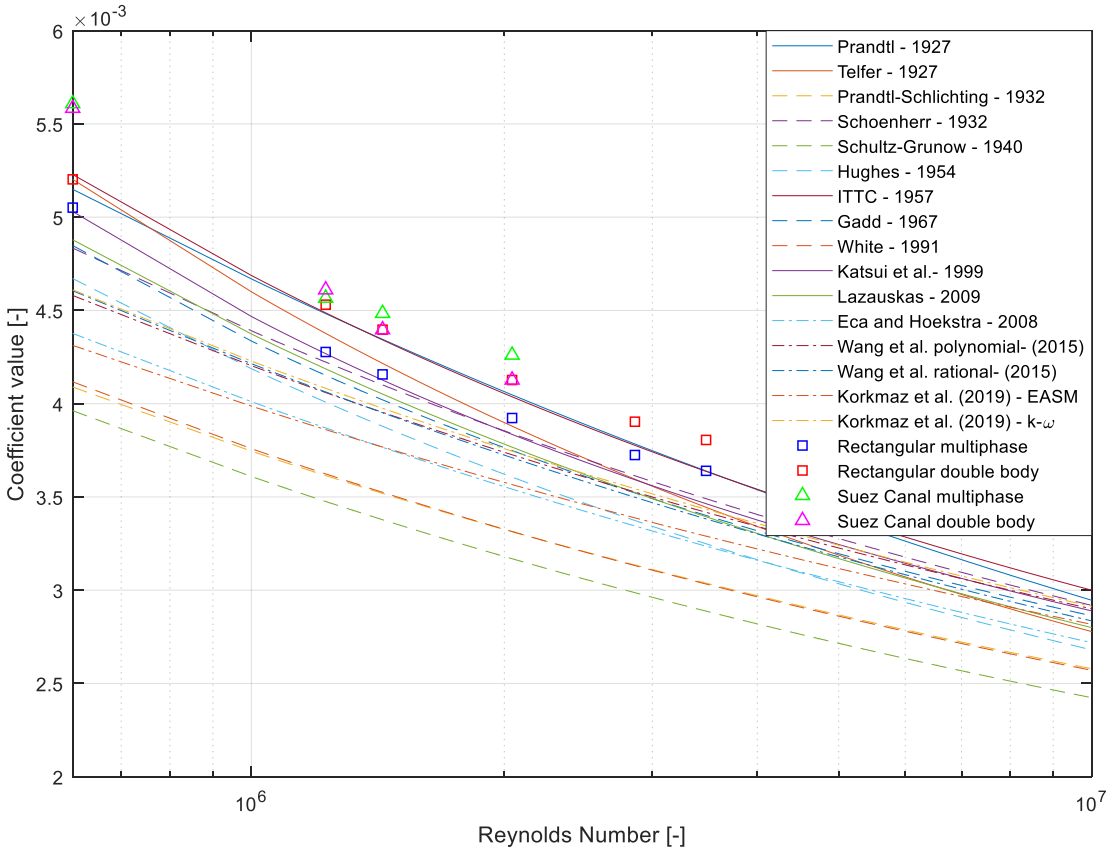

Figure 71. Frictional resistance coefficients for all case-studies (Eca and Hoekstra, 2008; Gadd, 1967; Hughes, 1954; ITTC, 2017c; Katsui et al., 2005; Korkmaz et al., 2019; Lazauskas, 2009; Prandtl, 1925; Schlichting, 1979; Schoenherr, 1932; Schultz-Grunow, 1941; Telfer, 1927; Wang et al., 2015; White, 2006)

In Figure 71, the double body and multiphase frictional resistance coefficients are presented graphically against Reynolds number. Several differences between the case-studies become immediately apparent. Firstly, contrary to the deep water cases of Terziev et al. (2019c), the frictional resistance coefficient in double body mode is higher, rather than lower than the multiphase case for the same Reynolds number in the rectangular canal. This has also been observed by the present authors in a recent work examining scale effects in shallow water (Terziev et al., 2019d).

The frictional resistance coefficients predicted for the Suez Canal exhibit a surprising feature. Namely, the double body predictions are either close to, or below the multiphase skin friction predictions. This implies that underwater bathymetry has a substantial effect on C_F. To further this argument, one may refer to the observed deviation between the

frictional predictions for the Suez and rectangular case-studies. Here, it is evident that a lateral restriction creates an increase in frictional resistance. Thus, the extension of the ITTC line for shallow waters proposed by Zeng et al. (2018), which corrects only the ship bottom, may not be applicable in the present case. In addition, the ship bottom must be maintained flat as part of the abovementioned authors' friction line, which was not done in this study. The difference between C_F for all cases shows signs of monotonic decline with increasing Reynolds number. This may suggest that free surface effects become negligible at higher speeds or scale factors. However, one must remember that in the resistance calculation process, the underwater area *and* speed are used to non-dimensionalise the resistance coefficients. Thus, an apparent decline in coefficient form could translate into an increase in dimensional resistance, depending on the case.

Figure 72 shows that the form factor behaves in a manner, opposite to the wave resistance for the Suez Canal. That is to say, (1+k) attains a high value of approximately 1.245 for a depth Froude number of 0.1. This is followed by a sharp decline, which brings the Suez Canal form factor in line with the rectangular canal. In fact, the difference between the two is vanishingly small for the highest depth Froude number examined in the present study. This suggests that, if one were to accept the present resistance decomposition methodology, three dimensional effects decrease in importance with increasing speed. It is also noted that the prediction made herein is virtually the same as in Elsherbiny et al. (2019b) for h/T=2.2. In fact, it seems that once a speed threshold is passed, the form factor ceases to vary and approaches the experimentally determined value.

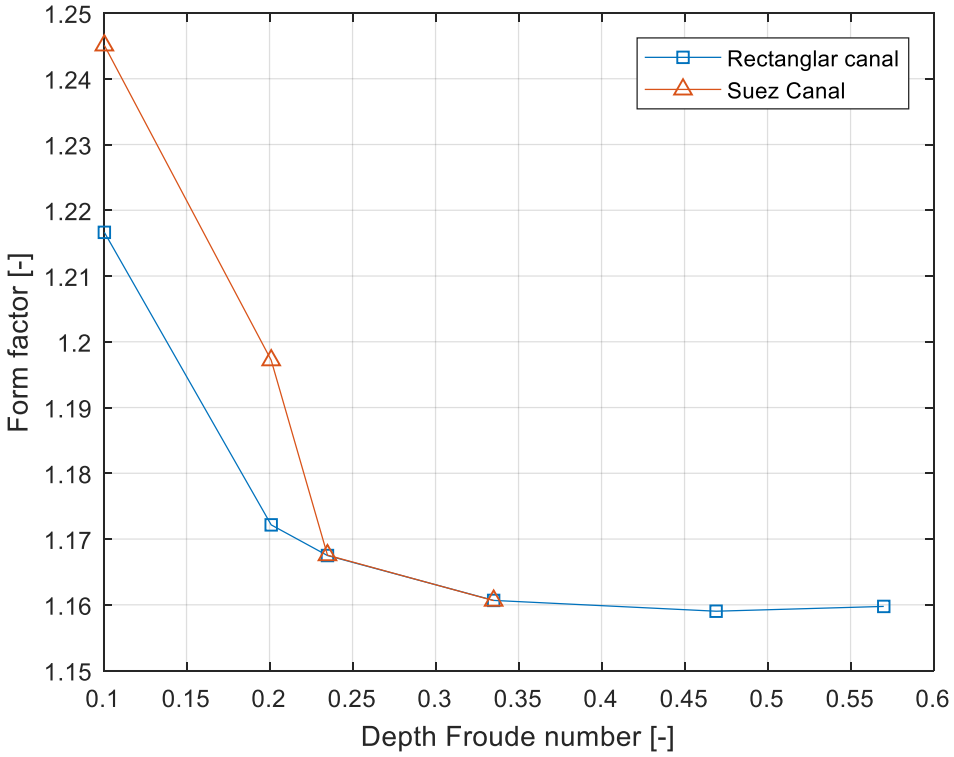

Figure 72. Predicted form factor for all case-studies using CFD

The form factor curve for the rectangular case-study shows a smooth behaviour, which is taken as an indication of the success of the present CFD model. The fact that the Suez Canal prediction seems to follow a similar path is taken as a good sign in terms of accuracy as well. The apparent disagreement between the two curves for the lowest speed suggests that there may be difficulty in predicting the underlying physics accurately. This is in line with expectations, which dictate that at a very low speed, the waves generated by the ship will be very short. These are difficult to capture if the mesh density is not high in the vicinity of where the abovementioned waves are expected. Although the generated mesh was progressively refined as the bank is approached, this may not have been sufficient for the lowest speeds. However, since the experimental method faces equal, if not greater challenges for the lowest speeds, it is considered that the results presented herein exhibit sufficient levels of accuracy.

The fact that the experimentally determined form factor is close to the low speed predictions of the present CFD model is encouraging. However, it also brings into question the experimental method for determination of the form factor, as applied to canal case-studies. This is typically assessed at very low speeds, where the wave resistance is

thought to be negligible. It was findings, specifically Figure 63, demonstrate that wave resistance is likely the cause in the experimental method's inability to predict the change in (1+k). As discussed previously, wave resistance does not decay in the rectangular canal as one might expect. The consequence of this is expressed in a contamination of the procedure used to experimentally determine the form factor. The results of this study suggest that CFD should be used to supplement the experimental determination of (1+k).

5.4 Concluding Remarks

This chapter presented an experimental and numerical assessment of the effects of bathymetry on ship squat and resistance. To demonstrate the practical importance of the work, the Suez Canal was modelled and compared to a rectangular canal. This study's attention was confined to low and moderate speeds in the Suez Canal, following the legal restrictions imposed on ships in the abovementioned waterway. Specifically, the maximum allowed speed is 7 knots. In this chapter, the numerical results showed best agreement with the experimental data. This is likely the case due to the ability of CFD to model complex phenomena without the need to individually prescribe each term in suitable manner, as is the case for potential flow.

Chapter Six

6. CONCLUSION AND FUTURE WORK

6.1 Introduction

This chapter presents a summary of the main outcomes of the studies discussed in this thesis, along with a clear demonstration of how the research aims and objectives have been achieved. Following this, a brief discussion on experimental, numerical, empirical and theoretical findings are will be given. Finally, recommendations will be presented for relevant fields of future research which are related to the work presented in this thesis.

6.2 Conclusion

The first research objective listed in Chapter 1 was as follows:

- ✓ **To review the available literature on squat of ships and to investigate the differences between various prediction techniques.**

The 'Critical Review' in Chapter 2 addressed this by presenting a wide-ranging overview of current squat and resistance predicting methods, from slender body theory and empirical equations to the state-of-the-art fully nonlinear unsteady RANS simulations and experimental testing. A discussion of each theory's strengths and weaknesses was also provided. The chapter also provided a literature survey on specific fields, such as predicting the squat and resistance of ships in shallow and restricted water regions. Finally, the gaps detected during the literature review were listed in the conclusion of Chapter 2. It was also emphasised that the main chapters of this thesis aimed to fill these gaps.

The following objectives were achieved in Chapter 3.

- ✓ **To perform a series of experiments on a model scale of the KRISO Container Ship (KCS) in shallow water and restricted water (including the New Suez Canal).**

- ✓ **To gain a better understanding of the effects of the water depth to ship draft ratios at various ship speeds on the squat phenomena and ship resistance in slope and rectangular canal.**
- ✓ **To study the blockage effect on ship resistance and squat.**
- ✓ **To determine a form factor value for the KCS at various water depth to ship draft ratios.**

The 'Experimental analysis of the squat of ships advancing through the New Suez Canal' in chapter three addressed this by presenting experimental results of the squat phenomenon in the new Suez Canal under both deep and shallow water operating conditions. The study reveals that a smaller keel clearance and higher speed will both significantly increase ship squat.

A large trim, sinkage and total resistance was observed when Froude number based on depth exceeded 0.4.

No significant impact on ship sinkage was observed when a ship is inside the canal compared to its former value before the ship entered the canal. Nonetheless, the total resistance force was seen to increase after the ship entered the canal due to blockage effects.

It was found out that higher blockage ratio results in significant squat, trim and added resistance (e.g. 20% increase in wave making resistance for the higher blockage values (0.1073) than the lower are (0.073) at depth Froude number =0.57). The maximum rate of increase in wave making resistance relative to blockage factor (k) according to (Figure 32) can be calculated from equation (110).

$$\frac{dC_w}{dk} = \frac{C_{w1} - C_{w2}}{K_1 - K_2} = \frac{0.001427}{0.03425} = 0.041652 \qquad (110)$$

Where C_{w1} is the wave making resistance coefficient at Fn_h is 0.57 and blockage ratio K_1 = 0.1073 and C_{w2} is the wave making resistance coefficient at Fn_h is 0.57 and blockage ratio K_2 = 0.0073.

The form factor reflecting the three dimensionality of ship was deduced based on measured resistance data in shallow water conditions for two blockage ratios. It was found

that 3D effect is more significant (almost 50% higher) for higher ship/canal blockage ratio.

Finally, it is important to consider the effect of both shallow and restricted water either separately or combined on the ship's sinkage, trim and resistance.

The following objectives were achieved in Chapter 4.

- ✓ **To detect the best trim angle for ships sailing in restricted waters to reduce resistance and therefore fuel consumption.**

The 'Experimental Investigation of the Trim Effect on the Behaviour of a Containership in Shallow water' in chapter four addressed this by presenting experimental results of the squat phenomenon and resistance in the restricted water. A series of model tests were conducted to measure the resistance, sinkage variations with speed, water depth and loading conditions under different trimming angles. It was also observed that level trim resulted in lowest resistance for high speeds. Albeit, there is less ship total resistance for the trim by stern case than for trim by bow case. Trim by bow recorded higher ship total resistance for all speeds. On the other side, it can be noticed that for high depth Froude numbers model sinkage was significantly decreased when model was trimmed by stern, compared to level condition and trimmed by bow condition. Moreover, the level trim condition recorded the higher sinkage at high speed.

The following objectives were achieved in Chapter 5.

- ✓ **To introduce a CFD-based RANS simulation model to predict the resistance and squat of the ship operating in shallow and restricted water.**
- ✓ **To predict the squat and resistance of a vessel advancing through a Suez Canal using this RANS solver.**
- ✓ **To make a comparison between different methodologies (experimental, numerical, analytical and empirical) for the prediction of ship squat and resistance on KCS model in sloped and rectangular canal.**

In this chapter, fully nonlinear unsteady RANS simulations were performed to predict the squat and resistance of a model-scale KCS container ship for two different cross section canal and for 0.144 ship draft at a range of forward speeds. The ship speeds and draft values were selected in analogy to the towing tank experiments of chapter three.

The main ship properties and the cross-section of the canal along with its dimensions were provided in chapter 3. Then, a list of empirical formula to predict ship squat was presented. Next, the slender body theory was conducted for rectangular canal and New Suez Canal to predict sinkage and trim. Next, the numerical setup of the CFD model was explained. Following this, a validation study was performed to assess the uncertainties of this work's CFD model. Finally, the squat and the resistance of the vessel in question were obtained using CFD and a comparison of the squat results with the experimental data was provided. This comparison showed that the CFD model predicted the ship squat values sufficiently well over various ship speeds.

6.3 Summary

In this study the squat phenomenon was experimentally investigated in the new Suez Canal under both deep and shallow water operating conditions. The results can be used as a useful database to predict the squat and added resistance of similar ships when navigating the new channel. In addition, presented numerical assessment of the effects of seabed proximity on ship squat and resistance was presented. To demonstrate the practical importance of this work, the Suez Canal was modelled and compared to a rectangular cross section canal. Attention was confined to low and moderate speeds in the Suez Canal, following the legal restrictions imposed on ships in the abovementioned waterway. Specifically, the maximum allowed speed is 7 knots.

Several discussions can be stated.

First, a ship's speed can be increased to up to 9 knots inside the Canal with no adverse effects, thus significantly reducing the time for a ship to pass through the Canal. Next, the study of reduced the Canal width to 62.5% of its real-life cross sectional area, no significant effect was observed on ship squat. Next, two factors were studied in this study

to examine their effects on ship navigating the Suez Canal these are water depth and canal width. Then, experimental test results confirmed the fact that when the model is moving in deep water (Fn_h < 0.4) wave pattern generated by ship motion doesn't change and accordingly almost no effect on sinkage, trim, and resistance. Next, two blockage values were also studied to examine canal bank proximity to navigation course effect as for as sinkage, trim and add resistance.

Second, the numerical results showed good agreement with the experimental data. This confirms configurations in more realistic way than the ability of CFD to model complex for potential flow. With the rapid growth in available computational power, studies such as the one presented here will become frequent. More importantly, the RANS method's ability to provide good predictions when compared to experiments reinforces the case for simulation-based design.

Third, in this study, the numerical model (RANS based) takes into account the realistic features of flow past ship in shallow and restricted water. The error at high speed which corresponding to 0.57 depth Froude number was found in order of 1.6% for resistance, 1.88% for trim and 24% for sinkage. However, at low speed the error was recorded slightly big, it can be explained as at low depth Froude numbers, the ship generates very small waves that requite a high mesh density which is not practically achievable. As the Froude number increases, the waves increase and the mesh can better capture them. Moreover, the present investigation focused on changes in form factor, wave resistance and friction across case-studies. The results reveal that the Prohaska test, which requires a vanishingly small wave resistance is valid for the Suez Canal, but may not be true for the rectangular canal. In fact, C_W vanishes with a reduction in depth Froude numbers below about 0.2. Surprisingly, the rectangular canal's wave resistance showed no signs of decay with low speeds. This suggests that a speed in the vicinity of 0.05 depth Froude number may be required to guarantee that wave effects are asymptotically negligible. Unfortunately, such case-studies are difficult to perform, due to limitations in the sensors used in the course of an experiment. From a numerical point of view, these case-studies are also challenging. The ship produces short waves whose resolution require a much finer mesh than was adopted here.

Fourth, in terms of form factor, the research, reported above indicates a sharp decline with increasing speed for both cases studied. The predictions suggest that as the speed is increased, the difference in (1+k), calculated for either case vanishes after $F_h = 0.25$. In the present cases, the form factor's multiplicative relationship with the frictional resistance coefficient means should not be ignored. It is unlikely that three dimensional effects are captured adequately by a linear resistance decomposition. To support this claim, changes in C_F between the Suez Canal, rectangular canal, and their double body variants was presented. Surprisingly, the difference between multiphase and double body frictional resistance coefficients was shown to be greater for the rectangular canal than the Suez Canal.

Fifth, the combination of insurmountable experimental and numerical limitations suggests that it may be more efficient to shift one's attention away from extremely low speeds. These low speeds are used to predict the ship resistance without the influence of wave resistance. In this study, it was demonstrated that this may not be a good approach because wave resistance plays an important role even at very low speeds (near Fr=0.1) Instead, the ability of modern computational tools should be exploited to a greater extent, as demonstrated in this study. The numerical method can be used to manipulate the physics of the problem to provide the desired component of ship resistance. Whether it is physically meaningful to split the total into linear components is a disputable matter. In the absence of better extrapolation techniques, one has little choice but to accept the above limitations. However, this is only the case if one continues to view the problem of ship resistance prediction and extrapolation to full-scale as a problem to be approached in a purely experimental way. It is hoped that the present study has demonstrated the strong applicability of CFD for problems of practical importance.

Finally, the results as per the slender body theory are quite far from the EFD and CFD results in terms of trim. However, the width to length ratio of the KCS is 14%, which is close to the upper limit for the slender body theory, thus limiting its applicability. Moreover, the observed discrepancies may stem from the assumption that a sloped canal can be represented by a rectangular canal with equal blockage. Regarding the empirical equations, they can be used to analyse the ships squat in the early design stages.

6.4 Recommendations for Future Research

Recommendations for further studies related to the work presented in this thesis are briefly outlined below.

1. In Chapter 3, a series of experiments on a model scale of the KRISO Container Ship (KCS) were conducted to measure sinkage and trim at various water depth to ship draft ratios and different ship speeds in shallow and restricted water. As a future piece of work, a testing of other types of ships that navigate via the new Suez Canal such as tankers, bunkers, RoRos, ... etc is important.

2. Additionally, the study that examined the blockage effects is done at different water depth to ship draft ratios. Furthermore, deep water tests are performed to compare the results against shallow water test. The present work could be extended in several ways. The ship's surface was assumed smooth to reduce the complexity of the physics. However, this is rarely, if ever, the case in reality. The variations in skin friction and wave resistance will undoubtedly change upon the inclusion of such roughness effects.

3. The research in Chapter 4 has provided a very useful starting point for investigation of the trim effect on the behaviour of a containership in shallow and restricted water. This study may be extended to study experimental and numerical investigation on the impact of heading on resistance, sinkage and trim in New Suez Canal, as well as to investigate how the drift angles amplify hydrodynamic effects, induced by the seabed topography.

4. The research in Chapter 5 has provided empirical, analytical, numerical and experimental techniques to predict the ship squat and resistance of the ship in question for New Suez Canal. In addition to this, wave resistance and form factor of the ship were predicted by using CFD simulations to run in both multiphase and double body conditions. This study should be extended to study the form factor related to different appendages fitted to the ship and their effect on the overall form factor.

5. Self-propulsion is an important topic. The presence of a rotating propeller at the stern of the ship causes a complex, unsteady three dimensional pressure field. This affects all aspects of the ship's hydrodynamics (Wang et al., 2017). The shallow water cases examined herein amplify the abovementioned effects in a manner that is not well understood. These problems should be addressed in subsequent studies.
6. Full-scale CFD analysis should be carried out and compered with the results of the present study.

REFERENCE

26th ITTC Specialist Committee, 2011. Fresh Water and Seawater Properties. Int. Towing Tank Conf. 5, 1596–1599. https://doi.org/10.1002/cphc.200400116

Alam, M.-R., Mei, C.C., 2008. Ships advancing near the critical speed in a shallow channel with a randomly uneven bed. J. Fluid Mech. 616, 397–417. https://doi.org/10.1017/S0022112008004035

Alderf, N., Leftançois, E., Sergent, P., Debaillon, P., 2008. Dynamic ship response integration for numerical prediction of squat in highly restricted waterways. Int. J. Numer. Methods Fluids 601–629. https://doi.org/10.1002/fld

Barrass, C.B., Derrett, D.R., 2012. Chapter 42 – Ship Squat in Open Water and in Confined Channels. Sh. Stab. Masters Mates 367–388. https://doi.org/10.1016/B978-0-08-097093-6.00042-6

Bechthold, J., Kastens, M., 2020. Robustness and quality of squat predictions in extreme shallow water conditions based on RANS-calculations. Ocean Eng. 197, 106780. https://doi.org/10.1016/j.oceaneng.2019.106780

Beck, R.F., Newman, J.N., Tuck, E.O., 1975. Hydrodynamic forces on ships in dredged channels. J. Sh. Res. 19, 166–171.

Beck, R.F., Tuck, E.O., 1971. Heave and pitch of ships in shallow water, in: Fourth Australasian Conference on Hydraulics and Fluid Mechanics1.

Beukelman, W., Gerritsma, J., 1982. THE DISTRIBUTION OF HYDRODYNAMIC MASS AND DAMPING OF AN OSCILLATING SHIPFORM IN SHALLOW WATER. Elev. Sci. Methodol. Semin. Sh. Hydrodyn. Varna, Bulg. 1. https://doi.org/10.3233/ISP-1982-2933903

Briggs, M.J., 2009. Ankudinov Ship Squat Predictions – Part I : Theory, Parameters, and FORTRAN Programs. US Army Eng. Res. Dev. Cent. 1–15.

Briggs, M.J., 2006. Ship squat predictions for ship/tow simulator (ERDC/CHL CHETN-I-72). Erdc/Chl Chetn-I-72 1–18.

Briggs, M.J., Daggett, L., 2009. Ankudinov Ship Squat Predictions – Part II : Laboratory

and Field Comparisons and Validations. US Army Eng. Res. Dev. Cent.

Briggs, M.J., Group, B., Debaillon, P., 2009. Comparisons of PIANC and Numerical Ship Squat Predictions for Rivers Elbe and Weser.

Calisal, S., Alidadi, M., 2011. A NUMERICAL STUDY ON SQUAT OF A WIGLEY HULL 1–5.

Castiglione, T., He, W., Stern, F., Bova, S., 2014. URANS simulations of catamaran interference in shallow water. J. Mar. Sci. Technol. 19, 33–51. https://doi.org/10.1007/s00773-013-0230-5

Celik, I.B., Ghia, U., Roache, P.J., Freitas, C.., 2008. Procedure for Estimation and Reporting of Uncertainty Due to Discretization in CFD Applications. J. Fluids Eng. 130, 078001. https://doi.org/10.1115/1.2960953

Constantine, T., 1960. On the movement of ships in restricted waterways. J. Fluid Mech. 9, 247. https://doi.org/10.1017/S0022112060001080

Dand, W.I., 1967. The wavemaking resistance of ships: Vertical force and form resistance of a hull at uniform velocity. PhD Thesis. University of Glasgow.

Degiuli, N., Hadžić, N., Pedišić, M., Buča, G.S., 2007. Form factor determination of the full, large breadth and shallow draught ship series. Brodogradnja 58, 380–388.

Delefortrie, G., Vantorre, M., Eloot, K., Verwilligen, J., Lataire, E., 2010. Squat prediction in muddy navigation areas. Ocean Eng. 37, 1464–1476. https://doi.org/10.1016/j.oceaneng.2010.08.003

Deng, H., Zhang, Z.H., Liu, J. Bin, Gu, J.N., 2014. Nonlinear effects on hydrodynamic pressure field caused by ship moving at supercritical speed in shallow water. Ocean Eng. 82, 144–149. https://doi.org/10.1016/j.oceaneng.2014.03.003

Duffy, J., 2008. Modelling of Ship-Bank Interaction and Ship Squat for Ship-Handling Simulation by.

Durbin, P.A., Pettersson Reif, B.A., 2011. Statistical theory and modelling for turbulent flow, Second Edi. ed. Wiley.

Eca, L., Hoekstra, M., 2014. A procedure for the estimation of the numerical uncertainty

of CFD calculations based on grid refinement studies. J. Comput. Phys. 262, 104–130. https://doi.org/10.1016/j.jcp.2014.01.006

Eca, L., Hoekstra, M., 2008. The numerical friction line. J. Mar. Sci. Technol. 13, 328–345. https://doi.org/10.1007/s00773-008-0018-1

Eca, L., Hoekstra, M., Beja Pedro, J.F., Falcao de Campos, J.A.C., 2013. On the characterization of grid density in grid refinement studies for discretization error estimation. Int. J. Numer. Methods Fluids 72, 119–134. https://doi.org/https://doi.org/10.1002/fld.3737

Eca, L., Vaz, G., Hoekstra, M., 2017. Iterative Errors in Unsteady Flow Simulations : Are they Really Negligible ? NuTTS-2017 1–5. https://doi.org/10.1016/j.cej.2015.03.004

el Moctar, O., Shigunov, V., Zorn, T., 2012. Duisburg Test Case : Post-Panamax Container Ship for Benchmarking. Sh. Technol. Res. J. 59, 50–64. https://doi.org/10.1179/str.2012.59.3.004

Elsherbiny, K., Tezdogan, T., Kotb, M., Incecik, A., Day, A.H., 2019a. An experimental investigation of the trim effect on the behaviour of a containership in shallow water, in: Proceedings of the ASME 2019 38th International Conference on Ocean, Offshore and Arctic Engineering OMAE2019, Glasgow, UK.

Elsherbiny, K., Tezdogan, T., Kotb, M., Incecik, A., Day, S., 2019b. Experimental analysis of the squat of ships advancing through the New Suez Canal. Ocean Eng. 178, 331–344. https://doi.org/10.1016/j.oceaneng.2019.02.078

Farkas, A., Degiuli, N., Martić, I., 2017. Numerical investigation into the interaction of resistance components for a series 60 catamaran. Ocean Eng. 146, 151–169. https://doi.org/10.1016/j.oceaneng.2017.09.043

Feng, A., Bai, W., You, Y., Chen, Z.M., Price, W.G., 2016. A Rankine source method solution of a finite depth, wave-body interaction problem. J. Fluids Struct. 62, 14–32. https://doi.org/10.1016/j.jfluidstructs.2016.01.002

Ferguson, A.M., 1977. Factors affecting the components of ship resistance. PhD Thesis. University o Glasgow, Department of Naval Architecture. University of Glasgow.

Gadd, G.E., 1967. A new turbulent friction formulation based on a reappraisal of Hughes' results. Trans. RINA 109, 109–511.

Gotman, A.S., 2002. Study Of Michell's Integral And Influence Of Viscosity And Ship Hull Form On Wave Resistance. Ocean. Eng. Int. 6, 74–115.

Gourlay, T., 2014. ShallowFlow: A Program to Model Ship Hydrodynamics in Shallow Water, in: OMAE 2014. p. 8. https://doi.org/10.1115/OMAE2014-23291

Gourlay, T., 2013. Ship Squat in Non-Uniform Water Depth 1–12.

Gourlay, T., 2009. Sinkage and trim of two ships passing each other on parallel courses. Ocean Eng. 36, 1119–1127. https://doi.org/10.1016/j.oceaneng.2009.06.003

Gourlay, T., 2008. Slender-body methods for predicting ship squat. Ocean Eng. 35, 191–200. https://doi.org/10.1016/j.oceaneng.2007.09.001

Gourlay, T., Ha, J.H., Mucha, P., Uliczka, K., 2015. Sinkage and Trim of Modern Container Ships in Shallow Water. Coast Ports 2015 1–8.

Gourlay, T., Tuck, E.O., 2001. The maximum sinkage of a ship. J. Sh. Res. 45, 50–58.

Guo, C., Xu, P., Wang, C., Zi, K., 2019. Numerical and Experimental Study of Blockage Effect Correction Method. China Ocean Eng. 33, 522–536. https://doi.org/10.1007/s13344-019-0050-4

Ha, J.H., Gourlay, T., 2017. Bow and Stern Sinkage Coefficients for Cargo Ships in Shallow Open Water 1–18.

Haase, M., Davidson, G., Binns, J., Thomas, G., Bose, N., 2016a. Full-scale resistance prediction in finite waters: A study using computational fluid dynamics simulations, model test experiments and sea trial measurements. Proc. Inst. Mech. Eng. Part M J. Eng. Marit. Environ. 231, 316–328. https://doi.org/10.1177/1475090216642467

Haase, M., Zurcher, K., Davidson, G., Binns, J.R., Thomas, G., Bose, N., 2016b. Novel CFD-based full-scale resistance prediction for large medium-speed catamarans. Ocean Eng. 111, 198–208. https://doi.org/10.1016/j.oceaneng.2015.10.018

Havelock, T., 1924. The Propagation of Groups of Waves in Dispersive Media, with Aplication to Waves on Water produced by a Travelling Disturbance 422–451.

https://doi.org/10.1098/rspa.1933.0074

He, W., Castiglione, T., Kandasamy, M., Stern, F., 2015. Numerical analysis of the interference effects on resistance , sinkage and trim of a fast catamaran. J. Mar. Sci. Technol. 292–308. https://doi.org/10.1007/s00773-014-0283-0

Hirt, C.. W., Nichols, B.. D., 1981. Volume of fluid (VOF) method for the dynamics of free boundaries. J. Comput. Phys. 39, 201–225. https://doi.org/10.1016/0021-9991(81)90145-5

Hughes, G., 1954. Friction and form resistance in turbulent flow and a proposed formulation for use in model and ship correlation. Trans. Inst. Nav. Arch. 96.

Inui, T., 1954. Wave-Making Resistance in Shallow Sea and in Restricted Water, with Special Reference to its Discontinuities 1, 1–10.

ISO GUM, 2008. Guide to the Expression of Uncertainty in Measurement,(1995), with Supplement 1, Evaluation of measurement data. Organ. Stand. Geneva, Switzerland. JCGM 101.

ITTC, 2017a. ITTC-Recommended Procedures and Guidelines Uncertainty Analysis, Instrument Cali-bration ITTC Quality System Manual Recommended Procedures and Guidelines Procedure.

ITTC, 2017b. Quality System Manual Recommended Procedures and Guidelines Procedure Uncertainty Analysis in CFD Verification and Validatio.

ITTC, 2017c. Recommended Procedures 1978 ITTC Performance Prediction Method, 4th revision, 7.5 – 02 03 – 01.4. 28th Int Towing Tank Conf.

ITTC, 2014. Example for Uncertainty Analysis of Resistance Tests in Towing Tanks, 27th International Towing Tank Conference.

ITTC, 2011. Recommended Procedures and Guidelines: Practical Guidelines for Ship CFD. 26th Int. Towing Tank Conf.

ITTC, 2008. Uncertainty Analysis in CFD Verification and Validation Methodology and Procedures. 25th ITTC 2008, Resist. Comm. 12.

ITTC, 2002. ITTC – Recommended Procedures and Guidelines Uncertainty Analysis ,

Example for Resistance Test.

Jachowski, J., 2008. Assessment of ship squat in shallow water using CFD. Arch. Civ. Mech. Eng. 8, 27–36. https://doi.org/10.1016/S1644-9665(12)60264-7

Janssen, P.P., Schijf, J.., 1953. he relation between the form of cross section the cross section, the method of revetment and the distribution of the water velocities in a waterway, in: PIANC 18th Congress 1953, Rome, Section SI C1. PIANC.

Ji, S.C., Ouahsine, A., Smaoui, H., Sergent, P., 2012. 3-D numerical simulation of convoy-generated waves in a restricted waterway. J. Hydrodyn. 24, 420–429. https://doi.org/10.1016/S1001-6058(11)60263-1

Jones, D.A., Clarke, D.B., 2010. Fluent Code Simulation of Flow around a Naval Hull: the DTMB 5415. Def. Sci. Technol. Organ. Victoria (Australia), Marit. platforms Div.

Joukovski, N., 1903. On the wave of translation. Complet. Work.

Katsui, T., Asai, H., Himeno, Y., Tahara, Y., 2005. The proposal of a new friction line, in: Fifth Osaka Colloquium on Advanced CFD Applications to Ship Flow and Hull Form Design, Osaka, Japan.

Kazerooni, M.F., Seif, M.S., 2014. Experimental evaluation of ship squat in shallow waters. J. Brazilian Soc. Mech. Sci. Eng. 36, 559–569. https://doi.org/10.1007/s40430-013-0114-y

KCS Geometry and Conditions, SIMMAN 2008, FORCE Technology, n.d.

Kinaci, O.K., Sukas, O.F., Bal, S., 2016. Prediction of wave resistance by a Reynolds-averaged Navier-Stokes equation-based computational fluid dynamics approach. Proc. Inst. Mech. Eng. Part M J. Eng. Marit. Environ. 230, 531–548. https://doi.org/10.1177/1475090215599180

Kok, Z., Jin, Y., Chai, S., Denehy, S., Duffy, J., 2018. URANS prediction of berthed ship–passing ship interactions. Ships Offshore Struct. 13, 561–574. https://doi.org/10.1080/17445302.2018.1429136

Korkmaz, K.B., Werner, S., Bensow, R.E., 2019. Numerical friction lines for CFD based

form factor determination, in: VIII International Conference on Computational Methods in Marine Engineering MARINE 2019.

Kreitner, J., 1934. The Resistance of Ships in Confined Waters. Werft-Rederei-Hafen.

Lamb, H., 1932. Hydrodynamics. Cambridge Univ. Press 6th revise, 262–264. https://doi.org/10.1017/CBO9781107415324.004

Larsson, L., Raven, H.C., 2010. Ship resistance and flow.

Lataire, E., Vantorre, M., Delefortrie, G., 2012. A prediction method for squat in restricted and unrestricted rectangular fairways. Ocean Eng. 55, 71–80. https://doi.org/10.1016/j.oceaneng.2012.07.009

Lazauskas, L. V, 2009. Resistance, Wave-Making and Wave-Decay of Thin Ships, with Emphasis on the Effects of Viscosity.

Lea, G.K., Feldman, J.P., 1972. Transcritical flow past slender ships, in: 9th Symposium on Naval Hydrodynamics. Washington DC, pp. 1527–1542.

Lesieur, M., 2008. Turbulence in fluids, 4th ed, Physics of Fluids. Springer. https://doi.org/10.1063/1.1711203

Liu, J., Hekkenberg, R., Rotteveel, E., Hopman, H., 2015. Literature review on evaluation and prediction methods of inland vessel manoeuvrability. Ocean Eng. 106, 458–471. https://doi.org/10.1016/j.oceaneng.2015.07.021

Ma, S.J., Zhou, M.G., Zou, Z.J., 2013. Hydrodynamic interaction among hull, rudder and bank for a ship sailing along a bank in restricted waters. J. Hydrodyn. 25, 809–817. https://doi.org/10.1016/S1001-6058(13)60428-X

Mei, C.C., 1976. Flow around a thin body moving in shallow water. J. Fluid Mech. 77, 737. https://doi.org/10.1017/S0022112076002863

Mei, C.C., Choi, H.S., 1987. Forces on a slender ship advancing near the critical speed in a wide canal. J. Fluid Mech. 179, 59–76. https://doi.org/10.1017/S0022112087001435

Michell, J.H., 1898. The wave-resistance of a ship. London, Edinburgh, Dublin Philos. Mag. J. Sci. 45, 106–123.

Millward, A., 1996. A review of the prediction of squat in shallow water. J. Navig. 77–88. https://doi.org/10.1017/S0373463300013126

Min, K.-S., Kang, S.-H., 2010. Study on the form factor and full-scale ship resistance. J. Mar. Sci. Technol. 15, 108–118. https://doi.org/10.1007/s00773-009-0077-y

Molland, A.F., Turnock, S.R., Hudson, D.A., 2017. Model-Ship Extrapolation, in: Ship Resistance and Propulsion: Practical Estimation of Ship Propulsive Power. Cambridge University Press, Cambridge, pp. 70–85. https://doi.org/10.1017/9781316494196.006

Mucha, P., 2017. On Simulation-based Ship Maneuvering Prediction in Deep and Shallow Water.

Mucha, P., Deng, G., Gourlay, T., Moctar, O. el, 2016. Validation studies on numerical prediction of ship squat and resistance in shallow water. Proc. 4th MASHCON 83–92. https://doi.org/10.18451/978-3-939230-38-0

Mucha, P., Dettmann, T., Ferrari, V., el Moctar, O., 2019. Experimental investigation of free-running ship manoeuvers under extreme shallow water conditions. Appl. Ocean Res. 83, 155–162. https://doi.org/10.1016/j.apor.2018.09.008

Mucha, P., Moctar, O. el, Dettmann, T., Tenzer, M., 2018. An experimental study on the effect of confined water on resistance and propulsion of an inland waterway ship. Ocean Eng. 167, 11–22. https://doi.org/10.1016/j.oceaneng.2018.08.009

Nandhini, V., Nallayarasu, S., 2019. CFD simulation of the passing vessel effects on moored vessel. Ships Offshore Struct. 0, 1–16. https://doi.org/10.1080/17445302.2019.1606764

Newman, J.N., 1965. Propagation of water waves over an infinite step. J. Fluid Mech. 23, 399–415. https://doi.org/10.1017/S0022112065001453

Pacuraru, F., Domnisoru, L., 2017. Numerical investigation of shallow water effect on a barge ship resistance. IOP Conf. Ser. Mater. Sci. Eng. 227. https://doi.org/10.1088/1757-899X/227/1/012088

Phillips, T., 2012. Extrapolation-based Discretization Error and Uncertainty Estimation

in Computational Fluid Dynamics.

PIANC, 2014. Report 121 - 2014.

Prakash, S.M.N., Chandra, B., 2013. Numerical Estimation of Shallow Water Resistance of a River-Sea Ship using CFD. Int. J. Comput. Appl. 71, 33–40. https://doi.org/https://doi.org/10.5120/12357-8670

Prandtl, L., 1925. Report on the investigation of developed turbulence, Translation of " Bericht über Untersuchungen zur ausgebildeten Turbulenz." Zeitschrift für angewandte Mathematik und Mechanik, vol. 5, no. 2, April 1925.

Richardson, L.F., 1911. The Approximate Arithmetical Solution by Finite Differences of Physical Problems involving Differential Equations, with an Application to the Stresses in a Masonry Dam. Philos. Trans. th R. Soc. London,Containing Pap. a Math. Phys. Character 210, 307–357.

Roache, P.J., 1998. Validation and Verification in computational science and engineering. Hermosa Albuquerque, NM.

Roache, P.J., 1997. Quantification of Uncertainty in Computational Fluid Dynamics. Annu. Rev. Fluid Mech. 29, 123–160. https://doi.org/10.1146/annurev.fluid.29.1.123

Römisch, K., 1989. Empfehlungen zur Bemessung von Hafeneinfahrten. Tech. Univ. Dresden.

Rotteveel, E., Hekkenberg, R.G., 2015. The Influence of Shallow Water and Hull Form Variations on Inland Ship Resistance 2, 220–236.

Roy, C., 2005. Review of code and solution verification procedures for computational simulation. J. Comput. Phys. 205, 131–156. https://doi.org/10.1016/j.jcp.2004.10.036

Roy, C., Blottner, F.G., 2001. Assessment of One- and Two-Equation Turbulence Models for Hypersonic Transitional Flows. J. Spacecr. Rockets 38, 699–710. https://doi.org/10.2514/2.3755

Sakamoto, N., Wilson, R.V., Stern, F., 2007. Reynolds-averaged Navier-Stokes

simulations for high-speed wigley hull in deep and shallow water. J. Sh. Res. 51, 187–203.

Schlichting, H., 1979. Boundary-Layer Theory, 7th ed. McGraw-Hill. https://doi.org/10.1007/978-3-662-52919-5

Schoenherr, K., 1932. Resistance of flat surfaces moving through a fluid. Trans. Soc. Nav. Arch. Mar. Eng. 40, 279–313.

Schultz-Grunow, F., 1941. New frictional resistance law for smooth plates.

Sergent, P., Lefrançois, E., Mohamad, N., 2015. Virtual bottom for ships sailing in restricted waterways (unsteady squat). Ocean Eng. 110, 205–214. https://doi.org/10.1016/j.oceaneng.2015.10.017

Sherbaz, S., Duan, W., 2014. Ship trim optimization: assessment of influence of trim on resistance of MOERI container ship. ScientificWorldJournal. 2014, 603695. https://doi.org/10.1155/2014/603695

Shevchuk, I., Kornev, N., 2017. Study of unsteady hydrodynamic effects in the stern area of river cruisers in shallow water. 7th Int. Conf. Comput. Methods Mar. Eng. Mar. 2017 2017-May, 440–448. https://doi.org/10.1080/09377255.2017.1349599

Shivachev, E., Khorasanchi, M., Day, A.H., 2017. Trim influence on KRISO container ship (KCS); an experimental and numerical study, in: Proceedings of the ASME 2017 36th International Conference on Ocean, Offshore and Arctic Engineering. pp. 1–7. https://doi.org/10.1115/OMAE2017-61860

Simonsen, C.D., Otzen, J.F., Joncquez, S., Stern, F., 2013. EFD and CFD for KCS heaving and pitching in regular head waves. J. Mar. Sci. Technol. 18, 435–459. https://doi.org/10.1007/s00773-013-0219-0

Stern, F., Yang, J., Wang, Z., Sadat-Hosseini, H., Mousaviraad, M., 2013. Computational ship hydrodynamics: Nowadays and way forward. Int. Shipbuild. Prog. 60, 3–105. https://doi.org/10.3233/ISP-130090

Suez Canal Authority, 2019. Suez Canal Rules of Navigation. https://doi.org/https://www.suezcanal.gov.eg/English/Navigation/Pages/RulesOfNa

vigation.aspx

Suez Canal Authority, 2018. Suez Canal Traffic Statistics: Annual Report 2018.

Telfer, E. V., 1927. Ship resistance similarity. Trans. R. Inst. Nav. Archit. 69, 174–190.

Terziev, M., Tezdogan, T., Incecik, A., 2019a. Influence of mixed flow on ship hydrodynamics in dredged channels, in: OMAE2019, Glasgow, UK. pp. 1–10.

Terziev, M., Tezdogan, T., Incecik, A., 2019b. Application of eddy-viscosity turbulence models to problems in ship hydrodynamics. Ships Offshore Struct. 1–24. https://doi.org/10.1080/17445302.2019.1661625

Terziev, M., Tezdogan, T., Incecik, A., 2019c. A geosim analysis of ship resistance decomposition and scale effects with the aid of CFD. Appl. Ocean Res. 92. https://doi.org/10.1016/j.apor.2019.101930

Terziev, M., Tezdogan, T., Incecik, A., 2019d. Under Review: Numerical verification procedures applied to a geosim series in shallow water ship hydrodynamics using CFD. Appl. Oc.

Terziev, M., Tezdogan, T., Oguz, E., Gourlay, T., Demirel, Y.K., Incecik, A., 2018. Numerical investigation of the behaviour and performance of ships advancing through restricted shallow waters. J. Fluids Struct. 76, 185–215. https://doi.org/10.1016/j.jfluidstructs.2017.10.003

Tezdogan, T., Demirel, Y.K., Kellett, P., Khorasanchi, M., Incecik, A., Turan, O., 2015. Full-scale unsteady RANS CFD simulations of ship behaviour and performance in head seas due to slow steaming. Ocean Eng. 97, 186–206. https://doi.org/10.1016/j.oceaneng.2015.01.011

Tezdogan, T., Incecik, A., Turan, O., 2016a. A numerical investigation of the squat and resistance of ships advancing through a canal using CFD. J. Mar. Sci. Technol. 21, 86–101. https://doi.org/10.1007/s00773-015-0334-1

Tezdogan, T., Incecik, A., Turan, O., 2016b. Full-scale unsteady RANS simulations of vertical ship motions in shallow water. Ocean Eng. 123, 131–145. https://doi.org/10.1016/j.oceaneng.2016.06.047

Today, E., 2019. egypt today [WWW Document]. https://doi.org/https://www.ceicdata.com/en/egypt/maritime-transport-revenues/maritime-transport-suez-canal-revenues

Toxopeus, S.L., 2013. Viscous-flow calculations for KVLCC2 in deep and shallow water. Comput. Methods Appl. Sci. 29, 151–169. https://doi.org/10.1007/978-94-007-6143-8_9

Toxopeus, S.L., Simonsen, C.D., Guilmineau, E., Visonneau, M., Xing, T., Stern, F., 2013. Investigation of water depth and basin wall effects on KVLCC2 in manoeuvring motion using viscous-flow calculations. J. Mar. Sci. Technol. 18, 471–496. https://doi.org/10.1007/s00773-013-0221-6

Tuck, E.O., 1967a. Sinkage and Trim in Shallow Water of Finite Width. Schiffstechnik 14, 92–94.

Tuck, E.O., 1967b. A Simple "Filon-Trapezoidal" Rule 121, 1–12.

Tuck, E.O., 1966. Shallow-Water Flows Past Slender Bodies. J. Fluid Mech. 26, 81–95. https://doi.org/10.1017/S0022112066001101

Tuck, E.O., Lazauskas, L. V, 2008. Drag on a ship and Michell's integral, in: 22nd Int. Congress of Theoretical and Applied Mechanics, Adelaide, South Australia, August.

Tuck, E.O., Lazauskas, L. V, 1998. OPTIMUM HULL SPACING OF A FAMILY OF MULTIHULLS 1–38.

Tuck, E.O., Newman, J.N., 1976. Hydrodynamic interactions between ships, in: Symposium on Naval Hydrodynamics, 10th, Cambridge, Mass, June 24-28.

Tuck, E.O., Taylor, J.P., 1970. Shallow wave problems in ship hydrodynamics, in: 8th Symposium Naval Hydrodynamics. pp. 627–659.

Tunaley, J.K.E., 2014. Ship Wakes in Shallow Waters. LRDC Rep. 6–9.

van Hoydonck, W., Toxopeus, S., Eloot, K., Bhawsinka, K., Queutey, P., Visonneau, M., 2018. Bank effects for KVLCC2. J. Mar. Sci. Technol. 0, 1–26. https://doi.org/10.1007/s00773-018-0545-3

van Oortmerssen, G., 1976. The motions of a ship in swallow water. Ocean Eng. 3, 221–

255. https://doi.org/10.1016/0029-8018(76)90025-1

Varyani, K.S., 2006. Squat effects on high speed craft in restricted waterways. Ocean Eng. 33, 365–381. https://doi.org/10.1016/j.oceaneng.2005.04.016

Wang, H.Z., Zou, Z.J., 2014. Numerical study on hydrodynamic interaction between a berthed ship and a ship passing through a lock. Ocean Eng. 88, 409–425. https://doi.org/10.1016/j.oceaneng.2014.07.001

Wang, J., Zou, L., Wan, D., 2017. CFD simulations of free running ship under course keeping control. Ocean Eng. 141, 450–464. https://doi.org/10.1016/j.oceaneng.2017.06.052

Wang, Z.Z., Xiong, Y., Shi, L.P., Liu, Z.H., 2015. A numerical flat plate friction line and its application. J. Hydrodyn. 27, 383–393. https://doi.org/10.1016/S1001-6058(15)60496-6

White, F., 2006. Viscous fluid flow, 3rd ed. McGraw-Hill.

Wilcox, D.C., 2006. Turbulence modeling for CFD, 3rd ed, Transportation Research Record. DCW Industries. https://doi.org/10.1016/j.aqpro.2013.07.003

Wortley, S., 2013. CFD Analysis of Container Ship Sinkage, Trim and Resistance.

WORLD MARITIME NEWS, 2016. Grounding in Suez canal. Retrieved from. https://search.worldmaritimenews.com/search?s=grounding+in+suez+canal&submit=submit, Accessed date: 30 March 2018.

Xia, L., Yuan, S., Zou, Z., Zou, L., 2020. Uncertainty quantification of hydrodynamic forces on the DTC model in shallow water waves using CFD and non-intrusive polynomial chaos method 198.

Xing, T., Stern, F., 2010. Factors of Safety for Richardson Extrapolation. J. Fluids Eng. 132, 061403. https://doi.org/10.1115/1.4001771

Yao, J.X., Zou, Z.J., 2010. Calculation of ship squat in restricted waterways by using a 3D panel method. J. Hydrodyn. 22, 472–477. https://doi.org/10.1016/S1001-6058(09)60241-9

Yao, J.X., Zou, Z.J., Wang, H.M., 2011. Numerical study on bank effects for a ship sailing

in shallow channel. J. Shanghai Jiaotong Univ. 16, 91–96. https://doi.org/10.1007/s12204-011-1100-0

Yeung, R.W., 1978. On the interactions of slender ships in shallow water. J. Fluid Mech. 85, 143–159. https://doi.org/10.1017/S0022112078000567

Yuan, Z.M., 2018. Ship Hydrodynamics in Confined Waterways. J. Sh. Res. 1–14. https://doi.org/http://dx.doi.org/10.5957/JOSR.04170020

Yuan, Z.M., Day, A.H., 2015. Optimum distance between two advancing ships arranged side by side, in: Proceedings of the ASME 2015 34th International Conference on Ocean, Offshore and Arctic Engineering OMAE2015. pp. 1–7.

Yuan, Z.M., Incecik, A., Day, A.H., Jia, L., 2015. Double Doppler shift theory on water waves generated by a translating and oscillating source. 30th Intl Work. Water Waves Float. Bodies.

Yuan, Z.M., Ji, C., Incecik, A., Zhao, W., Day, A.H., 2016. Theoretical and numerical estimation of ship-to-ship hydrodynamic interaction effects. Ocean Eng. 121, 239–253. https://doi.org/10.1016/j.oceaneng.2016.05.032

Zaghi, S., Broglia, R., Di Mascio, A., 2011. Analysis of the interference effects for high-speed catamarans by model tests and numerical simulations. Ocean Eng. 38, 2110–2122. https://doi.org/10.1016/j.oceaneng.2011.09.037

Zeng, Q., Hekkenberg, R., Thill, C., 2019. A Study of Ship's Frictional Resistance in Extremely Shallow Water 1–11.

Zeng, Q., Thill, C., Hekkenberg, R., Rotteveel, E., 2018. A modification of the ITTC57 correlation line for shallow water. J. Mar. Sci. Technol. 0, 0. https://doi.org/10.1007/s00773-018-0578-7

Zeraatgar, H., Vakilabadi, K.A., Yousefnejad, R., 2011. Parametric Analysis of Ship Squat in Shallow Water by Model Test. Brodogradnja 62, 37–43.

Zhang, S., Tezdogan, T., Zhang, B., Xu, L., Lai, Y., 2018a. Hull form optimisation in waves based on CFD technique. Ships Offshore Struct. 13, 149–164. https://doi.org/10.1080/17445302.2017.1347231

Zhang, S., Zhang, B., Tezdogan, T., Xu, L., Lai, Y., 2018b. Computational fluid dynamics-based hull form optimization using approximation method. Eng. Appl. Comput. Fluid Mech. 12, 74–88. https://doi.org/10.1080/19942060.2017.1343751

Zhang, S., Zhang, B., Tezdogan, T., Xu, L., Lai, Y., 2017. Research on bulbous bow optimization based on the improved PSO algorithm. China Ocean Eng. 31, 487–494. https://doi.org/10.1007/s13344-017-0055-9

Zhang, Z., Deng, H., Li, Y. chen, Gu, J. nong, 2017. Analytical models of sub-supercritical ship hydrodynamic pressure field with the dispersive effect. Ocean Eng. 133, 66–72. https://doi.org/10.1016/j.oceaneng.2017.01.028

Zhang, Z.H., Deng, H., Wang, C., 2015. Analytical models of hydrodynamic pressure field causing by a moving ship in restricted waterways. Ocean Eng. 108, 563–570. https://doi.org/10.1016/j.oceaneng.2015.08.046

Zhou, M.-G., Zou, Z.-J., Yao, J.-X., 2013. Prediction of ship squat in restricted waters. Chuan Bo Li Xue/Journal Sh. Mech. 17. https://doi.org/10.3969/j.issn.1007-7294.2013.06.005

Zou, L., Larsson, L., 2013. Numerical predictions of ship-to-ship interaction in shallow water. Ocean Eng. 72, 386–402. https://doi.org/10.1016/j.oceaneng.2013.06.015

PUBLICATIONS

The following papers have been either published, or submitted for consideration for publication, in scientific journals and conferences. All of the papers listed below have been drawn from this thesis.

Journal papers:

1. Elsherbiny, K., Tezdogan, T., Kotb, M., Incecik, A., Day, S., 2019. Experimental analysis of the squat of ships advancing through the New Suez Canal. Ocean Eng. 178, 331–344. https://doi.org/10.1016/j.oceaneng.2019.02.078

2. Elsherbiny, K., Terziev, M., Tezdogan, T., Incecik, A. & Kotb,. M. (2019) 'Numerical and experimental study on hydrodynamic performance of ships advancing through different canals'. Journal of Ocean Engineering. Vol. 195, https://doi.org/10.1016/j.oceaneng.2019.106696

Conference paper:

1. Elsherbiny, K., Tezdogan, T., Kotb, M., Incecik, A., Day, A.H., 2019. An experimental investigation of the trim effect on the behaviour of a containership in shallow water, in: Proceedings of the ASME 2019 38th International Conference on Ocean, Offshore and Arctic Engineering OMAE2019, Glasgow, UK.

Appendix

Table 13 Experimental results for Case I in chapter 3 for H/T=2.5

H/T=2.5					
Model speed (m/s)	Depth Froude number (Fn)	Trim (deg.)	Load (N)	Sinkage (mm)	C_T
0.18	0.10	-0.005	0.04	0.17	0.005
0.24	0.13	-0.003	0.27	0.11	0.006
0.30	0.17	-0.005	0.41	-0.36	0.006
0.36	0.20	-0.003	0.58	-0.29	0.006
0.42	0.23	-0.002	0.78	-0.77	0.006
0.48	0.27	-0.006	1.00	-1.21	0.006
0.53	0.30	-0.006	1.22	-1.44	0.005
0.59	0.33	-0.007	1.51	-1.96	0.006
0.83	0.47	-0.016	2.92	-5.15	0.005
1.01	0.57	-0.050	4.18	-8.65	0.005
1.19	0.67	-0.133	5.50	-15.64	0.005
1.31	0.74	-0.172	8.59	-25.59	0.007
1.37	0.77	0.306	18.39	-35.33	0.013

Table 14 Experimental results for Case I in chapter 3 for H/T=2.2

H/T=2.2					
Model speed (m/s)	Depth Froude number (Fn)	Trim (deg.)	Load (N)	Sinkage (mm)	C_T
0.18	0.10	0.0008	0.20	-0.70	0.0048
0.24	0.13	-0.0102	0.24	-0.41	0.0050
0.30	0.17	-0.0007	0.40	-0.58	0.0054
0.36	0.20	-0.0068	0.52	-0.49	0.0049
0.42	0.23	-0.0128	0.77	-0.76	0.0053
0.48	0.27	-0.0157	1.05	-1.39	0.0055
0.53	0.30	-0.0224	1.30	-2.09	0.0054
0.59	0.33	-0.0266	1.56	-2.39	0.0053
0.83	0.47	-0.0572	3.15	-5.96	0.0054
1.01	0.57	-0.1028	4.51	-10.07	0.0052
1.19	0.67	-0.1853	6.75	-17.77	0.0057
1.31	0.74	-0.1717	11.50	-28.41	0.0080
1.37	0.77	0.6542	27.82	-38.21	0.0178

Table 15 Experimental results for Case I in chapter 3 for H/T=2

H/T=2					
Model speed (m/s)	Depth Froude number (Fn)	Trim (deg.)	Load (N)	Sinkage (mm)	C_T
0.18	0.10	0.0011	0.34	-0.36	0.0050
0.24	0.13	-0.0094	0.30	-0.24	0.0059
0.30	0.17	-0.0129	0.50	-0.42	0.0062
0.36	0.20	-0.0114	0.70	-0.87	0.0060
0.42	0.23	-0.0258	0.88	-0.94	0.0056
0.48	0.27	-0.0215	1.17	-1.36	0.0057
0.53	0.30	-0.0318	1.42	-2.03	0.0054
0.59	0.33	-0.0344	1.70	-2.80	0.0053
0.83	0.47	-0.0654	3.38	-6.48	0.0054
1.01	0.57	-0.1120	4.96	-10.79	0.0053
1.19	0.67	-0.1783	7.55	-19.96	0.0059
1.31	0.74	0.0425	16.70	-32.87	0.0107
1.37	0.77	1.0621	37.15	-39.71	0.0219

Table 16 Experimental results for Case I in chapter 3 for H/T=1.78

H/T=1.78					
Model speed (m/s)	Depth Froude number (Fn)	Trim (deg.)	Load (N)	Sinkage (mm)	C_T
0.18	0.10	-0.0075	0.21	-0.02	0.0058
0.24	0.13	0.0016	0.41	0.01	0.0059
0.30	0.17	-0.0043	0.55	-0.66	0.0063
0.36	0.20	-0.0106	0.76	-0.61	0.0061
0.42	0.23	-0.0132	0.96	-1.05	0.0057
0.48	0.27	-0.0066	1.35	-1.75	0.0060
0.53	0.30	-0.0111	1.70	-2.06	0.0060
0.59	0.33	-0.0173	2.01	-2.64	0.0058
0.83	0.47	-0.0263	3.99	-7.24	0.0059
1.01	0.57	-0.0520	6.11	-11.92	0.0061
1.19	0.67	-0.0691	10.10	-20.72	0.0073
1.31	0.74	0.3891	23.68	-20.56	0.0141
1.37	0.77	1.6000	49.66	-20.98	0.0271

Table 17 Experimental results for Case II in chapter 3 for H/T=1.78

H/T=1.78					
Model speed (m/s)	Depth Froude number (Fn)	Trim (deg.)	Load (N)	Sinkage (mm)	C_T
0.18	0.10	0.0011	0.12	-0.44	0.00908
0.24	0.13	0.0036	0.18	-0.06	0.00908
0.30	0.17	0.0047	0.50	-0.43	0.00910
0.36	0.20	0.0068	0.77	-0.09	0.00893
0.42	0.23	0.0079	0.95	-0.76	0.00763
0.48	0.27	0.0046	1.25	-1.35	0.00737
0.53	0.30	-0.0010	1.51	-1.87	0.00679
0.59	0.33	-0.0043	1.93	-2.44	0.00681
0.83	0.47	-0.0009	2.45	-3.24	0.00710
1.01	0.57	0.0577	6.45	-7.84	0.00948
1.19	0.67	0.1866	11.90	-11.41	0.01183

Table 18 Experimental results for Case II in chapter 3 for H/T=2

H/T=2					
Model speed (m/s)	Depth Froude number (Fn)	Trim (deg.)	Load (N)	Sinkage (mm)	C_T
0.18	0.10	-0.0033	0.05	0.06	0.0070
0.24	0.13	-0.0052	0.44	-0.10	0.0074
0.30	0.17	-0.0088	0.53	-0.51	0.0067
0.36	0.20	-0.0103	0.82	-0.57	0.0071
0.42	0.23	-0.0142	1.12	-1.13	0.0071
0.48	0.27	-0.0164	1.32	-1.10	0.0064
0.53	0.30	-0.0212	1.65	-2.00	0.0063
0.59	0.33	-0.0284	2.04	-2.50	0.0064
0.83	0.47	-0.0116	5.05	-6.30	0.0080
1.01	0.57	0.0863	9.55	-10.58	0.0103
1.19	0.67	-0.0033	0.05	0.06	0.0070

Table 19 Experimental results for Case II in chapter 3 for H/T=2.2

H/T=2.2					
Model speed (m/s)	Depth Froude number (Fn)	Trim (deg.)	Load (N)	Sinkage (mm)	C_T
0.18	0.10	-0.0045	0.03	0.05	0.0026
0.24	0.13	-0.0031	0.04	0.07	0.0054
0.30	0.17	-0.0050	0.33	-0.06	0.0057
0.36	0.20	-0.0075	0.39	-0.38	0.0059
0.42	0.23	-0.0067	0.65	-0.70	0.0061
0.48	0.27	-0.0107	0.86	-1.49	0.0060
0.53	0.30	-0.0087	1.15	-1.68	0.0061
0.59	0.33	-0.0148	1.33	-2.12	0.0062
0.83	0.47	-0.0176	1.92	-2.47	0.0065
1.01	0.57	-0.0122	4.32	-6.69	0.0074
1.19	0.67	0.0654	8.01	-9.54	0.0080

Table 20 Experimental results for Case III in chapter 3 for H/T=2.2

H/T=2.2					
Model speed (m/s)	Depth Froude number (Fn)	Trim (deg.)	Load (N)	Sinkage (mm)	C_T
0.18	0.10	-0.0065	0.15	-0.25	0.0080
0.24	0.13	-0.0051	0.23	-0.13	0.0088
0.30	0.17	-0.0071	0.31	-0.48	0.0067
0.36	0.20	-0.0080	0.78	-0.51	0.0105
0.42	0.23	-0.0088	0.98	-0.81	0.0093
0.48	0.27	-0.0107	1.03	-1.82	0.0071
0.53	0.30	-0.0092	1.39	-1.90	0.0073
0.59	0.33	-0.0114	1.73	-2.43	0.0072
0.83	0.47	-0.0119	2.07	-2.97	0.0070
1.01	0.57	0.0501	5.60	-7.35	0.0096
1.19	0.67	0.1845	10.35	-8.79	0.0121

Table 21 Experimental results for Case III in chapter 3 for H/T=2

H/T=2					
Model speed (m/s)	Depth Froude number (Fn)	Trim (deg.)	Load (N)	Sinkage (mm)	C_T
0.18	0.10	-0.0026	-0.06	0.31	0.0070
0.24	0.13	-0.0028	0.25	-0.03	0.0088
0.30	0.17	0.0002	0.48	-0.71	0.0094
0.36	0.20	-0.0044	0.65	-0.41	0.0081
0.42	0.23	-0.0041	1.14	-0.75	0.0099
0.48	0.27	-0.0059	1.26	-0.84	0.0080
0.53	0.30	-0.0085	1.52	-1.81	0.0074
0.59	0.33	-0.0094	1.88	-1.94	0.0072
0.83	0.47	-0.0150	2.53	-3.05	0.0079
1.01	0.57	0.0708	7.93	-7.18	0.0126
1.19	0.67	0.2213	12.70	-9.60	0.0137

Table 22 Experimental results for Case III in chapter 3 for H/T=1.78

H/T=1.78					
Model speed (m/s)	Depth Froude number (Fn)	Trim (deg.)	Load (N)	Sinkage (mm)	C_T
0.18	0.10	-0.0033	0.16	-0.002	0.0120
0.24	0.13	-0.0027	0.17	0.188	0.0056
0.30	0.17	-0.0034	0.50	0.020	0.0090
0.36	0.20	-0.0008	0.76	-0.316	0.0089
0.42	0.23	-0.0008	0.99	-0.400	0.0079
0.48	0.27	0.0033	1.38	-1.074	0.0081
0.53	0.30	0.0047	1.95	-2.088	0.0088
0.59	0.33	0.0070	2.23	-2.795	0.0079
0.83	0.47	0.0152	3.01	-3.611	0.0087
1.01	0.57	0.1489	9.06	-7.969	0.0133
1.19	0.67	0.3401	15.96	-11.791	0.0159

Table 23 Experimental results for Case V in chapter 3 for deep water

Deep water				
Model speed (m/s)	Trim (deg.)	Load (N)	Sinkage (mm)	C_T
0.83	0.0296	2.92447	-1.42217	0.005044
1.01	0.0513	4.143957	-2.21294	0.004827
1.19	-0.1127	5.067421	-4.96603	0.004692
1.31	-0.1348	6.149603	-5.92171	0.004692
1.37	-0.1493	6.773131	-6.70971	0.004796
1.43	-0.1629	7.50624	-7.15059	0.004843

Table 24 Experimental results for Case I in chapter 4 for H/T=2.2 and trim 0.9 degree.

Loading condition with trim 0.9 degree				
Model speed (m/s)	Depth Froude number (Fn)	Trim (deg.)	Sinkage (mm)	R_T(N)
0.18	0.10	0.0031	-0.18	0.17
0.36	0.20	0.0041	-0.98	0.66
0.42	0.23	0.0055	-1.30	0.97
0.53	0.30	0.0002	-2.20	1.57
0.71	0.40	0.0216	-4.38	3.04
0.89	0.50	0.0970	-7.04	6.06
1.01	0.57	0.2068	-8.03	9.39
1.07	0.60	0.3026	-8.55	12.30
1.13	0.64	0.4347	-7.79	15.10
1.19	0.67	0.5619	-7.28	18.47

Table 25 Experimental results for Case I in chapter 4 for H/T=2.2 and trim 0.3 degree.

Loading condition with trim 0.3 degree				
Model speed (m/s)	Depth Froude number (Fn)	Trim (deg.)	Sinkage (mm)	R_T(N)
0.18	0.10	0.0044	-0.13	0.10
0.36	0.20	-0.0020	-1.04	0.66
0.42	0.23	0.0009	-1.29	0.88
0.53	0.30	-0.0014	-2.63	1.49
0.71	0.40	0.0022	-4.68	2.86
0.89	0.50	0.0688	-7.62	6.06
1.01	0.57	0.1631	-8.77	9.48
1.07	0.60	0.2727	-9.24	12.46
1.13	0.64	0.3893	-8.31	15.43
1.19	0.67	0.5035	-7.93	18.48

Table 26 Experimental results for Case I in chapter 4 for H/T=2.2 and trim -0.3 degree.

Loading condition with trim -0.3 degree				
Model speed (m/s)	Depth Froude number (Fn)	Trim (deg.)	Sinkage (mm)	R_T(N)
0.18	0.10	-0.0049	-0.21	0.14
0.36	0.20	-0.0080	-0.98	0.65
0.42	0.23	-0.0077	-1.47	0.92
0.53	0.30	-0.0151	-2.27	1.46
0.71	0.40	-0.0131	-5.15	2.90
0.89	0.50	0.0526	-8.50	6.26
1.01	0.57	0.1611	-9.57	10.12
1.07	0.60	0.2721	-10.32	13.02
1.13	0.64	0.4133	-9.28	16.58
1.19	0.67	0.5434	-8.46	19.60

Table 27 Experimental results for Case I in chapter 4 for H/T=2.2 and trim -0.9 degree.

Loading condition with trim -0.9 degree				
Model speed (m/s)	Depth Froude number (Fn)	Trim (deg.)	Sinkage (mm)	R_T(N)
0.18	0.10	-0.0056	-0.49	0.13
0.36	0.20	-0.0166	-1.01	0.64
0.42	0.23	-0.0133	-1.57	0.96
0.53	0.30	-0.0226	-2.86	1.48
0.71	0.40	-0.0244	-5.59	2.96
0.89	0.50	0.0690	-8.78	6.77
1.01	0.57	0.1710	-9.82	10.14
1.07	0.60	0.3164	-9.92	13.55
1.13	0.64	0.4776	-9.20	17.46
1.19	0.67	0.6241	-8.78	20.76

Table 28 Experimental results for Case I in chapter 4 for H/T=1.78 and trim 0.9 degree.

Loading condition with trim 0.9 degree				
Model speed (m/s)	Depth Froude number (Fn)	Trim (deg.)	Sinkage (mm)	R_T(N)
0.18	0.10	-0.0061	-0.48	0.16
0.24	0.13	0.0001	-1.51	0.33
0.30	0.17	-0.0013	-1.37	0.59
0.36	0.20	0.0002	-2.10	0.86
0.42	0.23	0.0005	-2.83	1.22
0.48	0.27	0.0023	-3.23	1.50
0.53	0.30	0.0075	-3.96	2.00
0.59	0.33	0.0074	-4.76	2.45
0.65	0.37	0.0119	-6.12	2.95
0.71	0.40	0.0144	-7.60	3.68
0.77	0.44	0.0478	-9.13	5.02
0.83	0.47	0.0808	-9.98	6.67
0.89	0.50	0.1255	-11.62	8.38
0.95	0.54	0.1832	-12.09	10.52
1.01	0.57	0.2854	-13.00	13.97
1.07	0.60	0.4595	-13.90	19.23
1.13	0.64	0.6713	-13.25	24.99
1.19	0.67	0.8583	-11.80	29.73

Table 29 Experimental results for Case I in chapter 4 for H/T=1.78 and trim -0.9 degree.

Loading condition with trim -0.9 degree				
Model speed (m/s)	Depth Froude number (Fn)	Trim (deg.)	Sinkage (mm)	R_T(N)
0.18	0.10	-0.0101	-0.36	0.19
0.24	0.13	-0.0154	-1.15	0.35
0.30	0.17	-0.0175	-1.50	0.58
0.36	0.20	-0.0212	-1.87	0.82
0.42	0.23	-0.0246	-2.51	1.15
0.48	0.27	-0.0354	-3.30	1.45
0.53	0.30	-0.0422	-3.93	1.94
0.59	0.33	-0.0515	-4.54	2.43
0.65	0.37	-0.0654	-5.98	2.91
0.71	0.40	-0.0703	-7.13	3.77
0.77	0.44	-0.0571	-8.80	4.89
0.83	0.47	-0.0306	-9.94	6.73
0.89	0.50	-0.0037	-11.09	8.38
0.95	0.54	0.0574	-13.00	11.30
1.01	0.57	0.1289	-13.15	14.35
1.07	0.60	0.2756	-13.99	19.19
1.13	0.64	0.4712	-13.32	24.68
1.19	0.67	0.6276	-13.09	29.20

Table 30 Experimental results for Case I in chapter 4 for H/T=2.2

H/T=2.2					
Model speed (m/s)	Depth Froude number (Fn)	Trim (deg.)	Load (N)	Sinkage (mm)	C_T
0.18	0.10	0.0008	0.20	-0.70	0.0048
0.24	0.13	-0.0102	0.24	-0.41	0.0050
0.30	0.17	-0.0007	0.40	-0.58	0.0054
0.36	0.20	-0.0068	0.52	-0.49	0.0049
0.42	0.23	-0.0128	0.77	-0.76	0.0053
0.48	0.27	-0.0157	1.05	-1.39	0.0055
0.53	0.30	-0.0224	1.30	-2.09	0.0054
0.59	0.33	-0.0266	1.56	-2.39	0.0053
0.83	0.47	-0.0572	3.15	-5.96	0.0054
1.01	0.57	-0.1028	4.51	-10.07	0.0052
1.19	0.67	-0.1853	6.75	-17.77	0.0057
1.31	0.74	-0.1717	11.50	-28.41	0.0080
1.37	0.77	0.6542	27.82	-38.21	0.0178

Table 31 Experimental results for Case II in chapter 4

H/T=2.2				
Model speed (m/s)	Depth Froude number (Fn)	Trim (deg.)	Sinkage (mm)	R_T(N)
0.18	0.10	-0.0032	-0.38	0.17
0.24	0.13	-0.0017	-0.58	0.30
0.30	0.17	-0.0038	-0.79	0.50
0.36	0.20	-0.0011	-1.23	0.78
0.42	0.23	-0.0031	-2.13	1.06
0.48	0.27	-0.0020	-2.12	1.45
0.53	0.30	-0.0002	-2.88	1.88
0.59	0.33	0.0046	-3.71	2.30
0.65	0.37	0.0148	-5.03	3.13
0.71	0.40	0.0428	-6.21	4.28
0.77	0.44	0.0955	-6.82	5.99
0.83	0.47	0.1812	-7.09	8.14
0.89	0.50	0.2634	-7.63	10.43
0.95	0.54	0.3717	-7.20	13.28
1.01	0.57	0.5203	-6.86	17.11
1.07	0.60	0.6890	-4.92	21.13
1.13	0.64	0.8511	-2.21	25.01
1.19	0.67	0.9779	0.85	27.62
1.31	0.74	1.2502	6.42	33.58
1.49	0.84	1.2578	11.99	34.78

Table 32 Experimental results for Case III in chapter 4

H/T=2.2				
Model speed (m/s)	Depth Froude number (Fn)	Trim (deg.)	Sinkage (mm)	R_T(N)
0.18	0.10	-0.0041	-0.37	0.10
0.36	0.20	-0.0083	-0.74	0.59
0.42	0.23	-0.0078	-1.21	0.78
0.48	0.27	-0.0135	-1.54	1.03
0.53	0.30	-0.0172	-1.84	1.27
0.65	0.37	-0.0324	-3.47	1.85
0.71	0.40	-0.0422	-4.17	2.28
0.77	0.44	-0.0466	-5.16	2.65
0.83	0.47	-0.0656	-5.36	3.02
0.89	0.50	-0.0873	-6.25	3.42
0.95	0.54	-0.1001	-9.06	4.17
1.01	0.57	-0.1257	-9.96	4.47
1.10	0.62	-0.1744	-13.32	5.47
1.19	0.67	-0.2249	-17.17	6.62
1.31	0.74	-0.2800	-30.20	10.41

1.37	0.77	0.6300	-40.39	28.60
1.43	0.80	1.6035	-38.37	46.79

Table 33 Text matrix for all running test

	Case number	Number of H/T	Number of speeds	Number of loading condation trim	Number of run
Chapter 3	I	4	13 for each H/T	1	52
	II	3	11 for each H/T	1	33
	III	3	11 for each H/T	1	33
	IV	1	6	1	6
Chapter 4	I	1	10 for each trim angle	5	50
	I	1	18	2	36
	II	1	20	1	20
	I	1	17	1	17
				Total number of run	**247**

Table 34 Test matrix for all CFD running test

	Case type	Number of H/T	Number of speeds	Number of loading condation trim	Number of run
Multiphase	Rectangular Canal	1	6	1	6
	Suez Canal	1	4	1	4
Double body	Rectangular Canal	1	6	1	6
	Suez Canal	1	4	1	4
				Total number of run	**20**